TWO-PHASE FLOW INTERFACIAL STRUCTURE STUDY FOR BUBBLY TO SLUG AND CHURN-TURBULENT TO ANNULAR TRANSITIONS

by

Guanyi Wang

A Dissertation

Submitted to the Faculty of Purdue University

In Partial Fulfillment of the Requirements for the degree of

Doctor of Philosophy

School of Nuclear Engineering

West Lafayette, Indiana

August 2020

THE PURDUE UNIVERSITY GRADUATE SCHOOL
STATEMENT OF COMMITTEE APPROVAL

Dr. Mamoru Ishii, Chair
School of Nuclear Engineering

Dr. Seungjin Kim
School of Nuclear Engineering

Dr. Martin Lopez-De-Bertodano
School of Nuclear Engineering

Dr. Steven T. Wereley
School of Mechanical Engineering

Approved by:
Dr. Seungjin Kim

致我的父母和妻子

To my parents and wife

ACKNOWLEDGMENTS

I would like to express my sincerest gratitude to my advisor, Distinguished Professor Mamoru Ishii, for his mentoring, support, and encouragement during the past 6 years. Prof. Ishii's insight, vision, and rigorous attitude on research always inspire me. I would also like to express my genuine appreciation to Professors Seungjin Kim, Martin Lopez-De-Bertodano, and Steven T. Wereley for serving on my doctoral committee and for their valuable comments.

Special thanks to all members of the Thermal-hydraulic and Reactor Safety Laboratory that I had the great pleasure to work with during my study, especially to Dr. Qingzi Zhu, Mr. Yang Zhao, Mr. Zhuoran Dang, and Mr. Ke Tang for their help and collaboration. I am also grateful to the machinist James Younts for his great technical assistance.

The research reported in this dissertation was supported by several projects from the Naval Nuclear Laboratory (Bettis Atomic Power Laboratory) and the United States Nuclear Regulatory Commission. I would like to express my sincere appreciation to Dr. J.R. Buchanan and Dr. Steve Bajorek for their insightful comments and suggestions.

Finally, I appreciate my family from my deepest heart. Thanks to my parents for their endless support and encouragement. Thanks to my wife Zhen for her love, patience, and support.

TABLE OF CONTENTS

LIST OF TABLES

LIST OF FIGURES

NOMENCLATURE

Latin Characters

A	Crossectional area [m^2]
A_i	Average surface area of fluid particles of volume V, [m^2]
a_i	Interfacial Area concentration[1/m]
C_0	Distrubution parameter [-]
CL	Chord length [m]
D	Diameter [m]
D_c	Volumetric equivalent diameter of the maximum spherical bubble [m]
D_h	Hydraulic diameter [m]
D_{m1}	Maximum group I bubble diameter [m]
D_{sm}	Sauter mean diameter [m]
D_1^*	Non-dimensional diameter ratio D_c / D_{sm1} [-]
f	Frequency [Hz] or particle number density distribution function [$1/m^6$]
G	Gap size of flow duct [m]
g	Gravitational acceleration [m/s^2]
H	Enthalpy [kJ/kg]
h	Disturbance wave height [m]
j	Superficial velocity [m/s]
p	Pressure [Pa]
q	Heat flux [W/m^2]
M_{ik}	Generalized interfacial drag [Pa]
n_1	Group 1 bubble number density [$1/m^3$]
L	Length [m]
P	probability [-]
p	Pressure [Pa]
Sr	Strouhal number [-]
R	Number source/sink rate per unit mixture volume [$1/m^3/s$], or radius [m]
Re	Reynolds number [-]
T	Transition function [-] or time [s]

u_r Relative velocity [m/s]

V Bubble Volume [m^3]

v Velocity [m/s]

We Weber number [-]

X Lockhart-Martinelli parameter

z Axial location [m]

Greek Characters

α Void fraction [-]

Γ Mass generation term [$kg/m^3/s$]

δ Film thickness [m]

η Void fraction source/sink rate [1/s]

μ Dynamic viscosity [Pa s]

ρ Density [kg/m^3]

σ Surface tension [N/m]

v Kinematic Viscosity [m^2/s]

τ Shear stress [Pa]

Φ Energy dissipation rate [W/m^3]

φ Interfacial area change rate [1/m/s]

χ Inter-group transfer coefficient [-]

Sub/Superscripts

drop Liquid droplet

f Liquid phase

g Gas phase

i Interfacial

k k^{th} group/phase

lig Liquid ligament

ph Phase change

Operators

$\langle \ \rangle$ Area-averaged quantity

$\langle\langle \ \rangle\rangle$ Void-weighted area-averaged quantity

ABSTRACT

To fully realize the advantages of the two-fluid model, the interfacial area concentration (IAC) should be properly given by a constitutive model. The conventional flow-regime-based IAC correlations intrinsically cannot predict the dynamic flow structure change and would introduce a discontinuity and numerical instability to system codes. As a promising alternative, the interfacial area transport equation (IATE) is developed to model the interface structure mechanistically. Progress has been achieved for IATE modeling in bubbly, slug, and churn-turbulent flow during the past two decades. Aiming at a comprehensive flow structure predictor for all flow regimes, further development in two directions is highly desirable. First is extending the current experiment and modeling capability from churn-turbulent to annular flow. In this study, an advanced four-sensor droplet capable conductivity probe (DCCP-4) is developed to capture all interfaces in churn-turbulent and annular flow, including liquid film, liquid droplet, gas core, and gas bubble. A first of a kind experimental database in churn-turbulent, annular, and wispy annular flow with two-dimensional spatial distributions is established, which provides the experimental basis for the multi-field two-phase flow model development. The measured parameters include local time-averaged volume faction, IAC, and velocity for various fields of annular flow. In addition, a new constitutive model to quantify the interfacial area between the gas core and liquid film of annular flow is developed, which fills the last theoretical gap of interfacial area modeling. The other important direction is improving the current IATE model to fulfill the dynamic prediction of developing flow, especially the bubbly to slug transition flow. Vertical-upward air-water two-phase flow experiments are performed. The state-of-the-art IATE model is evaluated against the newly collected data at bubbly and slug flow, and the result shows unsatisfactory performance in predicting the developing flow with intensive bubble coalescence. A new bubble coalescence model is derived by using the log-normal bubble size distribution, which significantly improves the model prediction capability.

1. INTRODUCTION

1.1 Importance of the Problem and Research Background

Given the ubiquity and importance of gas-liquid two-phase flow in various industrial applications like nuclear, chemical, petroleum industries, it is critical to have solid knowledge and reliable models to accurately predict two-phase flow phenomena. The complexity of two-phase flow is rooted in the diverse and deforming interfacial structures, such as spherical, distorted, cap, slug, and churn bubbles, as well as liquid film and droplets. Several kinds of analytical models have been proposed to describe two-phase flow, like the homogeneous [1], drift-flux [2], and two-fluid [3] models. These models are developed based on temporal or spatial averaging and some detailed local information is eliminated, which is usually unnecessary for practical applications. In comparison to these averaged models, direct numerical simulation (DNS) [4] has developed rapidly, which is characterized by solving the local instant formulations using numerical methods. This method requires very fine mesh to resolve the interface between phases. Considering the significant size disparity between a nuclear reactor and the representative length scale of a bubble in a pressurized or boiling water reactor, the computational cost for DNS is too expensive for practical application in the foreseeable future. Therefore, averaged models will continue to play a critical role in two-phase flow system analysis and design. Among those practical models, the two-fluid model has been widely accepted as the most advanced and accurate model, because it treats two phases separately and has field equations for each phase. The two-fluid model was first rigorously derived by Ishii [5] in 1975. He used time-averaging and obtained the two-fluid model formulation from the local instant formulation. Apart from time-averaging, other averaging methods like area and volume averaging [6] and ensemble averaging [7] were also adopted to get the two-fluid model formulation.

In the two-fluid model, the mass, momentum, and energy transport are considered separately for each phase, resulting in six field equations. Apart from these six field equations, interfacial jump conditions and interfacial transfer terms need to be specified to account for the interaction at the interface. The accuracy of the interfacial transfer terms is of great importance to the performance of the two-fluid model, as these terms characterize the mass, momentum, and energy transfer

between phases. The magnitude of the interfacial transfer is directly related to the interfacial geometry structure, i.e., area of the interface. The interfacial geometry structure of the flow can be represented by interfacial area concentration (IAC), which is defined as the amount of interface area per unit volume. IAC quantifies the surface area available for the inter-phase transfer. To fulfill the advantages of the two-fluid model, accurate prediction of interfacial area concentration is indispensable.

There are two approaches to model the IAC, as shown in Table 1-1. The first one is using specific correlations for different flow regimes. Given that the flow structure within each flow regime would not significantly change, it is feasible to develop a correlation that could be applied to a specific flow regime. The advantage of this method is it is simple and easy to apply. However, there are several shortcomings to this approach. First, flow regime transition criteria are developed based on experimental results of steady-state, fully developed flow, and usually by flow visualization or analyzing area-averaged measurement results [8]–[11]. As a result, the capability of the model using flow regime transition criteria could be questionable in predicting developing and dynamic flow and flow with a significant spatial distribution. Second, the constitutive correlations developed for each flow regime may not be continuous at the transition boundary, and employing these correlations could introduce numerical instability to the code [12], [13]. Lastly, the flow structure is very sensitive to the injection method. If the initial bubble size is different, the flow patterns could be different for the same inlet gas and liquid fluxes. Therefore, the applicability of a flow regime map depends on the specific situation, and error may be introduced if using the flow regime map in generalized modeling. In view of these deficiencies, the interfacial area transport equation (IATE) [14] was proposed based on the fluid particle number density transport equation and bubble interaction mechanisms, with the target to dynamically characterize the local structure and properly handle the flow regime transitions. To develop a transport equation that can mechanistically represent the developing interfacial structure change for various flow regimes, considerable efforts in constitutive modeling for different responsible mechanisms are required, like bubble coalescence/disintegrate, nucleation/evaporating/condensing, pressure effect, etc. The United States Nuclear Regulatory Commission (U.S. NRC) has been cooperating with Purdue University to develop the interfacial area transport equation for one-dimensional (1-D) system analysis codes since 1997 [15]. As a result, one-group and two-group IATE models have

been developed and a comprehensive database has been established for benchmarking. Also, IATE has been used with 1-D and three-dimensional (3-D) two-fluid model, to predict both 1-D [16] and 3-D two-phase flow cases [17]. Significant progress has been achieved for IATE modeling of bubbly, slug, and churn-turbulent flow with detailed local 3-D two-phase flow data during the past two decades [18]–[23]. Further improvement is still required in several directions, including churn-turbulent to annular transition, developing flow with the significant intergroup transfer, IAC change due to boiling and condensing, etc. In this study, aiming at a comprehensive flow structure predictor for all flow regimes, two major targets are selected: first is extending the current experiment and modeling capability from churn-turbulent to annular flow; second is improving the current IATE model to fulfill the dynamic prediction of developing flow. In the following sections, the previous related studies are reviewed, and the significance of these two targets are discussed in detail.

Table 1-1 Comparison of approaches for specifying interfacial area concentration

Approach to quantify IAC	Advantages	Challenges
IAC correlations based on flow regimes	1. Easy to develop 2. Simple to use	1. Discontinuity at the flow regime boundaries 2. Cannot predict the flow dynamics
Interfacial area transport equation (IATE)	1. Dynamic prediction 2. Flow-regime independent	1. Require effort on constitutive modeling 2. Currently not applicable to annular flow

1.2 Literature Survey

In this section, the previous related studies are reviewed. First, the two-fluid model and interfacial area transport equation are briefly introduced. Then, the previous efforts in the IATE constitutive model development are reviewed with a focus on the bubbly to slug transition flow, namely one-group to two-group transition. Lastly, the previous modeling efforts in annular flow are reviewed to prepare the development of a comprehensive IAC predictor working from bubbly to annular flow.

1.2.1 Two-fluid Model and Interfacial Area Transport Equation

The two-fluid model is derived from the local instant conservation formulations of each phase by using suitable averaging methods to eliminate high-frequency information from local instant fluctuations of variables. After averaging, the two-fluid model cannot resolve the local instant interface information, which is usually far more detailed than the practical need, but the computational cost decreases significantly and makes it possible to solve an engineering problem using the two-fluid model. Comparing to the mixture model, two phases are treated separately when solving mass, momentum, and energy transfer. This provides advantages when solving problems where the two phases are weakly coupled. The simplified three-dimensional two-fluid model can be expressed as [3]:

Continuity equation:

$$\frac{\partial \alpha_k \rho_k}{\partial t} + \nabla \cdot \left(\alpha_k \rho_k \overrightarrow{v_k} \right) = \Gamma_k \tag{1.1}$$

Momentum equation:

$$\begin{aligned} \frac{\partial \alpha_k \rho_k \overrightarrow{v_k}}{\partial t} + \nabla \cdot \left(\alpha_k \rho_k \overrightarrow{v_k} \overrightarrow{v_k} \right) = -\alpha_k \nabla p_k + \nabla \cdot \alpha_k \left(\overline{\overline{\tau}}_k^{\mu} + \overline{\overline{\tau}}_k^{T} \right) \\ + \alpha_k \rho_k \vec{g} + \overrightarrow{v_{ki}} \Gamma_k + \overrightarrow{M_{ik}} - \nabla \alpha_k \cdot \overline{\overline{\tau}}_i \end{aligned} \tag{1.2}$$

Enthalpy energy equation:

$$\frac{\partial \alpha_k \rho_k H_k}{\partial t} + \nabla \cdot \left(\alpha_k \rho_k H_k \overrightarrow{v_k} \right) = -\nabla \cdot \alpha_k \left(\overrightarrow{q_k}^{\mu} + \overrightarrow{q_k}^{T} \right) + \alpha_k \frac{D_k}{Dt} p_k + H_{ki} \Gamma_k + \frac{q''_{ki}}{L_s} + \Phi_k \tag{1.3}$$

where Γ_k, $\overrightarrow{M_{ik}}$, τ_i, q''_{ki}, and Φ_k are the mass generation, generalized interfacial drag, interfacial shear stress, interfacial heat flux, and dissipation, respectively. The subscript *k* represents the parameter for phase *k*, and *i* means the interface. Among these parameters the interfacial mass transfer terms, interfacial drag forces, and interfacial heat flux describe the mass, momentum and energy transfer at the interface, and they all can be expressed as the product of interfacial area concentration and the driving force:

$$(\text{Interfcial transfer term}) \approx a_i \times (\textit{Driving}\ \text{force/flux}) \tag{1.4}$$

To fulfill the benefits of the two-fluid model, mass, momentum, and energy transfer between phases should be correctly specified by constitutive models. The key is accurately specifying interface structure and interfacial area because this is where the transfer processes happen.

In the current best-estimate thermal-hydraulic system analysis codes, the IAC is estimated using empirical correlations. However, these correlations depend on the flow regime transition criteria to describe the flow structure, and these criteria were usually based on the steady-state, fully developed two-phase flow experimental results. As mentioned previously, using this kind of correlation to predict the dynamic behavior of the interfacial structure could result in abnormal system behavior and limit the code accuracy. To predict the dynamic development of the interfacial structure, IATE was proposed by Kocamustafaogullari and Ishii [14] to replace the flow-regime-based correlations. IATE is derived as an analogy to the Boltzmann transport equation and is based on the fluid particle number density balance. For bubbly flow, the bubble size variance is limited and the interaction characteristics for different bubbles are similar. Therefore, one-group IATE [24] is sufficient to describe the bubble interaction and interfacial area transport:

$$\frac{\partial a_i}{\partial t}+\nabla\cdot\left(a_i v_{gi}\right)=\frac{2}{3}\frac{a_i}{\alpha}\left[\frac{\partial \alpha}{\partial t}+\nabla\cdot\left(\alpha\, v_g\right)-\eta_{ph}\right]+\sum_j \phi_j+\phi_{ph} \tag{1.5}$$

where α, a_i, v_{gi}, and v_g represents void fraction, interfacial area concentration, interface velocity, gas phase velocity, respectively. ϕ_j is the source/sink for the interfacial area concentration due to j^{th}-type bubble interaction mechanisms. ϕ_{ph} is the source/sink for the interfacial area concentration due to phase change. η_{ph} is the source/sink for the void fraction due to phase change (nucleation/collapse). The one-group IATE modeling of the bubble coalescence and breakup mechanisms in bubbly flow was performed by Wu et al. [24]. However, one-group IATE assumes that the size and shape of all bubbles are close, and the coalescence and breakup mechanisms can be applied to all bubbles. Therefore, the one-group IATE model does not apply to bubbly-slug transition, slug, and churn-turbulent flow conditions, where cap and slug bubbles exist. Two-group IATE was proposed to address this issue, which is firstly derived by Ishii and Kim [25]. It consists of two transport equations to describe the interfacial area transport of sphere/distorted bubbles and cap/slug bubbles, respectively. The two-group interfacial area transport equation is given as [26]:

$$\begin{aligned}\frac{\partial a_{i1}}{\partial t}+\nabla\cdot\left(a_{i1}v_{gi1}\right)=&\frac{2}{3}\frac{a_{i1}}{\alpha_1}\left[\frac{\partial \alpha_1}{\partial t}+\nabla\cdot\left(\alpha_1 v_{g1}\right)-\eta_{ph1}\right]\\&-\chi D_{c1}^{*\,2}\frac{a_{i1}}{\alpha_1}\left[\frac{\partial \alpha_1}{\partial t}+\nabla\cdot\left(\alpha_1 v_{g1}\right)-\eta_{ph1}\right]+\sum_j \phi_{j,1}+\phi_{ph1}\end{aligned} \tag{1.6}$$

and

$$\frac{\partial a_{i2}}{\partial t}+\nabla\cdot\left(a_{i2}\boldsymbol{v}_{gi2}\right)=\frac{2}{3}\frac{a_{i2}}{\alpha_2}\left[\frac{\partial\alpha_2}{\partial t}+\nabla\cdot\left(\alpha_2\boldsymbol{v}_{g2}\right)-\eta_{ph2}\right]$$
$$+\chi D_{c1}^{*2}\frac{a_{i1}}{\alpha_1}\left[\frac{\partial\alpha_1}{\partial t}+\nabla\cdot\left(\alpha_1\boldsymbol{v}_{g1}\right)-\eta_{ph1}\right]+\sum_j\phi_{j,2}+\phi_{ph2} \tag{1.7}$$

Here the subscript '1' represents the spherical and distorted bubble group, the subscript '2' represents the cap and slug bubble group. The boundary between group I and group II is the maximum distorted bubble size, which is given as [27]:

$$D_c=4\sqrt{\frac{\sigma}{g\Delta\rho}} \tag{1.8}$$

Like the one-group IATE, the left-hand sides of Eq. (1.6) and (1.7) are the time derivative and the advection of the IAC for each group, respectively. The first right-hand side terms are the intragroup expansion/contraction source/sink terms. These terms account for the IAC change due to the expansion/contraction of existing particles (bubbles) within each group. The second RHS terms are the intergroup expansion/contraction source/sink terms, which represents the IAC change due to the expansion/contraction of particles across the group boundary. k=1 and 2 for group I and II, respectively. α_k, a_{ik}, v_{gik}, and v_{gk} is the void fraction, interfacial area concentration, interfacial velocity, and gas phase velocity for group k, respectively. η_{phk} is the source/sink for the void fraction due to phase change (nucleation/collapse), and $\phi_{j,k}$ is the source/sink for the interfacial area concentration due to j^{th}-type bubble interactions mechanisms for group k bubbles. χ is the inter-group transfer coefficient at the group boundary. D_{c1}^{*} is the non-dimensional bubble diameter defined by

$$D_{c1}^{*}=\frac{D_c}{D_{\mathrm{sm1}}} \tag{1.9}$$

where D_c is defined by Eq. (1.8). D_{sm1} is the Sauter mean diameter of group I bubbles. Recently Worosz [28] pointed out that the effect of the intergroup transfer is double-counted in the current IATE formulation. Usually, the intergroup transfer is counted by the IAC bubble interaction terms $\phi_{j,k}$, but the void fraction change $\nabla\cdot\left(\alpha_k\boldsymbol{v}_{gk}\right)$ in the expansion/contraction source terms also includes the effect of the intergroup transfer. The reason is that $\nabla\cdot\left(\alpha_k\boldsymbol{v}_{gk}\right)$ is calculated through void transport equations, which also includes intergroup transfer source/sink terms for the void fraction η_j^{inter}. A revised two-group IATE is proposed by Worosz [28] to remove the intergroup transfer effects from the expansion/contraction source terms in Eq. (1.6) and (1.7):

$$\frac{\partial a_{i1}}{\partial t}+\nabla\cdot\left(a_{i1}\boldsymbol{v}_{gi1}\right)=\frac{2}{3}\frac{a_{i1}}{\alpha_1}\frac{1}{1-\chi D_{c1}^{*3}}\left[\frac{\partial\alpha_1}{\partial t}+\nabla\cdot\left(\alpha_1\boldsymbol{v}_{g1}\right)-\eta_{\mathrm{ph1}}-\sum_j\eta_{j,1}^{\mathrm{inter}}\right]$$
$$-\chi D_{c1}^{*2}\frac{a_{i1}}{\alpha_1}\frac{1}{1-\chi D_{c1}^{*3}}\left[\frac{\partial\alpha_1}{\partial t}+\nabla\cdot\left(\alpha_1\boldsymbol{v}_{g1}\right)-\eta_{\mathrm{ph1}}-\sum_j\eta_{j,1}^{\mathrm{inter}}\right]+\sum_j\phi_{j,1}+\phi_{\mathrm{ph1}} \tag{1.10}$$

$$\frac{\partial a_{i2}}{\partial t}+\nabla\cdot\left(a_{i2}\boldsymbol{v}_{gi2}\right)=\frac{2}{3}\frac{a_{i2}}{\alpha_2}\left\{\frac{\partial\alpha_2}{\partial t}+\nabla\cdot\left(\alpha_2\boldsymbol{v}_{g2}\right)-\eta_{\mathrm{ph2}}\right.$$
$$\left.-\frac{1}{1-\chi D_{c1}^{*3}}\left[\sum_j\eta_{j,1}^{\mathrm{inter}}+\chi D_{c1}^{*3}\left(\frac{\partial\alpha_1}{\partial t}+\nabla\cdot\left(\alpha_1\boldsymbol{v}_{g1}\right)-\eta_{\mathrm{ph1}}\right)\right]\right\}$$
$$+\chi D_{c1}^{*2}\frac{a_{i1}}{\alpha_1}\frac{1}{1-\chi D_{c1}^{*3}}\left[\frac{\partial\alpha_1}{\partial t}+\nabla\cdot\left(\alpha_1\boldsymbol{v}_{g1}\right)-\eta_{\mathrm{ph1}}-\sum_j\eta_{j,1}^{\mathrm{inter}}\right] \tag{1.11}$$
$$+\sum_j\phi_{j,2}+\phi_{\mathrm{ph2}}$$

In addition to the basic IATE formulation, the modeling of various IAC transfer mechanisms is critical, i.e. specifying the value of ϕ_j, ϕ_{ph}, and η_{ph}. Since this study focuses on the hydrodynamic investigation of two-phase flow, the phase change terms will not be reviewed here. Bubble coalescence and break-up mechanisms in IATE are modeled as constitutive equations. For bubble coalescence, the random collision (RC) driven by turbulent eddies and the wake entrainment (WE) effect of a bubble following a preceding bubble are considered as major mechanisms. For bubble disintegration, the turbulent impact (TI), shearing-off (SO) of large bubbles, and the surface instability (SI) are recognized as major mechanisms. Table 2-1 summarizes the major bubble interaction mechanisms for two-group IATE. For example, $\phi_{RC,1}^{(11,2)}$ represents the sink terms of group I IAC due to the random collision of two group I bubbles, which generates a group II bubble. It should be mentioned that there are several kinds of these IAC source/sink constitutive models [18], [23], [29], [30], which are developed to characterize the different kinds of flow channel such as moderate size round pipe, large size round pipe, rectangular flow channel, etc. Fu and Ishii [18], [31] developed a comprehensive set of IAC source/sink models for moderate size round pipes and benchmarked against 48.3 mm ID round pipe data. Given that this model is developed for moderate size pipe, the source/sink terms resulting from the random collision of group II bubbles, turbulence impact on group II bubbles and the surface instability are not considered.

Table 1-2 Major two-group bubble interaction mechanism [18]

Mechanism	Interaction	a_i Source/sink term	a_i Source/sink
Random-Collision (RC)	(1)+(1)→(1)	$\phi_{RC}^{(1)}$	G1 sink
	(1)+(1)→(2)	$\phi_{RC,1}^{(11,2)}, \phi_{RC,2}^{(11,2)}$	G1 sink, G2 source
	(1)+(2)→(2)	$\phi_{RC,1}^{(12,2)}, \phi_{RC,2}^{(12,2)}$	G1 sink, G2 source
	(2)+(2)→(2)	$\phi_{RC}^{(2)}$	G2 sink
Wake-Entrainment (WE)	(1)+(1)→(1)	$\phi_{WE}^{(1)}$	G1 sink
	(1)+(1)→(2)	$\phi_{WE,1}^{(11,2)}, \phi_{WE,2}^{(11,2)}$	G1 sink, G2 source
	(1)+(2)→(2)	$\phi_{WE,1}^{(12,2)}, \phi_{WE,2}^{(12,2)}$	G1 sink, G2 source
	(2)+(2)→(2)	$\phi_{WE}^{(2)}$	G2 sink
Turbulence-Impact (TI)	(1) →(1)+(1)	$\phi_{TI}^{(1)}$	G1 source
	(2) →(2)+(2)	$\phi_{TI}^{(2)}$	G2 source
Surface-Instability (SI)	(2) →(2)+(2)	$\phi_{SI}^{(2)}$	G2 source
Shearing-Off (SO)	(2) →(2)+(1)	$\phi_{SO,1}^{(2,12)}, \phi_{SO,2}^{(2,12)}$	G1 source, G2 sink

1.2.2 IATE Modeling at Bubbly to Slug Transition

Since one major target for IATE is to have the continuous prediction capability for various flow regimes, IATE models must accurately represent the flow structure change at bubbly to slug transition. In bubbly to slug transition flow, group I bubbles coalescence and form group II bubbles. Therefore, the IATE intergroup transfer terms $\phi_{RC}^{(11,2)}, \phi_{WE}^{(11,2)}$ are important, and the models of these terms are introduced in this section.

In the IATE model developed by Fu and Ishii [18], the intergroup transfer terms $\phi_{RC}^{(11,2)}, \phi_{WE}^{(11,2)}$ are formulated in a similar way to the one group condition. For turbulence-induced random collisions, the coalescence rate is given by Wu et al. [24]:

$$R_{RC}^{(1)} = C_{RC}\left[\frac{u_t n_1^2 D_{sm1}^2}{\alpha_{1,max}^{1/3}\left(\alpha_{1,max}^{1/3}-\alpha_1^{1/3}\right)}\right]\left[1-\exp\left(-C\frac{\alpha_{1,max}^{1/3}\alpha_1^{1/3}}{\alpha_{1,max}^{1/3}\left(\alpha_{1,max}^{1/3}-\alpha_1^{1/3}\right)}\right)\right] \tag{1.12}$$

To generate a group II bubble, two group I bubbles should if large enough. The probability for generating a group II bubble can be expressed as:

$$\xi = P\left(V_{b1}+V_{b1}>V_c\right)=\frac{\int_{V_{1,\max}}^{V_{1,\max}}\int_{V_c-V_{1,\max}}^{V_c-V_{b1}} f\left(V_{b1}\right) f\left(V_{b2}\right) dV_{b2}dV_{b1}}{\int_{V_{1,\min}}^{V_{1,\max}}\int_{V_{1,\min}}^{V_{1,\max}} f\left(V_{b1}\right) f\left(V_{b2}\right) dV_{b2}dV_{b1}} \tag{1.13}$$

Assuming the bubbles follow uniform number density distribution, then

$$\xi = 2\left(1-0.2894D_{c1}^{*3}\right)^2 \tag{1.14}$$

D_{c1}^{*} is defined in Eq (1.9). Note that this probability is meaningful only if D_{sm1}>7.21 mm. Below this limit, group I bubbles coalescence can only generate larger group I bubbles, and the term $\phi_{RC}^{(11,2)}$ should be zero. Following this approach, when two group I bubbles coalescence become a group II bubble, the average change of interfacial area for group I can be expressed as:

$$\left\langle \delta A_{i1}^{(11,2)} \right\rangle_R = \frac{-\left(36\pi\right)^{1/3}\int_{V_c-V_{1,\max}}^{V_{1,\max}}\int_{V_c-V_{b1}}^{V_{1,\max}} \left[V_{b1}^{2/3}+V_{b2}^{2/3}\right] f\left(V_{b1}\right) f\left(V_{b2}\right) dV_{b2}dV_{b1}}{\int_{V_{1,\min}}^{V_{1,\max}}\int_{V_{1,\min}}^{V_{1,\max}} f\left(V_{b1}\right) f\left(V_{b2}\right) dV_{b2}dV_{b1}} \tag{1.15}$$

Considering the uniform bubble size distribution, it can be formulated as:

$$\left\langle \delta A_{i1}^{(11,2)} \right\rangle_R = D_{sm1}^2\left[8.82+2.035\left(0.579D_1^{*3}-1\right)^{8/3}-5.428D_1^{*3}\right] \tag{1.16}$$

Then the interfacial area sink term for group I due to intergroup coalescence driven by random collision is

$$\phi_{1,RC}^{(11,2)} = \left\langle \delta A_{i1}^{(11,2)} \right\rangle_R R_{RC}^{(1)} \tag{1.17}$$

Similarly, the interfacial area source term for group II is

$$\phi_{2,RC}^{(11,2)} = \left\langle \delta A_{i2}^{(11,2)} \right\rangle_R R_{RC}^{(1)} \tag{1.18}$$

and

$$\left\langle \delta A_{i2}^{(11,2)} \right\rangle_R = D_{sm1}^2\left[6.462-2.182D_1^{*5}-0.395D_1^{*8}\right] \tag{1.19}$$

The models of wake entrainment induced bubble coalescence is similar to the random collision, except the wake entrainment coalescence rate is different, which is given as [24]:

$$R_{WE}^{(1)} = C_{WE}^{(1)}C_D^{1/3}n_1^2D_{sm1}^2v_{r1} \tag{1.20}$$

v_{r1} is the relative velocity, n_1 is the group I bubble number density, C_D is the drag coefficient.

The corresponding sink and source terms are:

$$\phi_{1,WE}^{(11,2)} = \left\langle \delta A_{i1}^{(11,2)} \right\rangle_R R_{WE}^{(1)} \tag{1.21}$$

$$\phi_{2,WE}^{(11,2)} = \left\langle \delta A_{12}^{(11,2)} \right\rangle_R R_{WE}^{(1)} \tag{1.22}$$

Supporting models for these parameters are provided in Appendix A.

In addition, recently several updates have been made on the Fu-Ishii model to address some of its shortcomings [28], [32]. Doup [32] found that the units of Fu's models for $\phi_{WE,1}^{(12,2)}$, $\phi_{WE,2}^{(12,2)}$, $\phi_{WE}^{(2)}$, $\eta_{WE}^{(12,2)}$, and κ_{fr} are inconsistent, and proposed revisions on these terms and recalibrated the experimental constants based on his experimental data in 50 mm ID test section. Meanwhile, Worosz [28] collected data focusing on one-group to two-group transitions flow in 50.8 mm ID test section and evaluated Fu's models using TRACE-T code [33] and these data. It was found that Fu's model cannot predict the one-group to two-group transition flow accurately. To address this shortcoming, Worosz [28] developed a transition function to describe the group I to group II transition and implemented it into related source/sink terms. Those inconsistent terms were also revised, and new experimental coefficients were proposed. In summary, the prediction capability of bubbly to slug transition flow requires further improvement, which will be discussed in section 1.3

1.2.3 Annular Flow Two-Fluid Model

IATE is developed based on the bubble number density transport equation and benchmarked against various databases ranging from bubbly flow to churn-turbulent flow. However, with the long-term goal of a full range (bubbly to annular) interfacial structure predictor, it is highly desirable to extend the interfacial area modeling capability from churn-turbulent flow to annular flow. In this section, previous efforts in annular flow modeling under the two-fluid model framework are discussed.

In annular flow, the flow structure is quite different from the bubbly and slug flow. In bubby and slug flow, the liquid is a continuous phase and the gas phase is dispersed in terms of bubbles. In annular flow, either gas or liquid could exist in both continuous form (gas core/liquid film) and dispersed form (bubble/droplet). Given that the interfacial transfer mechanism and the velocity of the continuous field and the dispersed field of one phase could be significantly different, only using one set of field equations may not be able to describe the flow characteristics in annular flow. An approach termed the four-field two-fluid model was proposed by Lahey and Drew [34] to

accurately predict the distribution and dynamics of the continuous gas phase, continuous liquid phase, dispersed gas phase, and dispersed liquid phase. It is inherently capable to capture the essential features of gas/liquid flows for various flow regimes because each field has its conservation equation. The four-field two-fluid model has been applied on a wide range of data using computational fluid dynamics (CFD) including air-water bubbly flow data [35], [36], subcooled boiling data [37], [38], external two-phase flow [39]. The results obtained using four-field two-fluid model CFD agree with the experimental data. However, all experiments used to verify the model are bubbly and slug flows, few efforts have been made to apply the four-field model in the 3-D analysis of annular flow.

The prediction of the 3-D distribution of IAC in annular flow is a major challenge. Since the original IATE derived by Kocamustafaogullari and Ishii [14] is based on the bubble number density transport equation, the theoretical foundation of previous IATE modeling may no longer be solid in the churn to annular transition and annular flow. Besides, all IAC source/sink terms are modeled based on bubble interaction mechanisms and benchmarked against the experimental data at bubbly to churn turbulent flow, and the applicability of these constitutive models in annular flow is also not verified. Liu [40] derived a new form of IATE based by averaging the local instant interfacial area transport equation. Compared to the original IATE from the population balance equation, the new IATE has a similar form except for the formulation of source/sink terms. In the IATE for annular flow, the source/sink terms are given in terms of surface motion with mean curvature. However, his work just proposed a potential way to solve the IAC in annular flow and no specific constitutive modeling is given. Zhu [41] proposed a simpler way to describe the IAC in annular flow. In his work, a correlation is developed that can predict the wall peak IAC in annular flow based on physical characters of annular flow like film thickness and void fraction. But the accuracy and reliability of this correlation has not been verified by experimental data.

1.3 Required Improvements

1.3.1 IATE Model for Bubbly to Slug Transition

As mentioned in section 1.2.2, some recent experimental results [42], [43], [28] show that the performance of two-group IATE at bubbly to slug transition is not satisfying. The two-group IATE

tends to under-estimate the intergroup transfer at the transition, especially for flow conditions with a strong developing effect. The reason for this is that most experimental results used to benchmark the two-group are collected in fully developed for semi-fully developed conditions, and the constitutive model for two-group IATE may not be well benchmarked or well developed to account for the strong developing effect in the bubbly to slug transition flow. In addition, although some local measurement datasets have been collected using the multi-sensor conductivity probe [18], [42]–[44] [45], most of them either focused on bubbly flow only [44][45] or aimed at a wide flow range including bubbly, slug, and churn flow [42], [43] yet did not have enough data points at the transition for model development. Besides, lots of previous studies concentrated on the moderate size pipe with diameters about 50 mm [18], and some recent experimental results [46] showed that the bubbly to slug transition phenomena between a moderate and small pipe size were quite different. Given that the applicability of the two-group IATE model for a small diameter pipe has not been comprehensively checked with experimental data, as well as several discrepancies of the two-group IATE in predicting bubbly to slug transition flow has been reported [28], [32], performing an experiment in a small pipe in the bubble to slug transition flow is necessary to develop a more robust IATE model that can be applied to a wide range of flow patterns and flow channel sizes.

1.3.2 Experimental and Modeling Capability in Annular Flow

The IATE has been developed for bubbly, slug, and churn flow. However, aiming at a complete and comprehensive flow structure model, it is highly desirable to extend the interfacial area experimental and modeling capability from churn-turbulent flow to annular flow.

1.3.2.1 IAC instrumentation development in churn-turbulent to annular transition

Currently, few models were proposed to quantitively describe the flow structure at churn to annular transition flow, because it is very difficult to experimentally capture the flow structure at these regimes. Although there are several ways to measure the two-phase flow interfacial area concentration in low void fraction conditions – optical fiber probe [47]–[49], flow visualization using a high-speed camera [50], wire-mesh tomography [51]–[53], and conductivity probe [54] to name a few – most of them cannot be applied to high void fraction cases like slug and churn-

turbulent flow. The conductivity probe and wire-mesh sensors could be the only two applicable instruments for high void fraction local measurements, yet they still have some limitations. For wire-mesh sensors, there is a contradiction between its spatial resolution and its disturbance to the flow. To reach a high spatial resolution to detect the dispersed liquid (like droplets), the mesh size should very fine, which will significantly change the channel flow resistance and affect the flow structure. For the conductivity probe, it can distinguish the gas and liquid phase by measuring the conductance between the sensor tip and the probe casing. However, it cannot detect the dispersed liquid phase like droplets since the size of dispersed liquid particle is usually very small and cannot cover the sensor tip and the probe casing at the same time. As a result, a low conductance signal will be detected when the dispersed liquid passes through the probe sensor and it will be identified as the gas phase. Incorrectly identifying the dispersed liquid phase as the gas phase will not only introduce measurement errors to volume fraction and interfacial area, but also leads to the missing of dispersed liquid field information, which is extremely important to the modeling of churn-turbulent and annular flows. To extend the capability of the conductivity probe to the liquid dispersed two-phase flow, a new design named as double-sensor Droplet Capable Conductivity Probe (DCCP-2) was proposed by Liu et al [55]. In this design, one more sensor called a 'common sensor' was added to the conventional double-sensor conductivity probe. Using this extra sensor, the dispersed liquid can be detected by measuring the conductance between the common sensor and other sensors. However, the double-sensor probe including the DCCP-2 can only measure the interfacial area concentration of spherical particles like small bubbles and droplets. It is not capable to measure an irregular interface, which is often encountered in slug, churn-turbulent, and annular flows.

1.3.2.2 Annular flow IAC modeling

In annular flow, the liquid exists as the liquid film near the wall and the gas-liquid interface is almost parallel to the flow direction. In two-fluid model, the specific gas-liquid interface will not be resolved, and the amount of the interface will be represented by the IAC. However, if the interface is parallel to the flow direction, the IAC at the annular interface location will become infinity, which is a singularity and undesired in a CFD code. This interface singularity should be eliminated to extend the applicability of the 3-D two-fluid model to annular flow. The most physical way is to average the IAC to account for the liquid film wave fluctuation. If there are

fluctuations in the interface, the local IAC will change from a singularity to a distribution, which can be easily handled by a CFD code. Developing a constitutive model that can give the IAC distribution near the wall for annular flow will greatly aid in the CFD modeling of annular flow using the two-fluid model. Besides, a lot of previously developed entrainment/deposition models depend on the interface area and cannot be applied to two-fluid model CFD since the interface is not directly resolved. If an approach that can convert these entrainment/deposition models from interface dependent to the IAC dependent can be developed, then all previous models will be able to work with the IAC wall function and can be applied to a CFD code directly.

1.4 Research Objectives and Contribution

The goal of this study is to develop a comprehensive interfacial geometry structure predictor for the 3-D two-fluid model. To achieve the required improvements discussed in section 1.3, investigations with two objectives are performed: first is improving the mechanistic modeling of two-group IATE focusing on intergroup transfer; second is extending the current experimental and modeling capability from churn-turbulent to annular flow. They can be briefly divided into two parts in terms of flow conditions of interest: bubbly to slug transition and churn-turbulent to annular transition.

For the bubbly to slug transition study, the experimental objective is to develop a comprehensive database at bubbly to slug transition conditions. The data should include the information of void fraction, IAC, and interface velocity for both small bubbles (group I) and large bubbles (group II), and the accuracy of the data should be ensured by various cross-check methods. Once the experimental objective is finished, the current two-group IATE constitutive models will be evaluated using this database. If the performance of the IATE is not satisfying, the reason for the discrepancy will be analyzed in detail and modeling effort will be made on improving the two-group IATE for bubbly to slug transition flow.

For the study of churn-turbulent to annular transition, the objective also includes an experimental part and modeling part. To address the experimental research gap at the churn-turbulent to annular transition flow and support the modeling at these flow regimes, the four-sensor droplet capable conductivity probe (DCCP-4) will be developed in this study. By taking advantage of both

previous droplet capable conductivity and conventional four-sensor probes, the DCCP-4 can measure various kinds of interfaces existing in the churn-turbulent to annular transition flow including droplets and ligaments. For the modeling part, the target is developing a reliable constitutive model that can predict the IAC distribution near the wall for annular flow.

1.5 Thesis Outline

In Chapter 2, the bubbly to slug transition flow experiment is performed using the four-sensor conductivity probe at a higher sampling frequency than previous research to improve the measurement accuracy. The accuracy of the local measurement results is cross-checked against the averaged instrumentation and drift-flux model predictions. The 1-D development of the void fraction and the IAC is discussed. In the following Chapter 3, the measured IAC data is used to evaluate the current two-group IATE with constitutive models, and the further improvement on the modeling for bubbly to slug transition is also performed. Given that no suitable instrumentation can be used for the local measurement in churn-turbulent and annular flow, the four-sensor droplet capable conductivity probe (DCCP-4) is developed featuring liquid droplet measurement capability, which is given in Chapter 4. Chapter 5 presents the local measurements using DCCP-4 in the churn-turbulent to annular transition flow as well as the experimental study on the flow structure of wispy annular flow using the DCCP-4 and film thickness probe together. In Chapter 6, the experimental study of interfacial wave structure has been performed, and a comprehensive evaluation of various models for wave properties is performed using the new database. The modeling efforts including developing the near-wall IAC distribution model as well as converting previous interface-based entrainment and deposition models to IAC-based are given in Chapter 7.

2. BUBBLY TO SLUG TRANSITION FLOW EXPERIMENTS

2.1 Experiments in a 25.4 mm Round Pipe

2.1.1 Experimental Setup

The experimental facility is an adiabatic two-phase flow system, as schematically shown in Fig. 2-1. The test section is a 25.4 mm inner diameter acrylic pipe, with a total height of 3.81 m, corresponding to L/D_h = 150. There are 3 probe ports located at z/D_h = 15, 78, 141, respectively. The two-phase flow mixture injection systems are located at both the top and the bottom of the test section, which consists of a sparger and two water flow channels. The sparger is made up of porous material with an average pore size of 10 μm. The water supply line is divided into two lines before entering the two-phase mixture injector. One is called primary flow and the other is the secondary flow. The secondary flow shears the bubbles off the sparger and then mixes with the primary flow. Therefore, the initial bubble size is controlled by the secondary flow rate and usually set as 1-2 mm, and the inlet liquid flow rate can be adjusted by changing the primary flow. Air was supplied by a compressor and a tank, and a pressure regulator is used to maintain a constant pressure. Three rotameters with different measuring ranges (0.01-0.57 m^3/h, 0.14-1.42 m^3/h 2.83-28.32 m^3/h, respectively) are used to measure the gas flow rate with an accuracy of ±2% of full scale. Water is supplied via a centrifugal pump and controlled by valves and a frequency converter. The water flow rate is measured using electro-magnetic liquid flow meters with an accuracy of ±1%.

The four-sensor conductivity probe is employed to measure the local two-phase flow parameters including void fraction, interfacial area concentration and bubble velocity at three axial locations of z/D_h = 15, 78, 141 and 14 radial locations range from r/R = -0.8 to r/R = 0.8, where z is the distance from measuring port to the gas injector, D_h is the hydraulic diameter of the flow channel, r is the radial distance from the centerline of the pipe and R is the inner radius of the pipe and r/R = ±1 represent the wall on each side, the detailed information of radial measurement locations can be found in Table 2-1. Note that the actual location could slightly change for different ports because of the uncertainty from each probe. In the data processing and presentation part, the actual radial locations measured for each port are used, instead of the values in Table 2-1. The

measurement principles and probe methodology are detailed in Revankar and Ishii [56] and Kim et al. [54]. The measurement error of the probe is estimated to be less than ±10% [54]. The pressure at three probe ports is measured by a pressure transducer with an accuracy of ±0.025% of the total measurement range (100 kPa).

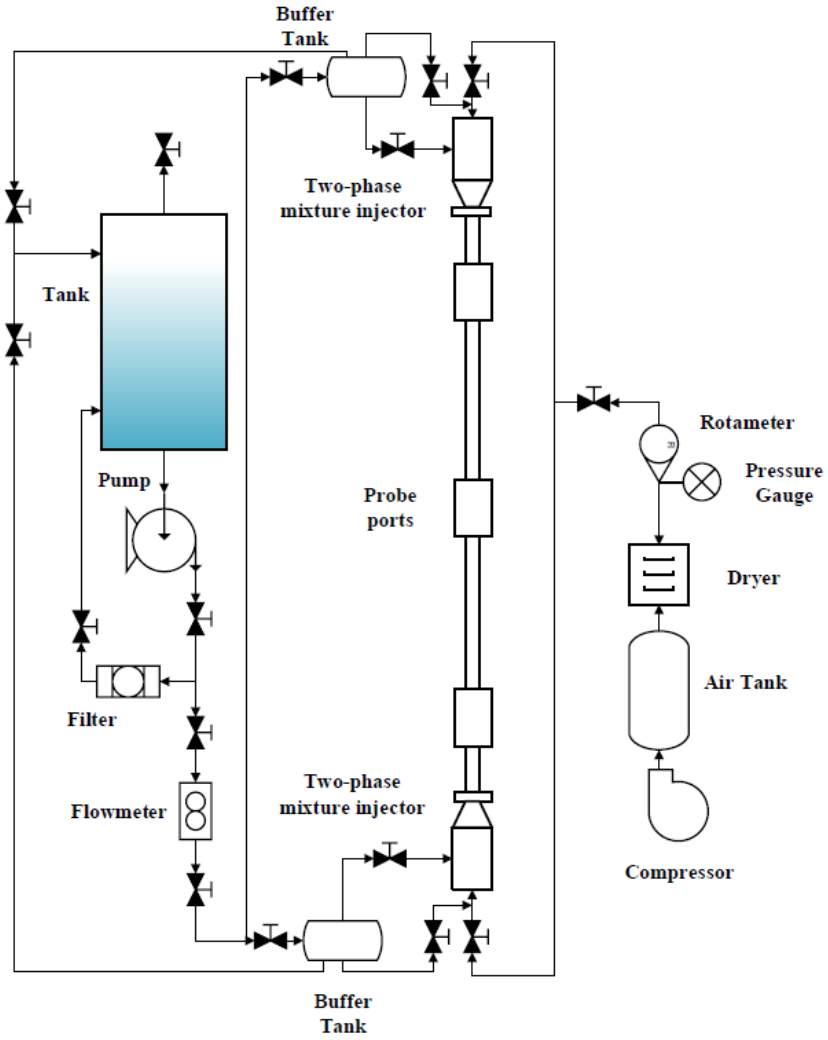

Figure 2-1 Schematic of the 25.4 mm ID round pipe facility

Table 2-1 Conductivity probe radial measurement location

Sequence #	1	2	3	4	5	6	7
Location (*r*/*R*)	0.8	0.7	0.6	0.5	0.4	0.3	0.2
Sequence#	8	9	10	11	12	13	14
Location (*r*/*R*)	0.1	0	-0.1	-0.3	-0.5	-0.7	-0.8

The experimental test matrix is presented in Fig. 2-2, and the Mishima-Ishii flow regime map [57] is also included for reference. In previous experimental studies, the test matrix was usually selected by fixing superficial gas velocity (j_g) or superficial liquid velocity (j_f) so the effect of j_g or j_f change can be investigated. But for flow regime transition, the important parameter is the void fraction instead of j_g or j_f. Therefore, the test conditions of the current experiment were selected to have similar void fraction based on the drift-flux model prediction [58], [59]. First, three superficial liquid velocities were selected, which is 0.5 m/s, 1 m/s, and 2 m/s. Then the superficial gas velocity is calculated using the drift-flux model by setting the target void fraction at 0.1, 0.15, 0.2, 0.25, 0.3, 0.35, 0.45, and 0.6, respectively. The details of flow conditions and pressure measurement results are presented in Table 2-2.

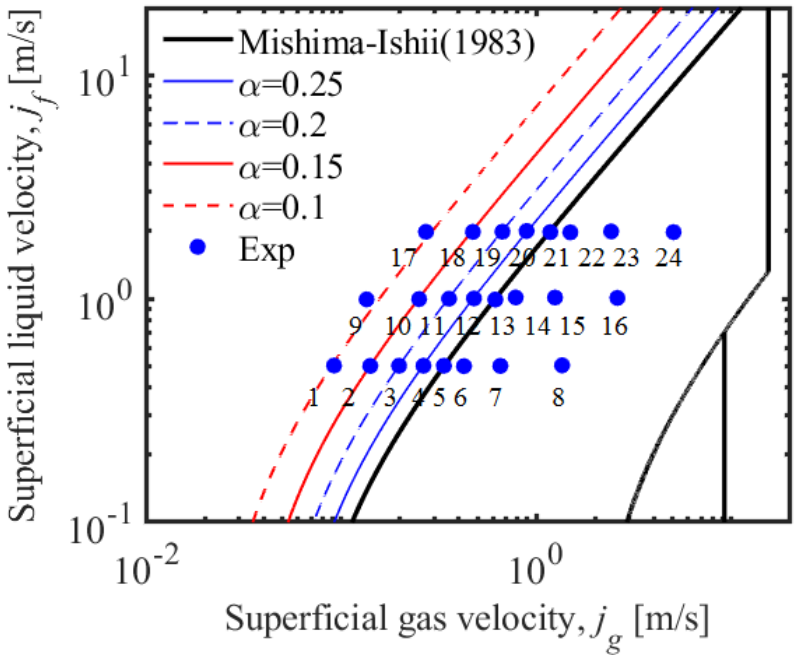

Figure 2-2 Test matrix of the round pipe experiment

Table 2-2 Inlet condition and pressure measurement result

Run#	Inlet conditions		Pressure (kPa)		
	j_f (m/s)	j_g (m/s)	z/D_h=15	z/D_h=78	z/D_h=141
1	0.502	0.092	139.159	123.176	109.387
2	0.500	0.141	138.154	122.810	109.674
3	0.501	0.198	136.316	121.852	109.355
4	0.501	0.264	134.273	120.499	108.598
5	0.501	0.336	133.057	119.871	108.462
6	0.499	0.426	130.653	118.159	107.931
7	0.500	0.654	126.918	115.311	106.300
8	0.503	1.354	122.346	112.310	105.329
9	0.992	0.135	141.917	125.202	110.243
10	0.995	0.251	140.147	124.024	109.909
11	0.999	0.357	138.654	123.154	109.682
12	1.002	0.479	137.080	122.632	109.755
13	0.990	0.616	134.911	121.252	108.800
14	1.012	0.783	133.831	120.791	108.610
15	1.011	1.245	130.436	117.766	107.118
16	1.007	2.599	128.792	116.922	107.057
17	1.990	0.272	145.543	126.796	109.314
18	1.988	0.473	145.515	127.379	110.351
19	1.992	0.670	145.371	127.625	110.987
20	2.006	0.891	145.008	127.532	111.072
21	1.983	1.178	145.002	127.975	111.626
22	1.978	1.492	144.743	127.993	111.610
23	1.997	2.415	145.157	127.920	111.190
24	1.983	5.040	152.037	133.604	114.301

2.1.2 Results Verification

The accuracy of experimental data measured by the four-sensor conductivity probe was checked against the rotameter measurement results by comparing the cross-sectional area-averaged superficial gas velocity. The local void fraction and local interfacial velocity can be measured by the conductivity probe, and the superficial gas velocity can be calculated by multiplying the local void fraction and interfacial velocity then area averaging. For the rotameter, the cross-sectional

area-averaged superficial gas velocity at each port can be calculated using the inlet rotameter result and the pressure measured at each port. The result of the comparison is shown in Fig. 2-3. It shows a good agreement of superficial gas velocity measurement between the conductivity probe and rotameter: the relative errors are less than 15% for most experimental conditions. The average error of all experimental conditions at all 3 measurement ports is 8.35%.

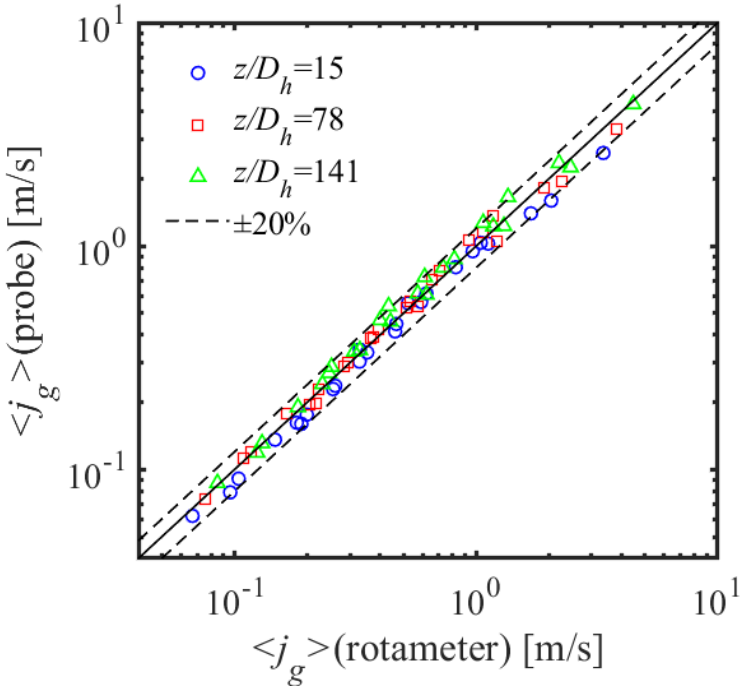

Figure 2-3 Comparison of superficial gas velocity measured by rotameter and probe

Using this rotameter evaluation can get the error of superficial gas velocity measured by probe, which is the integral product of the local void fraction and interfacial velocity, but it cannot evaluate void fraction or gas velocity separately. Even if the error of the superficial gas velocity measured by a probe is small, it is still possible that both the void fraction and interfacial velocity measurements have relatively larger errors yet these errors can offset each other. To investigate the error of void fraction and gas velocity respectively, the drift flux model was used to evaluate these experimental results, which is formulated by

$$\langle\langle v_g \rangle\rangle = \frac{\langle j_g \rangle}{\langle \alpha \rangle} = C_0 \langle j \rangle + \langle\langle V_{gj} \rangle\rangle \tag{2.1}$$

where v_g is gas velocity, j_g superficial gas velocity, α is the void fraction, C_0 is the distribution parameter, j is the sum of superficial gas and liquid velocity, and V_{gj} is the drift velocity. The

single angle brackets operator means the area-averaged value while the double angle brackets operator represents the void-weighted area-averaged value. C_0 and V_{gj} are usually given by constitutive equations [26]:

$$C_0 = \left(1.2 - 0.2\sqrt{\rho_g / \rho_f}\right)\left(1 - e^{-18\langle\alpha\rangle}\right) \tag{2.2}$$

$$\left\langle\left\langle V_{gj}\right\rangle\right\rangle = \sqrt{2}\left(\frac{\Delta\rho g\sigma}{\rho_f^{\,2}}\right)^{1/4}\left(1 - \langle\alpha\rangle\right)^{1.75} \tag{2.3}$$

To take the effect of superficial liquid velocity into account, the velocity ratio j_g/j is used to replace the α in the above constitutive equations. Given that the drift-flux model and its constitutive equations usually only apply to fully developed flow, only the velocity measured at z/D_h=141 is compared. The results are shown in Fig. 2-4. The gas velocity measured by the probe agrees well with the drift-flux model. The errors of all experimental conditions are less than 15% and the averaged error is 7.54%.

Besides, some interesting phenomena can be observed from this figure. When fixing the j_f and increasing the j_g, initially the experimental data is almost exactly located on the model prediction line, then the measured gas velocity becomes larger than the model prediction, but the increasing rate is close to the C_0 predicted by the drift-flux model. As the j_g further increasing and the area-averaged void fraction becomes higher than about 0.3, there is a change in the data slope and the measured velocity is less than the model prediction. This should result from the flow regime change from bubbly flow to slug flow. As small bubbles coalescence and form large slug bubbles, the drag characteristics, as well as the wall effect, vary significantly, therefore influence the gas velocity.

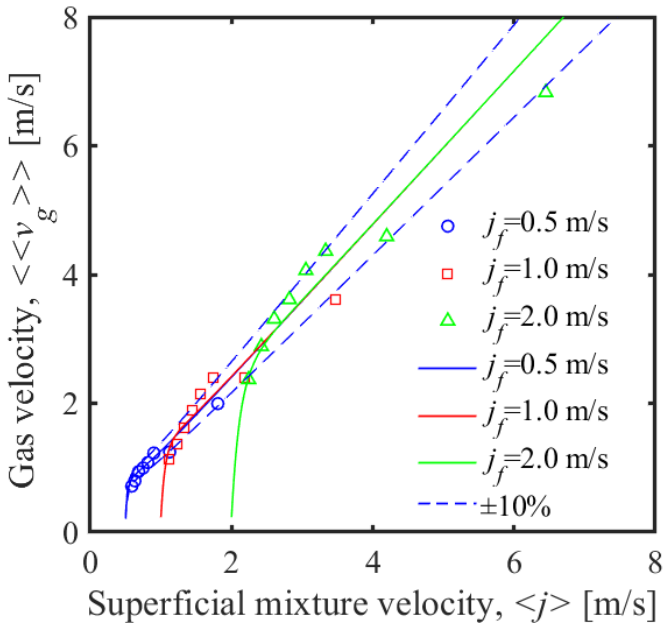

Figure 2-4 Drift-flux model evaluation

2.1.3 Experimental Results

In this section, the local measurement results including void fraction profiles, IAC profiles, and velocity profiles are presented. For each kind of profile, the effect of the superficial gas velocity is investigated by comparing flow conditions with the same superficial liquid velocity but different superficial gas velocity. Besides, the effect of superficial mixture velocity is also investigated by comparing flow conditions with similar void fraction but different superficial mixture velocity. At last, the 1-D development of void fraction and IAC is shown to help illustrate interfacial area transport at the bubbly to slug transition flow.

2.1.3.1 Void fraction

The void fraction radial distribution of Runs 10, 12, 14, and 16 are shown in Fig. 2-5. The inlet superficial liquid velocity for all these 4 conditions is about 1 m/s while the inlet superficial gas velocity is 0.25, 0.48, 0.78, and 2.60, respectively. The corresponding void fraction estimated by the drift-flux model using the inlet condition is 0.15, 0.25, 0.35, 0.6. The detailed inlet conditions can be found in Table 2-2. The left column is the group I void fraction, the middle column is the group II void fraction, and the right column is the total void fraction. From bottom to up is the void

profiles measured at the inlet port (z/D_h = 15), middle port (z/D_h = 78), and the highest port (z/D_h = 141), respectively.

For Run 10, there is no group II void fraction for all three ports, which means this flow condition is in bubbly flow, and the wall peaked void fraction distribution is observed in the inlet port. This is because the lift force working on these small spherical bubbles tends to push these bubbles towards the lower velocity region, which is the wall. As the bubble size increases, the bubble shape will no longer be a sphere and become distorted, which leads to the lift force direction to reverse and the void distribution transform from wall peaked to center peaked. This explains the wall peaked distribution becoming less obvious as the flow develops for Run 10. For Runs 12 and 14, no group II bubbles are measured at the inlet port. But as the flow develops, group II bubbles are formed at the middle and the highest port, and the void fraction profiles change from wall peaked to center peaked. For Run 16, the flow is dominated by group II bubbles even at the inlet port, and the void profile becomes flat as the flow develops.

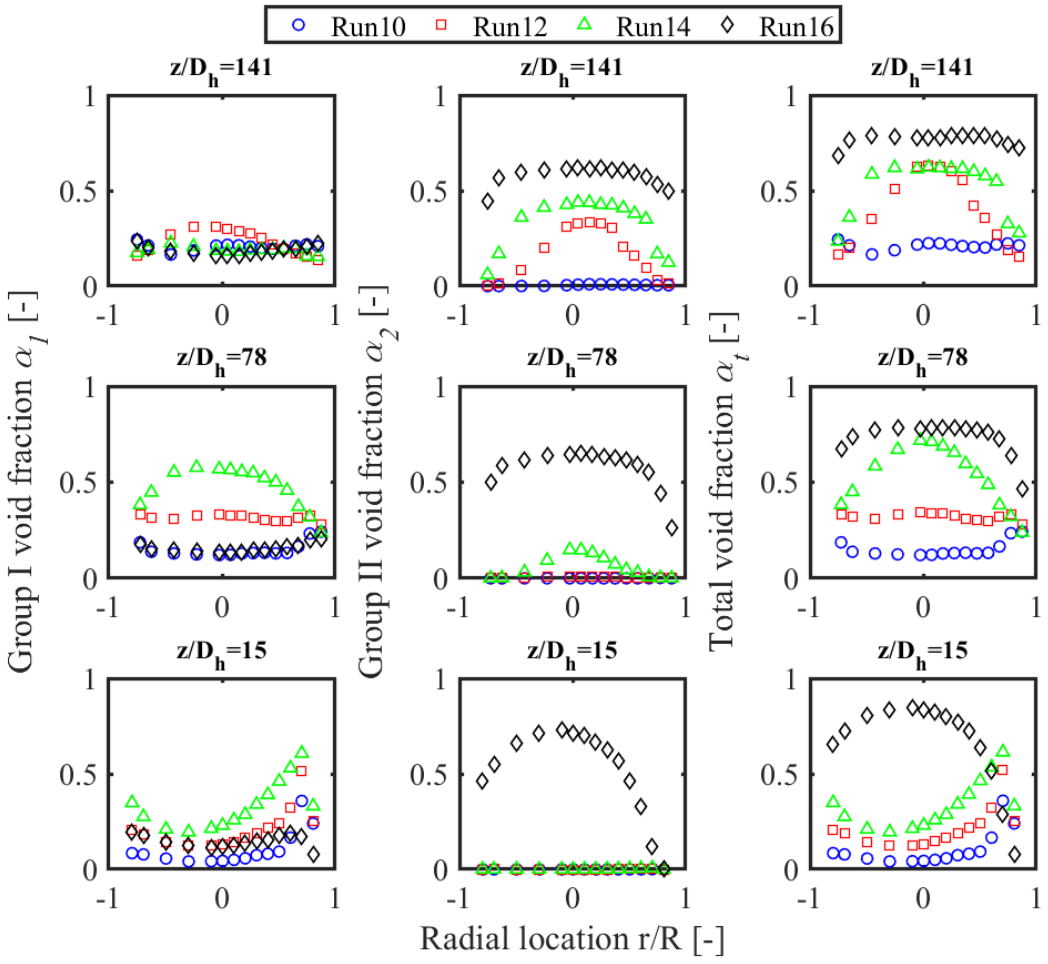

Figure 2-5 Superficial gas velocity effect on the local void fraction profile

To reach a given void fraction, multiple j_f and j_g combinations can be used. Although the area-averaged void fraction for these combinations should be similar, the radial profile, as well as the axial development trend, could be significantly different. To investigate the effect of superficial mixture velocity on flow conditions with similar void fraction, Runs 5, 13 and 21 are plotted in Fig. 2-6. The drift-flux model estimated area-averaged void fraction for these flow conditions is 0.3, which is exactly located in the bubbly to slug transition line of the Mishima-Ishii flow regime map. As shown in Fig. 2-6, although the total void fraction profiles at the highest port are similar for these three conditions, their axial development are quite different. For Runs 5 and 13, no group II bubble is detected at the inlet port, and group II bubbles are formed by bubble coalescence as the flow develops. It is interesting to note that Run 5 (j_f=0.5 m/s) has more group II bubbles than Run 13 (j_f=1.0 m/s) at the middle and the highest port. This means that the coalescence of the small

bubbles happens faster to form large bubbles at the lower superficial velocity, in other words, the intergroup void transfer is more frequent for the lower velocity conditions. This phenomenon could be attributed to a turbulence effect. As the group I bubbles coalescence, group II bubbles also disintegrate and generate some group I bubbles. The turbulence impacted disintegration of group II bubbles is an important mechanism for transferring group II void fraction to group I. As the turbulence intensity is weak in the low-velocity condition, the probability of group II bubble disintegration should be low, which explains the higher group II void fraction in the low-velocity condition.

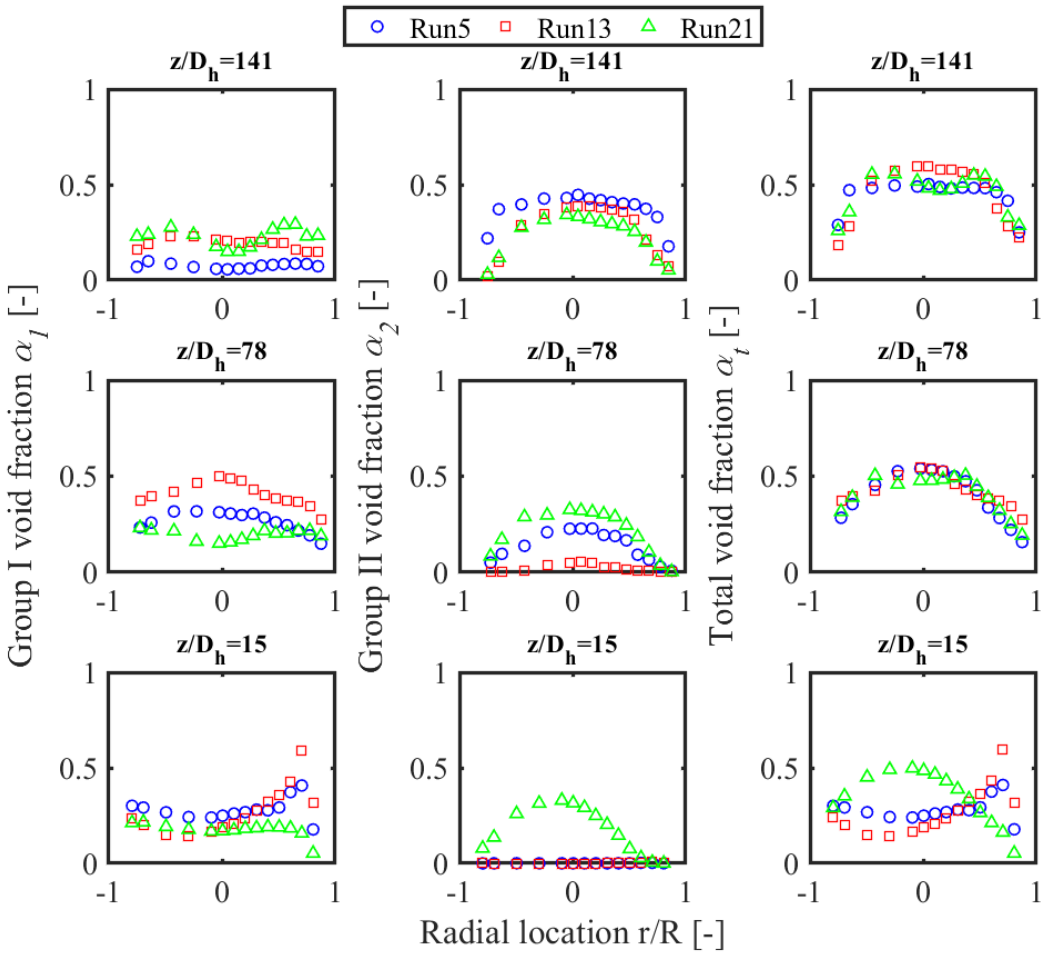

Figure 2-6 Superficial mixture velocity effect on the void fraction profile for similar void fraction conditions

2.1.3.2 Interfacial area concentration

The interfacial area concentration measurement results are presented in a similar way to the void fraction profiles. Fig. 2-7 shows the superficial gas velocity effect and Fig. 2-8 shows the superficial mixture velocity effect for flow conditions with a similar void fraction. For each figure, the left column is the group I IAC, the middle column is the group II IAC, and the right column is the total IAC.

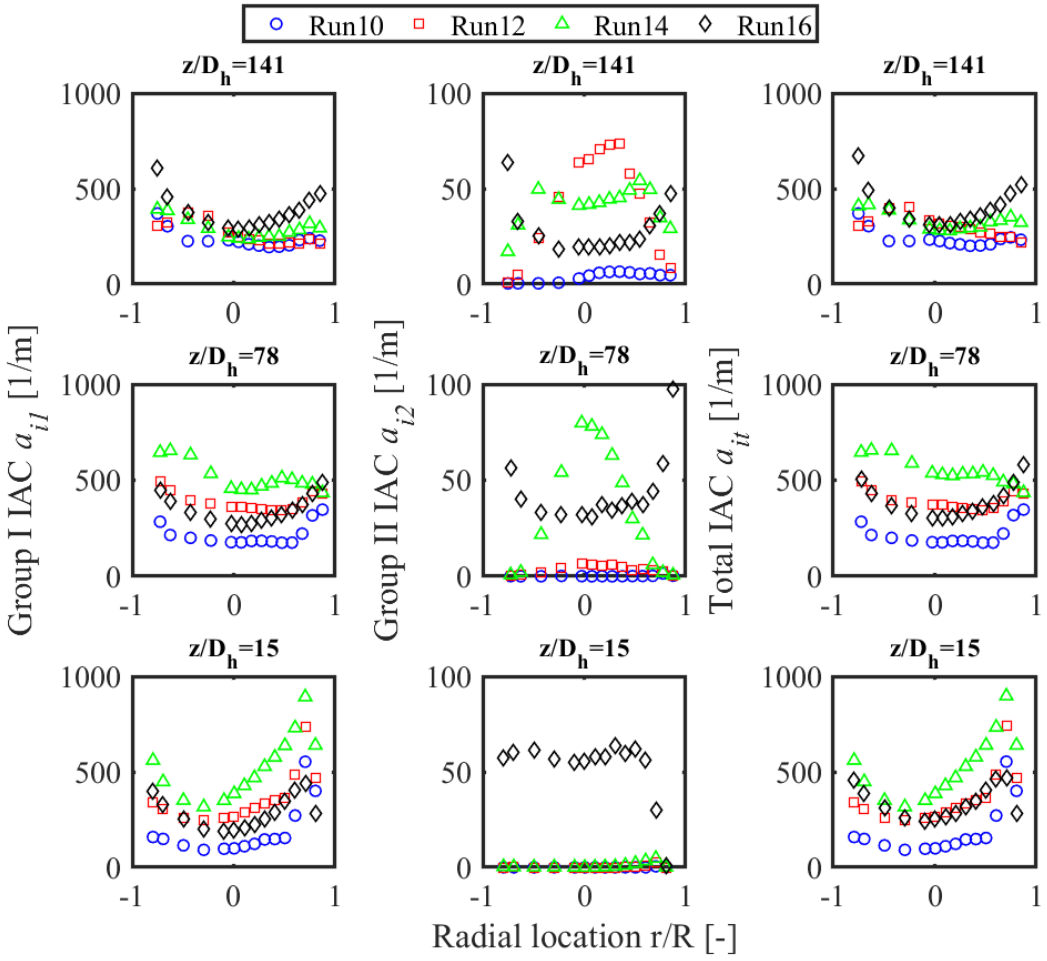

Figure 2-7 Superficial gas velocity effect on the local IAC profile

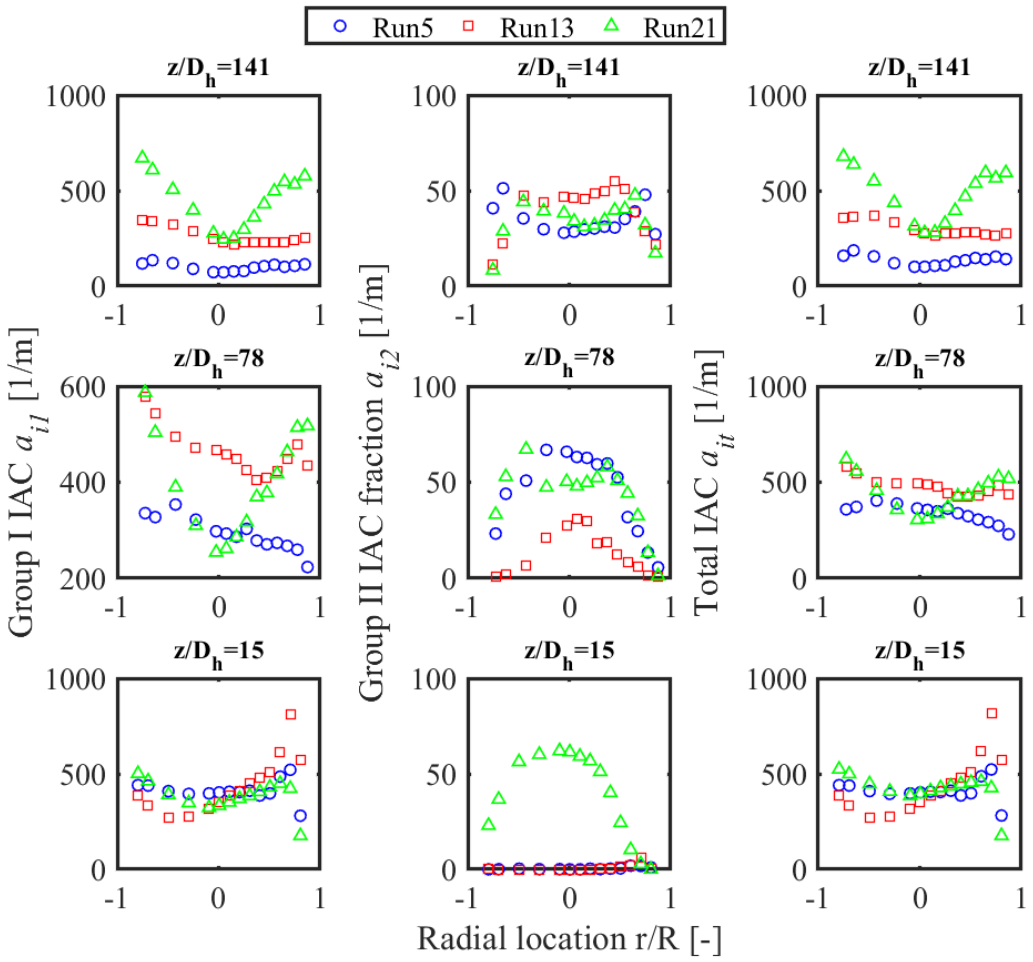

Figure 2-8 Superficial mixture velocity effect on the IAC profile for similar void fraction conditions

2.1.3.3 Gas velocity

The gas velocities for those above-mentioned flow conditions are shown in Figs. 2-9 and 2-10. The velocities of Runs 10, 12, 14, and 16 are plotted in Fig. 2-9. As the superficial gas velocity increases, the velocity gradient in the radial direction becomes larger. It should be mentioned that the uncertainty of group II bubble velocity for Runs 10, 12, and 14 could be large as few group II bubbles are detected, especially at the inlet port. The velocity of Runs 5, 13, and 21 are shown in Fig. 2-10. The radial velocity also increases with the superficial mixture velocity. The group II velocity for Runs 5 and 13 at the inlet port could be inaccurate as few group II bubbles exist for these conditions.

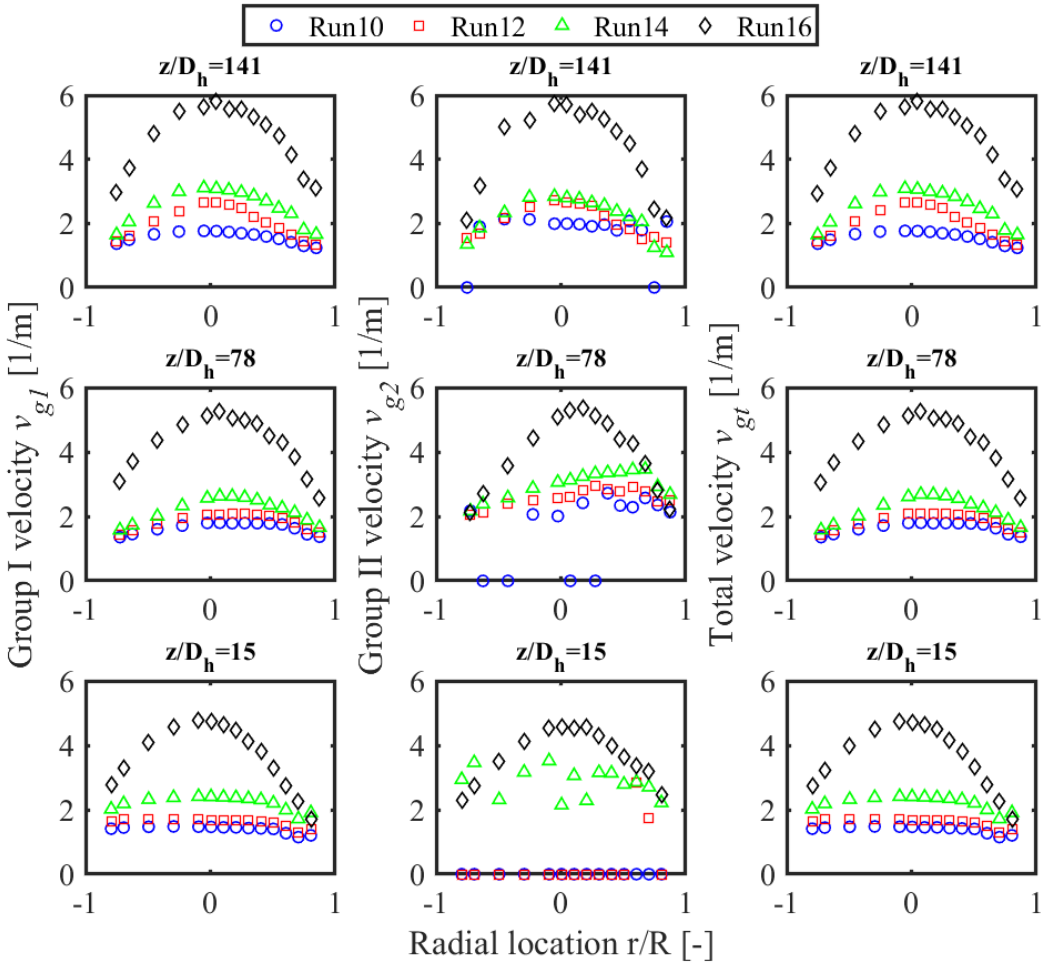

Figure 2-9 Superficial gas velocity effect on the local velocity profile

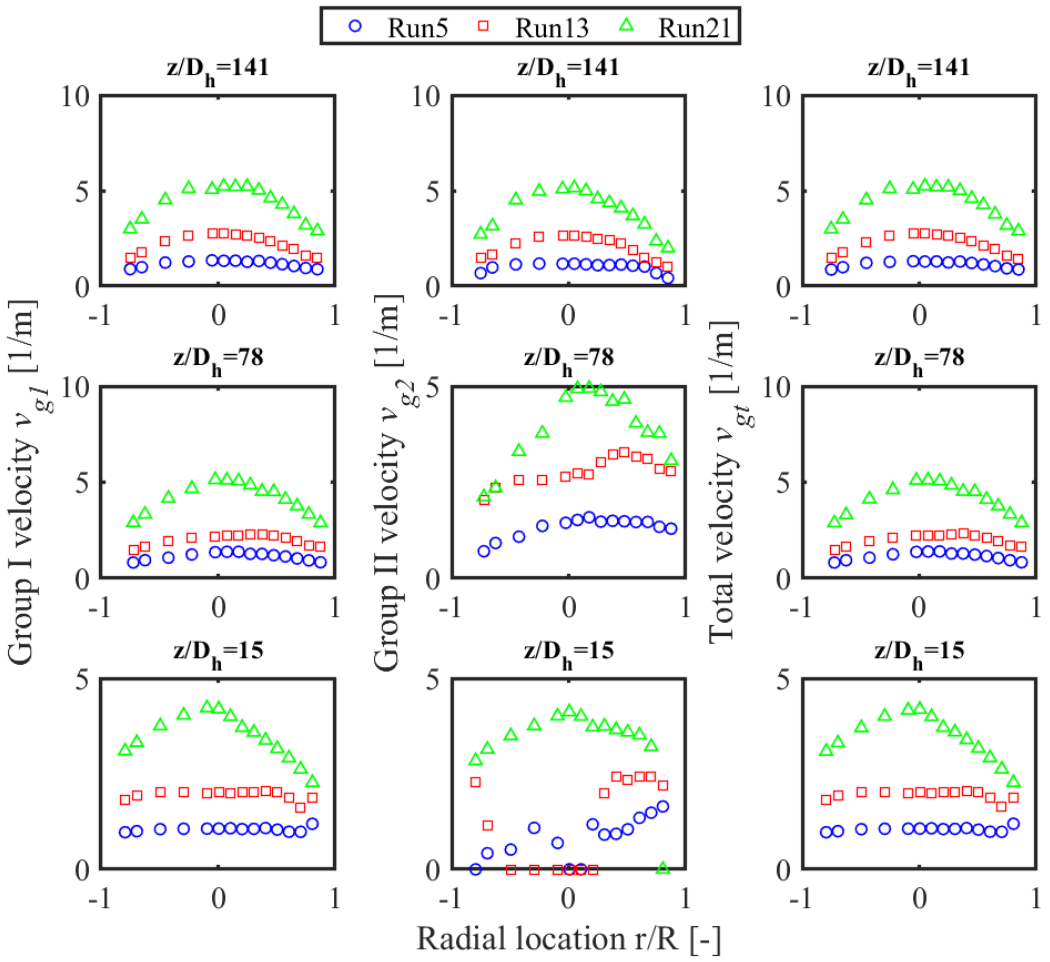

Figure 2-10 Superficial mixture velocity effect on the velocity profile for similar void fraction conditions

2.1.3.4 1-D development of void fraction and IAC

To give a better view of the axial development of the flow, the measured void fraction and IAC profiles are area-averaged and plotted in Figs. 2-11 and 2-12, respectively. In each figure, the highest, middle, and the lowest row are the flow conditions with the superficial liquid velocity of 0.5 m/s, 1.0 m/s, and 2.0 m/s. From left to right, each column has an approximated average void fraction of 0.15, 0.25, 0.35, 0.6, respectively. For flow conditions with similar void fraction but different superficial velocities, the total void fraction development trends are similar. However, the development trends for each group are different. For the low-velocity conditions (Runs 2, 4, 6, and 8), the drastic intergroup void transfer is observed in the axial direction, the group I bubbles rapidly coalescence and become group II bubbles as the flow develops. As a result, the group I

interfacial area concentration decreases rapidly in the flow direction, as shown in Fig. 2-12. For the high-velocity conditions (Runs 18, 20, 22, and 24), the intergroup void transport is less significant, as well as the IAC.

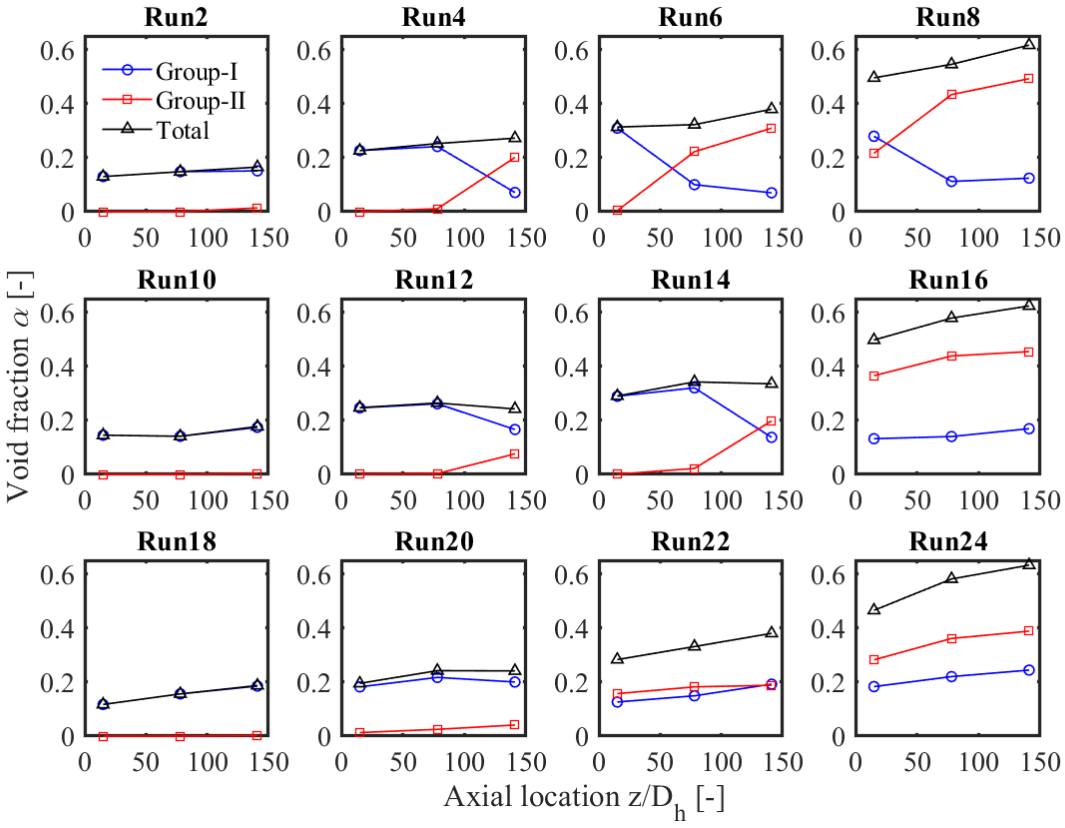

Figure 2-11 1-D development of void fraction

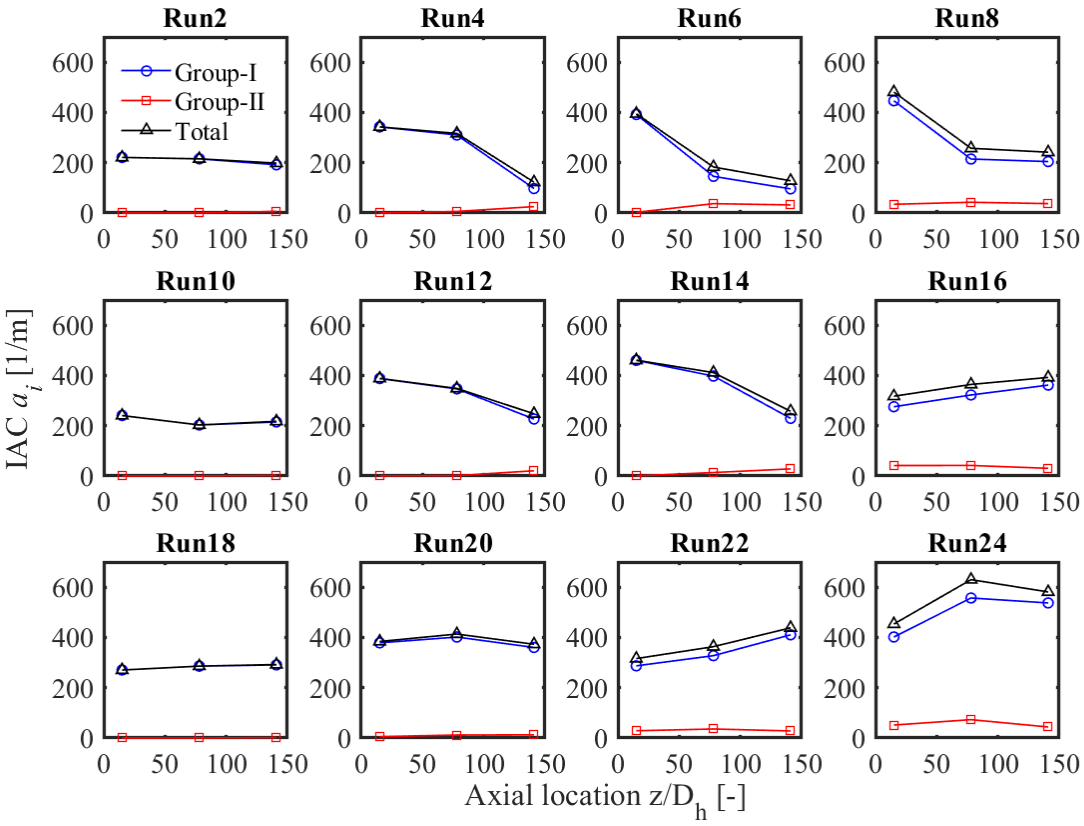

Figure 2-12 1-D development of IAC

2.2 Experiments in a 200 mm× 10 mm Narrow Rectangular Duct

The characteristics of two-phase flow in a narrow duct are different from those in a regular geometry channel, because of the restriction on the bubble shape. Although there are several experimental datasets available for the narrow rectangular channel [60]–[62], few of them [63] are focused on the bubbly to slug transition flow [64]. In this part, the objective is to perform experiments in the bubbly to slug transition flow in a narrow rectangular channel. The collected interfacial area data could be used to strengthen the understanding of the transition mechanisms and augment the current database for the IATE development.

2.2.1 Experimental Setup

The schematic of the experimental facility is shown in Fig. 2-13. The facility is designed to run adiabatic air-water upward two-phase flows at atmospheric pressure and room temperature. It

consists of air and water supply systems, a two-phase mixing section, a test section, an instrumentation system, and an upper plenum. The test section is a 200 mm ×10 mm rectangular duct which is made of acrylic. The height of the test section is around 3 m. The water is supplied by a centrifugal pump and the air is delivered by an air compressor through a compressed air tank. The water flow rate is measured by a vortex flowmeter with ±2% error of full scale for high flow rate, and the rotameters with ±2% error of full scale is used to measure the low flow rate. The airflow rate is also measured by several rotameters with an accuracy of ±2% of the full-scale reading. Three instrumentation ports are installed in the test section at three axial locations z/D_h=30.9, 81.6, and 132.3, which are equipped with four-sensor conductivity probes [54] to measure the void fraction, IAC, and interface velocity. For one flow condition, 36 cross-sectional locations are measured at each port, as presented in Fig. 2-14. It has been experimentally shown that the flow is symmetric in both *x* and *y* directions in a previous study [62], therefore the cross-sectional profile can be built based on measured points and symmetry. The measured bubbles are divided into two groups based on the critical bubble diameter D_{c1} for narrow channels, which can be expressed as [19]:

$$D_{c1} = 1.7G^{1/3}\left(\frac{\sigma}{g\Delta\rho}\right)^{1/3} \tag{2.4}$$

which is 7.1 mm for the current experimental system. G is the gap size, which is 10 mm for the current facility, σ is surface tension, g is gravity, and $\Delta\rho$ is the density difference. This equation is derived for rectangular ducts with the gap size less than the maximum distorted bubble size, which is 10.9 mm for the air-water two-phase flow under the normal condition. The sampling frequency is 100 kHz, which is much higher than previous experiments (20 kHz) [61], [62] to get more accurate velocity measurement, and the sampling time is 60 s. The measurement accuracy for void fraction and IAC using a four-sensor conductivity probe is around ±5% and ±10%, according to previous benchmark tests [54].

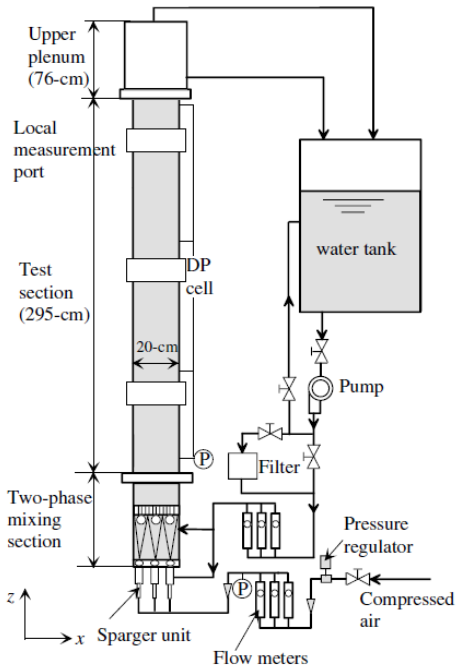

Figure 2-13 Schematic of the Experimental Facility

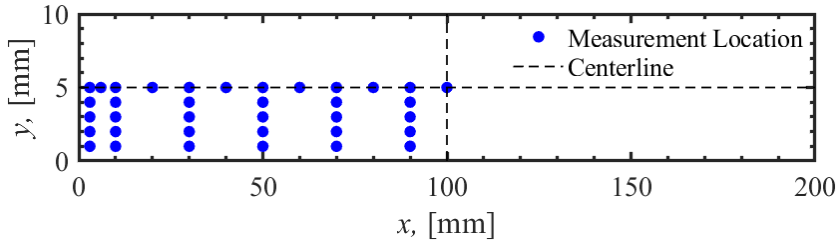

Figure 2-14 Four-sensor Conductivity Probe Measurement Mesh

Experiments were performed at eight flow conditions, as plotted in Fig. 2-15. In previous studies, the bubbly to slug flow regime transition criteria was given as void fraction α=0.3, and it could be plotted in a j_g-j_f graph using the drift-flux model [57][65]. However, previous experiment results indicate that the flow regime transition in narrow rectangular channels could happen earlier and the transition is almost completed when α reaches 0.3 [60]. Besides, the previous test matrix was selected by fixing j_g or j_f so the effect of j_g or j_f change can be investigated. But for flow regime transition, the important parameter is void fraction instead of j_g and j_f, therefore the test conditions of the current experiment were selected with similar void fraction but different j_g and j_f. The details of flow conditions and pressure measurement results are presented in Table 2-3.

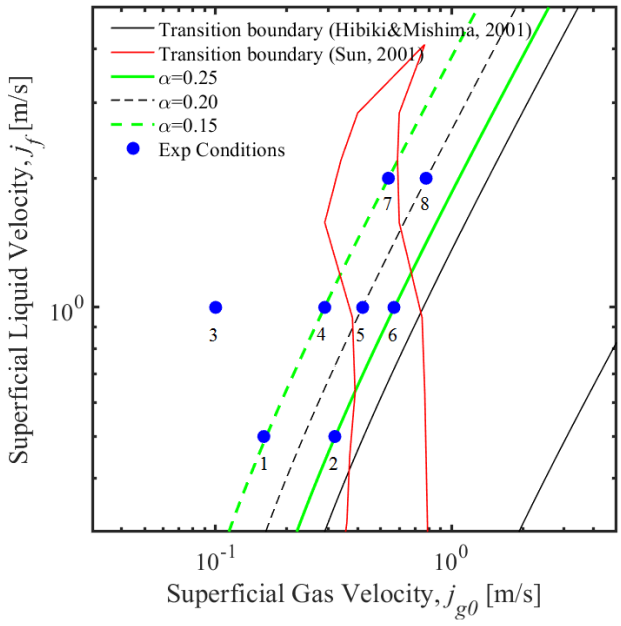

Figure 2-15 Test Matrix

Table 2-3 Summary of test conditions and the pressure measurement results

Run#	Inlet conditions (m/s)		Local absolute pressure (kPa)		
	j_f	j_{g0}	z/D_h=30.9	z/D_h=81.6	z/D_h=132.3
1	0.50	0.16	123.762	114.567	105.673
2	0.50	0.32	121.953	113.357	105.247
3	1.02	0.10	125.769	115.899	106.175
4	1.04	0.29	124.980	115.533	106.108
5	1.01	0.42	124.197	115.066	105.846
6	1.00	0.57	123.647	114.600	105.709
7	2.02	0.54	129.130	117.255	105.388
8	2.00	0.77	128.642	116.978	105.271

2.2.2 Results Verification

To verify the accuracy of the local data measured by the four-sensor conductivity probe, the measurement results were cross-checked against the superficial gas velocity measured by the rotameter. For the conductivity probe, the area-averaged superficial gas velocity can be expressed as the production of the area-averaged void fraction and the void-weighted area-averaged gas velocity, and these two parameters can be calculated from the local data measured by the probe. Therefore, the superficial gas velocities measured by the rotameter and the conductivity probe

could be compared with each other. The comparison result is shown in the left part of Fig. 2-16. For most flow conditions and axial locations, the difference between the probe measurement and the rotameter measurement is less than 15%, and the overall average relative error is 8.01%. Besides, the area-averaged void fraction measured by the probe was also compared with the drift-flux model prediction. Equations (2.1) and (2.3) are still applicable to the rectangular channel, while the distribution parameter should be calculated using [26]:

$$C_0 = \left(1.35 - 0.35\sqrt{\rho_g/\rho_f}\right)\left(1 - e^{-18\langle\alpha\rangle}\right) \tag{2.5}$$

Then the gas velocity can be calculated, and the area-averaged void fraction can be predicted by dividing the measured superficial gas velocity by the gas velocity. The comparison of the void faction measured by the conductivity probe and the drift-flux model prediction is presented in the right part of Fig. 2-16. The overall average relative error is 12.34%.

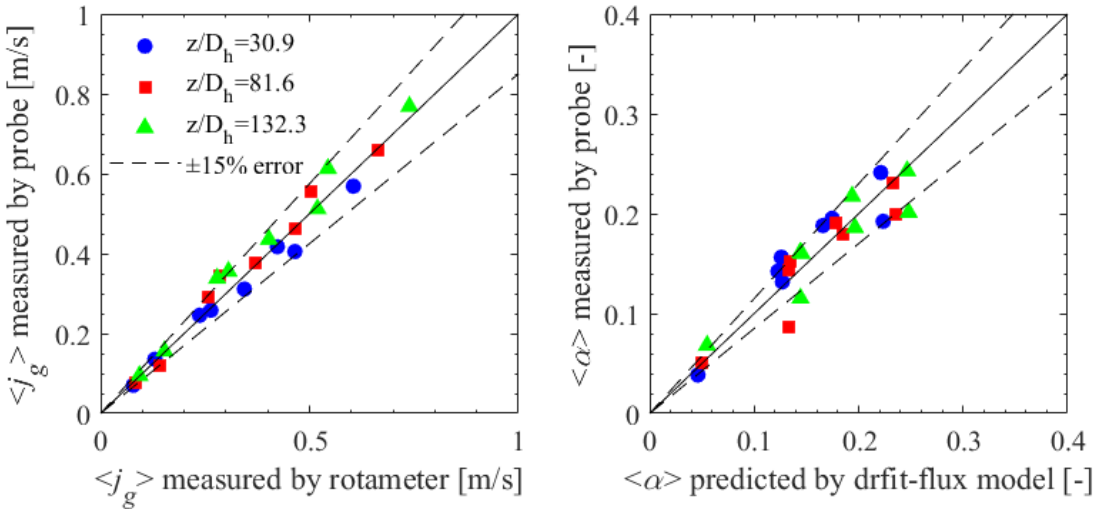

Figure 2-16 Measurement Results: Rotameter Cross Check (left) and Drift-flux Model Check (right)

2.2.3 Local Measurement Results

Fig. 2-17 shows the two-group void fraction distributions at three axial locations for Run 4 (j_f=1.04 m/s, j_{g0}=0.29 m/s). Each sub-figure represents the left half of the channel and it is acquired by interpolating the local measurement results. It is observed that the flow is still developing since the void fraction distribution changes significantly along the axial direction. The left part shows the group I void fraction axial development. At the lowest port (z/D_h=30.9), the group I bubble shows wall peak distribution in the y-direction (10 mm). At the middle (z/D_h=81.6) and highest

(z/D_h=132.3) port, the variation of group I void fraction over the entire cross-section is not significant. The maximum group I void fraction is less than 8% for this flow condition. The group II void fraction is presented in the right part of Fig. 2-17. In the x-direction (200 mm), the group II void fraction peaks near the left wall (x=30 mm) at the lowest port but shows center-peaked distribution (x=100 mm) at the highest port. At the middle port, the distribution shows transition characteristics and peaks at x=50 mm. Pictures were also taken for this flow condition at the locations right below the lowest port and the highest port, which is presented in Fig. 2-18. The width of these flow visualization images is 200 mm, and the flow direction is from the bottom to the top. These images can help support the measured void fraction axial development. At the inlet section, the cap turbulent bubbles tend to appear near the sidewall, while at the top section they coalescence into a larger bubble that occupies half of the channel and locates in the channel center.

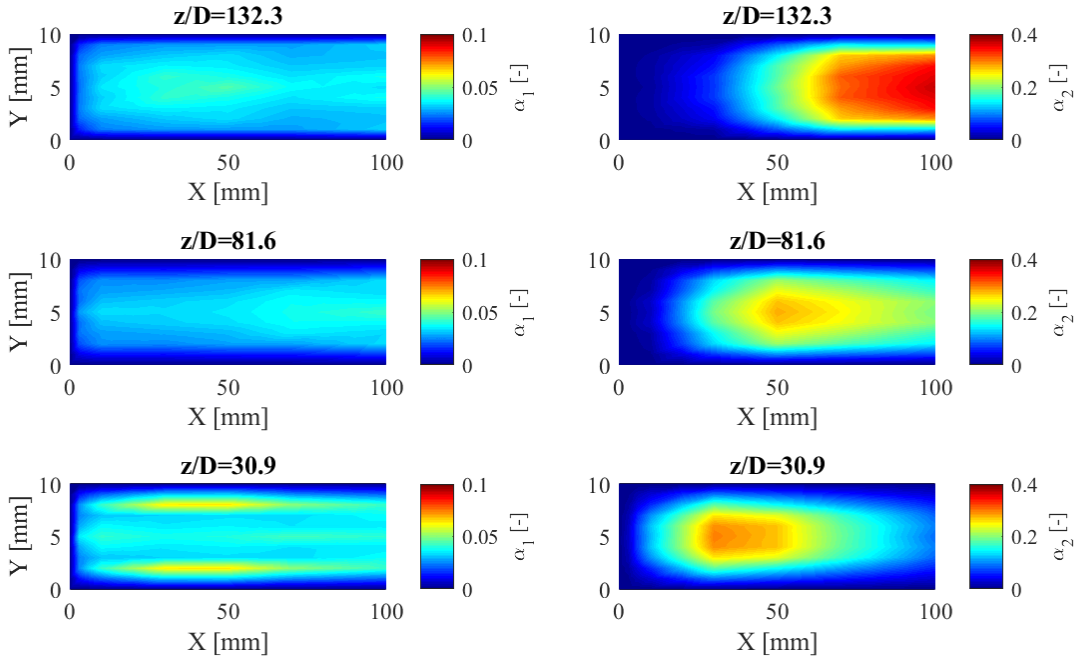

Figure 2-17 Group I (left) and Group II (right) Void Fraction Distribution of Run 4 (j_f=1.04 m/s, j_{g0}=0.29 m/s)

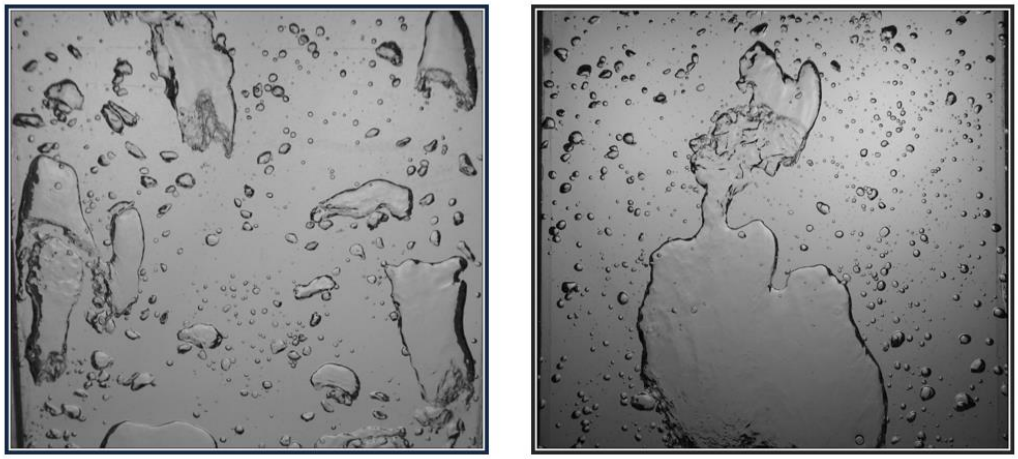

Figure 2-18 Pictures of Run 4 (j_f=1.04 m/s, j_{g0}=0.29 m/s) at z/D_h=20 (left) and z/D_h=121 (right)

As mentioned in section 2.2.1, the test matrix was determined based on the fixed void fraction curves, which were plotted using the drift-flux model. Runs 4 and 7 were located on the curve corresponds to α=0.15, Runs 5 and 8 were located on α=0.20, and Runs 2 and 6 were located on α=0.25. The comparisons of void fraction, IAC, and bubble velocity of these flow conditions at z/D_h=132.3 are shown in Fig. 2-19. It should be mentioned that the data presented in this figure is line averaged along the y-direction (10 mm gap) to emphasize the distribution in the x-direction. In Fig. 2-19, group I data are plotted in blue symbols and lines while group II data are plotted in red. Besides, for each comparison group, the flow conditions with lower j_f (Runs 2, 4, and 5) were represented by empty symbols and higher j_f conditions (Runs 6, 7, and 8) were represented by solid symbols. For Runs 4 and 7, although the area-averaged void fraction of these two conditions are similar, the void fraction distributions are quite different. Run 4 is center-peaked while Run 7 peaks at x=50 mm. Given that Run 4 is also developed from side peak to center peak, it can be inferred that Run 7 is still not fully developed at the highest port. The superficial liquid velocity of Run 7 is about twice of that of Run 4, therefore a longer development length is required. Although the group I void fraction is much less than group II for both runs, group I IAC is the major part of the total interfacial area. The size of group I bubbles are much smaller than group II bubbles, therefore the surface to volume ratio of group I bubbles is larger. The group I IAC of Run 7 is about twice of the group I IAC of Run 4. This is because the higher superficial mixture velocity of Run 7 results in more turbulence, which facilitates the disintegration of large bubbles and the generation of small bubbles. The void fraction and IAC profile for Run 5 and 8 are quite close to

Runs 4 and 7, except the void fraction and IAC increase a little due to the higher inlet superficial gas velocity. As to the bubble velocity, the trends for both groups are similar. For Runs 7 and 8, the velocity profile is close to a turbulent velocity profile, which is characterized by a flat region in the center. Besides, the velocity gradients of Runs 4 and 5 are much larger than that of Runs 7 and 8. This is because of a secondary flow effect induced by the large bubbles in the channel center. If the liquid velocity is low, the liquid flow near the sidewall could circulate at some height instead of going upward, with large bubbles periodically going upward at a high speed. If the liquid velocity is high enough, like Runs 7 and 8, the secondary flow effect would be negligible. For Runs 2 and 6, the void fraction profiles are center-peaked while the IAC and velocity profiles are close to other flow conditions.

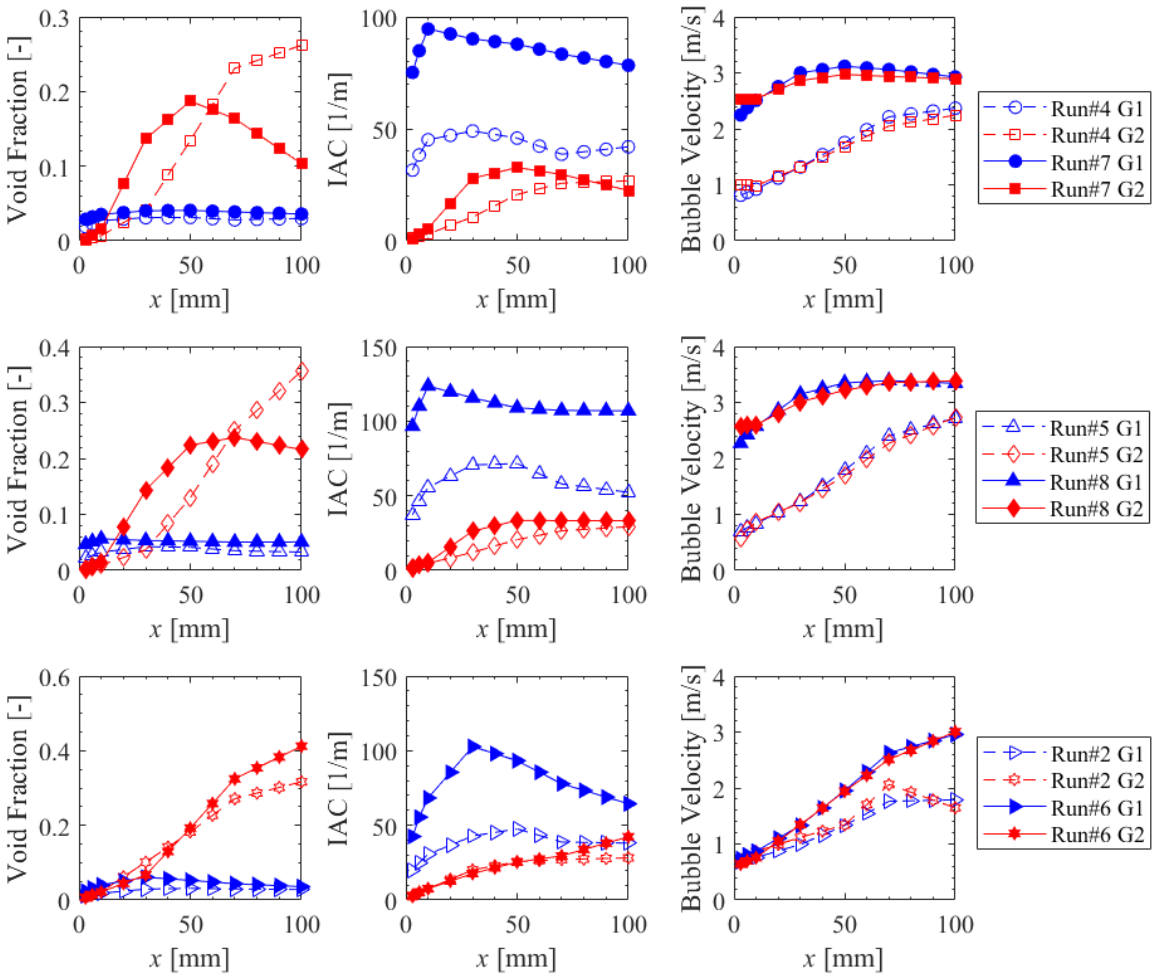

Figure 2-19 Local Measurement Results Comparison of Various Flow Conditions at z/D_h=132

3. MODEL DEVELOPMENT FOR BUBBLY TO SLUG TRANSITION FLOW

3.1 Two-group Interfacial Area Transport Equation

3.1.1 Formulation of Two-group IATE

The two-group interfacial area transport equation is given as [26]:

$$\frac{\partial a_{i1}}{\partial t}+\nabla\cdot\left(a_{i1}v_{gi1}\right)=\frac{2}{3}\frac{a_{i1}}{\alpha_1}\left[\frac{\partial\alpha_1}{\partial t}+\nabla\cdot\left(\alpha_1 v_{g1}\right)-\eta_{ph1}\right] - \chi D_{c1}^{*2}\frac{a_{i1}}{\alpha_1}\left[\frac{\partial\alpha_1}{\partial t}+\nabla\cdot\left(\alpha_1 v_{g1}\right)-\eta_{ph1}\right]+\sum_j\phi_{j,1}+\phi_{ph1} \tag{3.1}$$

and

$$\frac{\partial a_{i2}}{\partial t}+\nabla\cdot\left(a_{i2}\boldsymbol{v}_{gi2}\right)=\frac{2}{3}\frac{a_{i2}}{\alpha_2}\left[\frac{\partial\alpha_2}{\partial t}+\nabla\cdot\left(\alpha_2\boldsymbol{v}_{g2}\right)-\eta_{ph2}\right] + \chi D_{c1}^{*2}\frac{a_{i1}}{\alpha_1}\left[\frac{\partial\alpha_1}{\partial t}+\nabla\cdot\left(\alpha_1\boldsymbol{v}_{g1}\right)-\eta_{ph1}\right]+\sum_j\phi_{j,2}+\phi_{ph2} \tag{3.2}$$

The left-hand sides of Eq. (3.1) and (3.2) are the time derivative and the advection of the IAC for each group, respectively. The first right-hand side terms are the intragroup expansion/contraction source/sink terms. These terms account for the IAC change due to the expansion/contraction of existing particles (bubbles) within each group. The second RHS terms are the intergroup expansion/contraction source/sink terms, which represents the IAC change due to the expansion/contraction of particles across the group boundary. k=1 and 2 for group I and II, respectively. α_k, a_{ik}, v_{gik}, and v_{gk} is the void fraction, interfacial area concentration, interfacial velocity, and gas phase velocity for group k, respectively. η_{phk} is the source/sink for the void fraction due to phase change (nucleation/collapse), and $\phi_{j,k}$ is the source/sink for the interfacial area concentration due to j^{th}-type bubble interactions mechanisms for group k bubbles. χ is the inter-group transfer coefficient at the group boundary. D_{c1}^{*} is the non-dimensional bubble diameter defined by:

$$D_{c1}^{*}=\frac{D_c}{D_{\mathrm{sm1}}} \tag{3.3}$$

where D_c is defined by Eq. (3.4). D_{sm1} is the Sauter mean diameter of group-1 bubbles.

$$D_c = 4\sqrt{\frac{\sigma}{g\Delta\rho}} \tag{3.4}$$

Besides, the continuity equations, also referred as void transport equation, for each group are given as:

$$\frac{\partial\left(\alpha_{g1}\rho_g\right)}{\partial t} + \nabla\left(\alpha_{g1}\rho_g v_{g1}\right) = \Gamma_{g1} - \Delta\dot{m}_{12} \tag{3.5}$$

$$\frac{\partial\left(\alpha_{g2}\rho_g\right)}{\partial t} + \nabla\left(\alpha_{g2}\rho_g v_{g2}\right) = \Gamma_{g2} + \Delta\dot{m}_{12} \tag{3.6}$$

where Γ_{g1}, Γ_{g2} are the source for group I and II bubbles, and $\Delta\dot{m}_{12}$ is the inter-group mass transfer term, which can be calculated using void inter-group transfer terms η_j^{inter} and the density change. Usually in the adiabatic two-phase flow, $\Gamma_{g1} = \Gamma_{g2} = 0$.

As mentioned in section 1.2.1, recently Worosz [28] pointed out that the effect of the intergroup transfer is double-counted in the current IATE formulation, and a revised two-group IATE is proposed [28] to remove the intergroup transfer effects from the expansion/contraction source terms in Eq. (3.1) and (3.2):

$$\begin{aligned}\frac{\partial a_{i1}}{\partial t} + \nabla\cdot\left(a_{i1}\boldsymbol{v}_{gi1}\right) &= \frac{2}{3}\frac{a_{i1}}{\alpha_1}\frac{1}{1-\chi D_{c1}^{*3}}\left[\frac{\partial\alpha_1}{\partial t} + \nabla\cdot\left(\alpha_1\boldsymbol{v}_{g1}\right) - \eta_{\text{ph1}} - \sum_j \eta_{j,1}^{\text{inter}}\right] \\ &- \chi D_{c1}^{*2}\frac{a_{i1}}{\alpha_1}\frac{1}{1-\chi D_{c1}^{*3}}\left[\frac{\partial\alpha_1}{\partial t} + \nabla\cdot\left(\alpha_1\boldsymbol{v}_{g1}\right) - \eta_{\text{ph1}} - \sum_j \eta_{j,1}^{\text{inter}}\right] + \sum_j \phi_{j,1} + \phi_{\text{ph1}}\end{aligned} \tag{3.7}$$

$$\begin{aligned}\frac{\partial a_{i2}}{\partial t} + \nabla\cdot\left(a_{i2}\boldsymbol{v}_{gi2}\right) = \frac{2}{3}\frac{a_{i2}}{\alpha_2}\Bigg\{&\frac{\partial\alpha_2}{\partial t} + \nabla\cdot\left(\alpha_2\boldsymbol{v}_{g2}\right) - \eta_{\text{ph2}} \\ &- \frac{1}{1-\chi D_{c1}^{*3}}\left[\sum_j \eta_{j,1}^{\text{inter}} + \chi D_{c1}^{*3}\left(\frac{\partial\alpha_1}{\partial t} + \nabla\cdot\left(\alpha_1\boldsymbol{v}_{g1}\right) - \eta_{\text{ph1}}\right)\right]\Bigg\} \\ &+ \chi D_{c1}^{*2}\frac{a_{i1}}{\alpha_1}\frac{1}{1-\chi D_{c1}^{*3}}\left[\frac{\partial\alpha_1}{\partial t} + \nabla\cdot\left(\alpha_1\boldsymbol{v}_{g1}\right) - \eta_{\text{ph1}} - \sum_j \eta_{j,1}^{\text{inter}}\right] \\ &+ \sum_j \phi_{j,2} + \phi_{\text{ph2}}\end{aligned} \tag{3.8}$$

3.1.2 Constitutive Modeling of Bubble Coalescence and Break-up Mechanisms

Bubble coalescence and break-up mechanisms are modeled as constitutive equations of IATE. For bubble coalescence, the random collision (RC) driven by turbulent eddies and the wake entrainment (WE) effect of a bubble following a preceding bubble are considered as major mechanisms. For bubble disintegration, the turbulent impact (TI), shearing-off (SO) of large bubbles, and the surface instability (SI) are recognized as major mechanisms. Table 3-1 summarizes the major bubble interaction mechanisms for two-group IATE. For example, $\phi_{RC,1}^{(11,2)}$ represents the sink terms of group I IAC due to the random collision of two group I bubbles, which generates a group II bubble. It should be mentioned that there are several kinds of these IAC source/sink constitutive models [18], [23], [29], [30], which are developed to characterize different flow channels such as moderate and large diameter pipes, rectangular flow channels, etc. Fu and Ishii [18] developed a comprehensive set of IAC source/sink models for moderate size round pipes and benchmarked against 48.3 mm ID round pipe data. The detailed formulations are presented in the Appendix A. Given that this model is developed for a moderate pipe diameter, the source/sink terms resulting from the random collision of group II bubbles ($\phi_{RC,2}^{(2)}$, $\phi_{RC,k}^{(12,2)}$,), turbulence impact on group II bubbles ($\phi_{TI}^{(2)}$) and the surface instability ($\phi_{SI}^{(2)}$) are not taken into account. In this study these terms are adopted to predict the data collected in a 25.4 mm ID pipe. In addition two recent models by Worosz [28] and Doup [32], as discussed in section 1.2.2, are also evaluated using the 25.4 mm ID pipe data.

Table 3-1 Major two-group bubble interaction mechanism [18]

Mechanism	Interaction	a_i Source/sink term	a_i Source/sink
Random-Collision (RC)	(1)+(1)→(1)	$\phi_{RC}^{(1)}$	G1 sink
	(1)+(1)→(2)	$\phi_{RC,1}^{(11,2)}$, $\phi_{RC,2}^{(11,2)}$	G1 sink, G2 source
	(1)+(2)→(2)	$\phi_{RC,1}^{(12,2)}$, $\phi_{RC,2}^{(12,2)}$	G1 sink, G2 source
	(2)+(2)→(2)	$\phi_{RC}^{(2)}$	G2 sink
Wake-Entrainment (WE)	(1)+(1)→(1)	$\phi_{WE}^{(1)}$	G1 sink
	(1)+(1)→(2)	$\phi_{WE,1}^{(11,2)}$, $\phi_{WE,2}^{(11,2)}$	G1 sink, G2 source
	(1)+(2)→(2)	$\phi_{WE,1}^{(12,2)}$, $\phi_{WE,2}^{(12,2)}$	G1 sink, G2 source
	(2)+(2)→(2)	$\phi_{WE}^{(2)}$	G2 sink
Turbulence-Impact (TI)	(1) →(1)+(1)	$\phi_{TI}^{(1)}$	G1 source
	(2) →(2)+(2)	$\phi_{TI}^{(2)}$	G2 source
Surface-Instability (SI)	(2) →(2)+(2)	$\phi_{SI}^{(2)}$	G2 source
Shearing-Off (SO)	(2) →(2)+(1)	$\phi_{SO,1}^{(2,12)}$, $\phi_{SO,2}^{(2,12)}$	G1 source, G2 sink

3.2 IATE Evaluation Approach

In system safety analysis codes like TRACE and RELAP5, the one-dimensional (1-D) model is used to predict the flow behavior and system transient. Given the practical significance of the 1-D model, the IATE is evaluated in the 1-D form in this study. To obtain the one-dimensional form of two-group IATE, two types of averaging methods are required: area-average and void fraction-weighted area-average, which is defined by Eq. (3.9) and (3.10), respectively, where A is the cross-sectional area of the flow duct.

$$\langle \xi \rangle \equiv \frac{1}{A}\int_A \xi(x,y)\,\mathrm{d}A \tag{3.9}$$

$$\langle\langle \xi \rangle\rangle \equiv \frac{\int_A \alpha(x,y)\xi(x,y)\mathrm{d}A}{\int_A \alpha(x,y)\mathrm{d}A} = \frac{\frac{1}{A}\int_A \alpha(x,y)\xi(x,y)\mathrm{d}A}{\langle \alpha \rangle} \tag{3.10}$$

From Eq. (3.7) and (3.8), interfacial velocities $\langle\langle \upsilon_{gi1} \rangle\rangle$ and $\langle\langle \upsilon_{gi2} \rangle\rangle$ are required to solve the IATE. Although the interfacial velocity could be slightly different from the gas phase velocity, given the

practicality of the model, it is assumed that the interfacial velocity of each group can be approximated by gas velocities $\left\langle\left\langle \upsilon_{g1}\right\rangle\right\rangle$ and $\left\langle\left\langle \upsilon_{g2}\right\rangle\right\rangle$. This assumption has been widely used in previous IATE research [18], [28], [29]. Then the steady-state, one-dimensional, two-group, IATE and void transport equations for adiabatic two-phase flow are given as:

$$\frac{\partial}{\partial z}\left(\left\langle a_{i1}\right\rangle\left\langle\left\langle \upsilon_{g1}\right\rangle\right\rangle\right)=\left\langle \phi_{1,\exp}\right\rangle+\left\langle \phi_{RC}^{(1)}\right\rangle+\left\langle \phi_{WE}^{(1)}\right\rangle+\left\langle \phi_{TI}^{(1)}\right\rangle+\left\langle \phi_{SO,1}^{(2,12)}\right\rangle +\left\langle \phi_{RC,1}^{(11,2)}\right\rangle+\left\langle \phi_{WE,1}^{(11,2)}\right\rangle+\left\langle \phi_{WE,1}^{(12,2)}\right\rangle-\left\langle \phi_{\exp 12}\right\rangle \tag{3.11}$$

$$\frac{\partial}{\partial z}\left(\left\langle a_{i2}\right\rangle\left\langle\left\langle \upsilon_{g2}\right\rangle\right\rangle\right)=\left\langle \phi_{2,\exp}\right\rangle+\left\langle \phi_{WE}^{(2)}\right\rangle+\left\langle \phi_{SO,2}^{(2,12)}\right\rangle+\left\langle \phi_{RC,2}^{(11,2)}\right\rangle+\left\langle \phi_{WE,2}^{(11,2)}\right\rangle+\left\langle \phi_{WE,2}^{(12,2)}\right\rangle+\left\langle \phi_{\exp 12}\right\rangle \tag{3.12}$$

$$\frac{\partial}{\partial z}\left(\left\langle \alpha_1\right\rangle\left\langle\left\langle \upsilon_{g1}\right\rangle\right\rangle\right)=\frac{\left\langle \alpha_1\right\rangle\left\langle\left\langle \upsilon_{g1}\right\rangle\right\rangle}{\left\langle p\right\rangle}\left(-\frac{d\left\langle p\right\rangle}{dz}\right) -\left(\left\langle \eta_{RC}^{(11,2)}\right\rangle+\left\langle \eta_{WE}^{(11,2)}\right\rangle+\left\langle \eta_{WE}^{(12,2)}\right\rangle-\left\langle \eta_{SO}^{(2,12)}\right\rangle\right)-\left\langle \eta_{\exp 12}\right\rangle \tag{3.13}$$

$$\frac{\partial}{\partial z}\left(\left\langle \alpha_2\right\rangle\left\langle\left\langle \upsilon_{g2}\right\rangle\right\rangle\right)=\frac{\left\langle \alpha_2\right\rangle\left\langle\left\langle \upsilon_{g2}\right\rangle\right\rangle}{\left\langle p\right\rangle}\left(-\frac{d\left\langle p\right\rangle}{dz}\right) +\left(\left\langle \eta_{RC}^{(11,2)}\right\rangle+\left\langle \eta_{WE}^{(11,2)}\right\rangle+\left\langle \eta_{WE}^{(12,2)}\right\rangle-\left\langle \eta_{SO}^{(2,12)}\right\rangle\right)+\left\langle \eta_{\exp 12}\right\rangle \tag{3.14}$$

where η and ϕ are the source/sink terms for the void fraction and IAC. The terms $\phi_{1,\exp}$ and $\phi_{2,\exp}$ denote source terms due to expansion/compression associated with the pressure change at the axial location for each group. The last term of each equation represents the inter-group transfer at the group boundary due to the pressure effect. It should be noted that the pressure effect on inter-group transfer is neglected in Fu's model as well as some follow-up studies [18], [28], [33]. As mentioned previously, the original inter-group expansion/compression formulation double counts the effect of intergroup transfer due to bubble interactions. Revision of the inter-group expansion terms (Eq. (3.7) (3.8)) is adopted in the current study, and the specific expressions are also available in Appendix A.

After applying constitutive models of the source/sink terms, equations (3.11)-(3.14) have 6 unknowns left, $\left\langle \alpha_1\right\rangle, \left\langle \alpha_2\right\rangle, \left\langle a_{i1}\right\rangle, \left\langle a_{i2}\right\rangle, \left\langle\left\langle \upsilon_{g1}\right\rangle\right\rangle$ and $\left\langle\left\langle \upsilon_{g2}\right\rangle\right\rangle$. To close the system, the momentum equations of each group should be included. However, given that the constitutive relations for momentum interfacial transfer such as lift force model and bubble dispersion force model are still under development, solving IATE coupled with momentum equations would mix the errors from the IATE and momentum transfer models. To focus on the interfacial area transport and decouple

the two-fluid model momentum equations, a simplified approach is adopted to solve the one-dimensional two-group IATE. The gas velocity of each group is estimated using the experimental data by interpolating the measured gas velocity at three axial locations. To ensure the accuracy of the velocity measurement, the velocity results were crosschecked with rotameter measurement results ($\langle j_g \rangle / \langle \alpha \rangle$) and the drift-flux model prediction. An explicit Euler method is applied using a finite differencing approach to solve these ordinary differential equations. The flow parameters (void fraction, IAC, etc.) measured at the first port are used as the inlet conditions. The schematic of the numerical solution scheme is shown in Fig. 3-1.

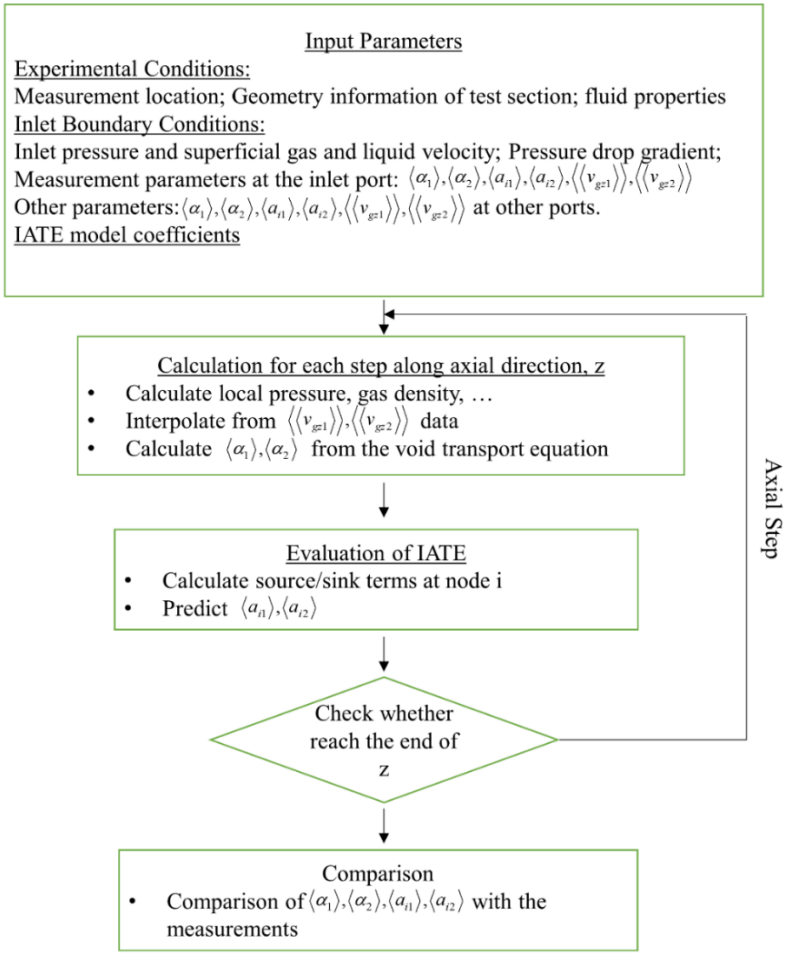

Figure 3-1 Schematic flow diagram of the numerical solution scheme

3.3 IATE Evaluation Results

3.3.1 IATE Evaluation Using Fu-Ishii Model

Fig. 3-2 presents the prediction error of the Fu-Ishii IATE model compared to the experimental data for all 24 flow conditions. The void fraction or IAC error in this plot is defined as

$$error_{\psi} = \sqrt{\frac{\sum_{i=1,2}^{k=2,3} \left(\left(\psi_{i,k,pred} - \psi_{i,k,exp} \right) / \psi_{t,k,exp} \right)^2}{4}} \tag{3.15}$$

where Ψ represents α or a_i, and i = 1, 2 means group I or group II, and t represents the total value of both groups, then k = 2, 3 refer to the results measured at the second (middle) or third (highest) port. It should be mentioned that in the denominator, instead of using $\psi_{i,k,exp}$, the total measured value is used. The reason is that for some one-group to two-group transition flow conditions, the group II void fraction and IAC could be very small. The calculated relative prediction error will be huge if these small values are used in the denominator, which makes this relative error not an ideal parameter to quantify to the prediction accuracy of various flow conditions. In Fig.3-2, each subplot represents flow conditions with the same superficial liquid velocity but different superficial gas velocities. From left to right the superficial increases and approximated void fraction is 0.1, 0.15, 0.2, 0.25, 0.3, 0.35, 0.45, 0.6, respectively. The result indicates that both the IAC and void fraction prediction error increase with the void fraction and reaches the maximum at the void fraction approximates to 0.3. Besides, the prediction errors for lower superficial liquid velocity conditions are larger. The test matrix with IAC prediction error indicated is plotted in Fig. 3-3. The large discrepancy happens near the bubbly to slug transitions boundary line, and the void fraction range for large discrepancy happens increases with the superficial liquid velocity decreasing.

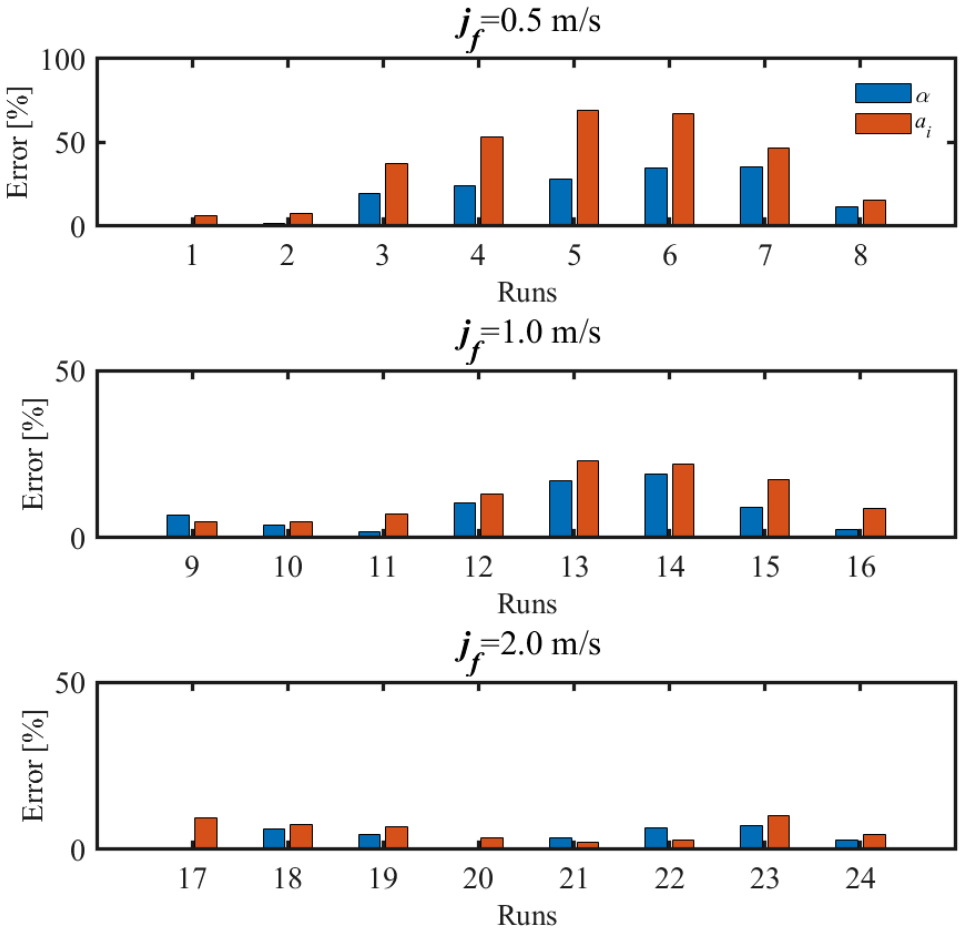

Figure 3-2 IATE prediction errors using Fu-Ishii model for round pipes

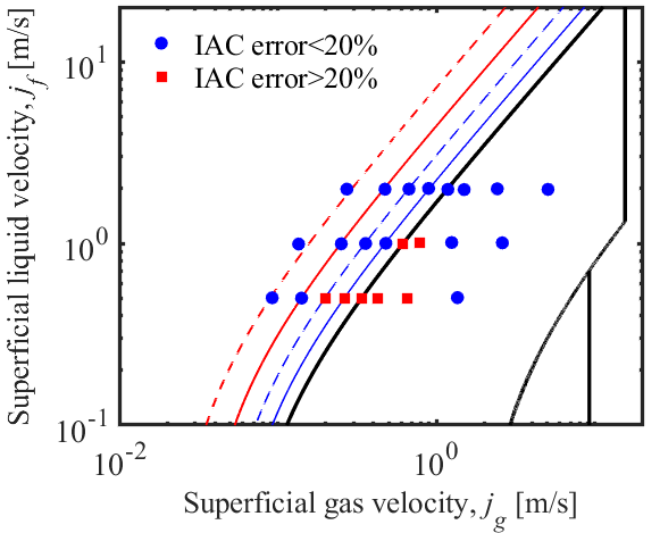

Figure 3-3 Test matrix with the IAC prediction error

The predicted axial development of void fraction and IAC for Runs 5, 13, and 21 are shown in Fig. 3-4. The area-averaged void for these runs is about 0.3. For Runs 5 and 13, the significant decrease of group I void fraction and increasing of group II void fraction is detected along the axial direction. The coalescence of small bubbles results in the decreasing of IAC, which is shown in the measured IAC axial development. However, the IATE model prediction underestimates the drastic inter-group transfer for Runs 5 and 13, and therefore, overestimates the group I void fraction and total IAC. For Run 21, the model works well and both void fraction and IAC are well predicted. It should be noted that for Run 21, the inter-group transfer is not as significant as Runs 5 and 13.

To further investigate the reason for the underestimation of the inter-group transfer, the contribution of various mechanisms (RC, WE, TI, SO, etc.) for Run 5 are plotted in Fig. 3-5. The left column is the predicted IAC development, the middle column is source contributions to group I IAC change, and the right column is source contributions to group II IAC change. It can be observed that the mechanisms related to the inter-group coalescence like $\phi_{WE,k}^{(11,2)}$ and $\phi_{RC,k}^{(11,2)}$ are inactive in the prediction, while these terms are in charge of generating group II bubble from group I bubbles. Besides, the inter-group wake entrainment mechanism $\phi_{WE,k}^{(12,2)}$ which entrains group I bubbles into group II bubbles are also not active. In small and moderate pipe sizes ($D_h<D_{cap,max}$), this mechanism should be dominating for the transition from bubbly flow to well-established slug flow. Therefore, the inter-group coalescence mechanisms of the current model needs to be improved to better predict the interfacial area transport in the bubbly to slug transition flow.

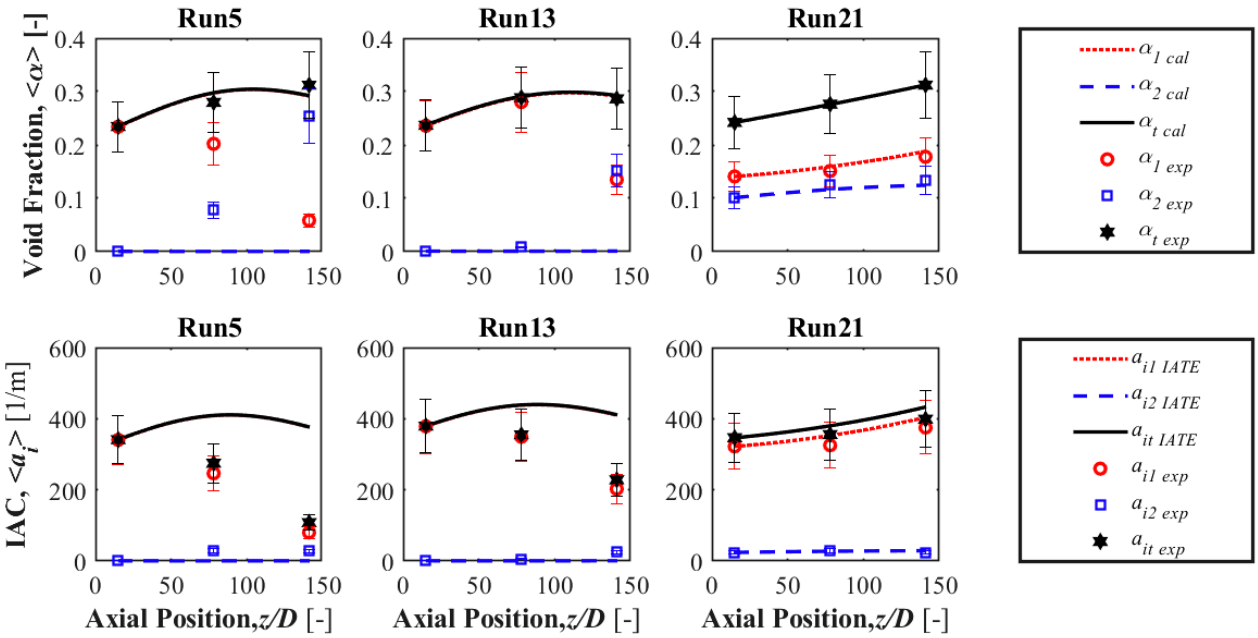

Figure 3-4 IATE prediction of axial development for flow conditions with void fraction of 0.3

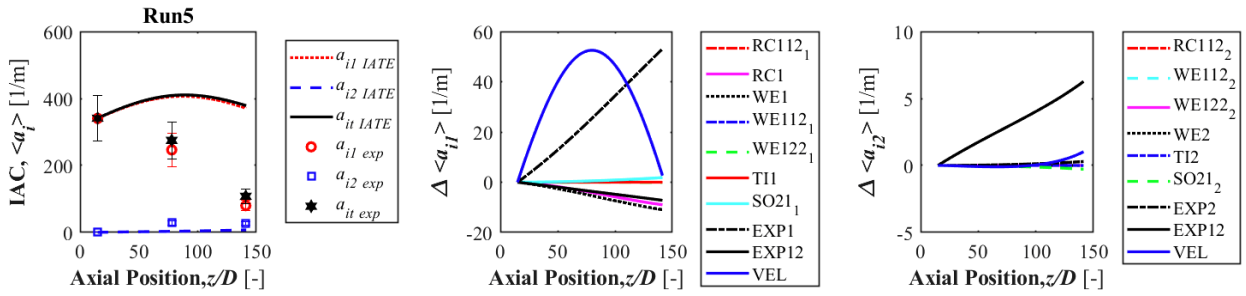

Figure 3-5 Contribution of various mechanisms on IAC change

3.3.2 IATE Evaluation Using Improved Model

As mentioned in 1.2.2, Doup [32] pointed out that the units of terms $\phi_{WE,1}^{(12,2)}$, $\phi_{WE,2}^{(12,2)}$, $\phi_{WE}^{(2)}$, $\eta_{WE}^{(12,2)}$, and κ_{fr} in Fu-Ishii model are inconsistent, and he re-derived these models to address these inconsistency issues and performed experiments on a 50 mm ID round pipe facility. Coefficients related to group II wake entrainment and shearing-off mechanisms were revised based on data. In addition to improvement on model consistency, Worosz [28] proposed a new view to model the inter-group wake entrainment (11,2) to improve the capability of the model in one-group to two-group transition flow. It is suggested to consider the generation of group II bubbles by wake entrainment (11,2) as a developing process, instead of regarding it as the result of the coalescence

of two group I bubbles. Specifically, once a large group I bubbles exist, they will start to coalescence with small bubbles in their wake and grow gradually and eventually become group II bubbles. While in previous binary reaction formulations, a group II bubble is formed by one coalescence of two very large group I bubbles. To quantify the fraction of large group I bubbles that could become group II bubble, a transition function is introduced and implemented into the related source/sink terms. The inconsistent terms were also revised. Worosz's model was evaluated using the one-group to two-group transition data collected in a 50.8 mm ID round pipe, and good agreement was obtained. It should be mentioned that although the data from both Doup and Worosz were collected at the bubbly to slug transition region, there is no drastic inter-group transfer in the axial direction (like Run 5) observed in their flow conditions. Therefore, the drastic inter-group transfer measured in the current facility (25.4 mm ID pipe) could be attributed to the channel geometry effect.

The comparison of the IAC prediction error for these three different models for all 24 flow conditions is shown in Fig. 3-6. There is no significant improvement in IAC prediction using the model by Doup. Worosz's model gives a better prediction for flow conditions near the transition line (Runs 4, 5, 6, 12, 13, and 14) since it is developed for bubbly to slug transition flow, but the error is still more than 20%. The error for high void fraction and high j_f conditions (Runs 8, 15, 16, 21-24) is very large because of the unphysical behavior of the shearing-off terms in the Worosz model. Fig. 3-7 presents the IAC axial development predicted by these three models for Runs 5, 13, and 21. For Runs 5 and 13, the prediction results by the Doup model are almost the same as the prediction by Fu-Ishii model. Although the performance of Worosz's model is better than the others, the inter-group transfer is still underestimated. For Run 21, Worosz's model overestimates the shearing-off effect and gives a higher group I IAC prediction.

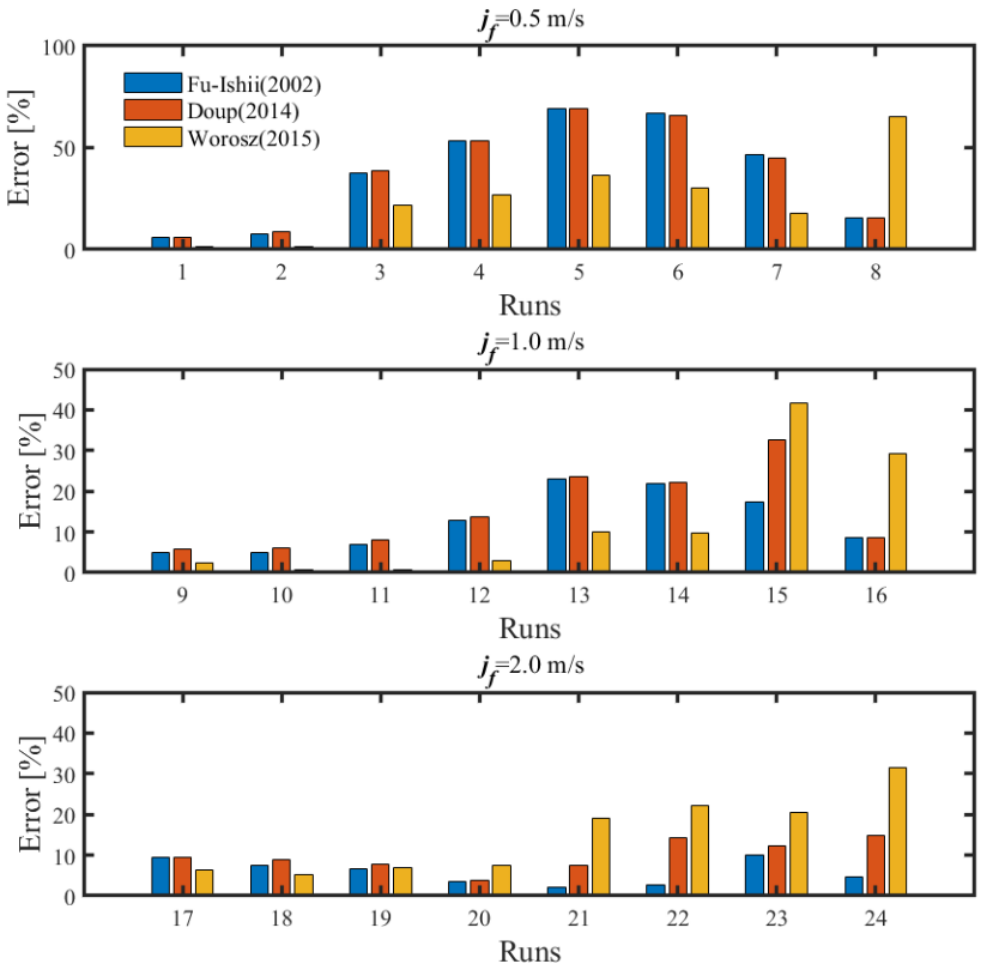

Figure 3-6 Comparison of overall IAC error for different models

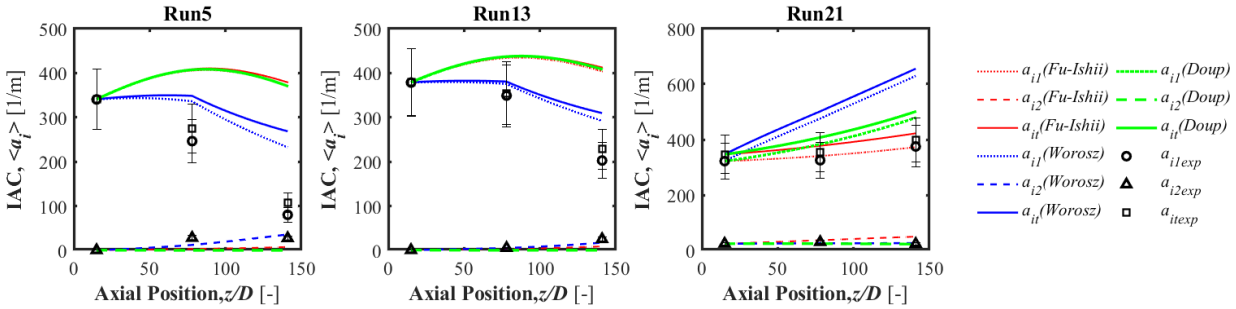

Figure 3-7 Comparison of IAC axial development for different models

3.4 Analysis of Discrepancy at Bubbly to Slug Transitions

As mentioned in section 3.3.2, the responsible mechanisms ($\phi_{WE}^{(11,2)}$, $\phi_{RC}^{(11,2)}$) for generating group II bubbles are not active as they are supposed to be at the transition conditions. To find out the reason, the derivation processes were reviewed, and corresponding assumptions were re-evaluated. One important assumption used in the derivation is the uniform bubble number density distribution within each group, which means the bubble number density for different sizes of bubbles is the same. Then the void fraction, α, and the IAC, a_i, for group I bubble can be formulated as

$$\begin{cases} \alpha_1 = \int_V fVdV = \int_{V_{\min}}^{V_{m1}} fVdV = f_1 \int_{V_{\min}}^{V_{m1}} VdV = f_1 \dfrac{V_{m1}{}^2 - V_{\min}{}^2}{2} \\ a_{i1} = \int_V fA_i dV = \int_{V_{\min}}^{V_{m1}} fA_i dV = f_1 \int_{V_{\min}}^{V_{m1}} A_i dV \end{cases} \tag{3.16}$$

where f means the bubble number density distribution and the bubble number density of specified bubble volume range can be acquired by integrating f within that volume range. V_{min} and V_{m1} are the lower and upper limits of group I bubble volume, respectively, and A_i is the bubble surface area. Given the spherical assumption for group I bubble shape, it is easy to get

$$A_i = (36\pi)^{1/3} V^{2/3} \tag{3.17}$$

and

$$a_{i1} = \frac{3}{5}(36\pi)^{1/3} f_1 \left(V_{m1}^{5/3} - V_{\min}^{5/3}\right) \tag{3.18}$$

Then the Sauter mean diameter of group I bubbles, D_{sm1}, can be expressed as

$$D_{sm1} = \frac{6\alpha_1}{a_{i1}} = \frac{5\left(V_{m1}{}^2 - V_{\min}{}^2\right)}{(36\pi)^{1/3}\left(V_{m1}^{5/3} - V_{\min}^{5/3}\right)} \tag{3.19}$$

and consider that V_{min} is much less than V_{m1},

$$D_{m1} = 1.2 D_{sm1} \tag{3.20}$$

To generate a group II bubble, the maximum group I bubble volume should be at least half of the minimum group II bubble volume.

$$V_{m1} \geq \frac{1}{2} V_c \tag{3.21}$$

From Eq. (3.20) and (3.21) the Sauter mean diameter requirement for generating a group II bubble can be expressed as

$$D_{sm1} \geq \frac{\left(\left(D_c\right)^3/2\right)^{1/3}}{1.2} \tag{3.22}$$

For the current air-water facility operated at room temperature and around the atmosphere pressure, D_c is about 10.9 mm. From Eq. (3.22), the required Sauter mean diameter of group I bubble (D_{sm1}) to activate the group II bubble generation mechanisms ($\phi_{WE}^{(11,2)}$, $\phi_{RC}^{(11,2)}$) should be at least 7.2 mm. However, the experimental results [42], [43] indicate that the group I Sauter mean diameters are usually less than 5 mm, even at the bubbly to slug transition flow conditions. This means the Sauter mean diameter criteria derived from the uniform bubble size distribution may not be able to accurately reflect the physical process of the initial generation of the group II bubble. Previous studies [66]–[70] show that the bubble size distribution for small bubbles usually follows a log-normal distribution.

Apart from the uniform distribution assumption, in the model derivation, some complicated effects like bubble coalescence efficiency are assumed to not change for various flow conditions. Therefore, they are represented by experimental coefficients and determined through benchmark experiments. Even if the constitutive models themselves are derived based on reasonable assumptions, the prediction error could still be high if the experimental coefficients are not well benchmarked. It should be noted that all three models evaluated in the current study are developed based on data collected in moderate pipe sizes ($2D_c \lesssim D_H \lesssim D_{cap,\max}$), and from these data, there is no drastic inter-group transfer observed in bubbly to slug flow transitions conditions. It is easy to comprehend that the bubbly flow to slug flow transition process could depend on the channel size. Fig. 3-8 schematically presents the difference of the bubbly to slug flow transition between small size pipe ($D_H \lesssim 2D_c$), and moderate size pipe ($2D_c \lesssim D_H \lesssim D_{cap,\max}$). In a moderate size pipe, the pure bubbly flow will first change to dispersed cap-bubbly flow and then transit to confined slug flow with the void fraction increasing. But in a small pipe, cap bubbles or even large group I bubbles could be confined by the channel, and the probability of following bubbles located in the wake region of cap bubbles and the large group I bubbles is much higher than that in a moderately pipe size. Therefore, the wake entrainment will be intensified in a small size pipe, and the transition should be more drastic. Given that the channel geometry effect is not considered in the previous models, significant change of the experimental coefficients could be necessary to get

good prediction results on the current data collected in the 25.4 mm ID test section. To fulfill the complete benefits of IATE, unified constitutive models for various pipe sizes including the channel geometry effects should be developed in the future. Developing these unified models will need more detailed transition data in various flow channels with different sizes.

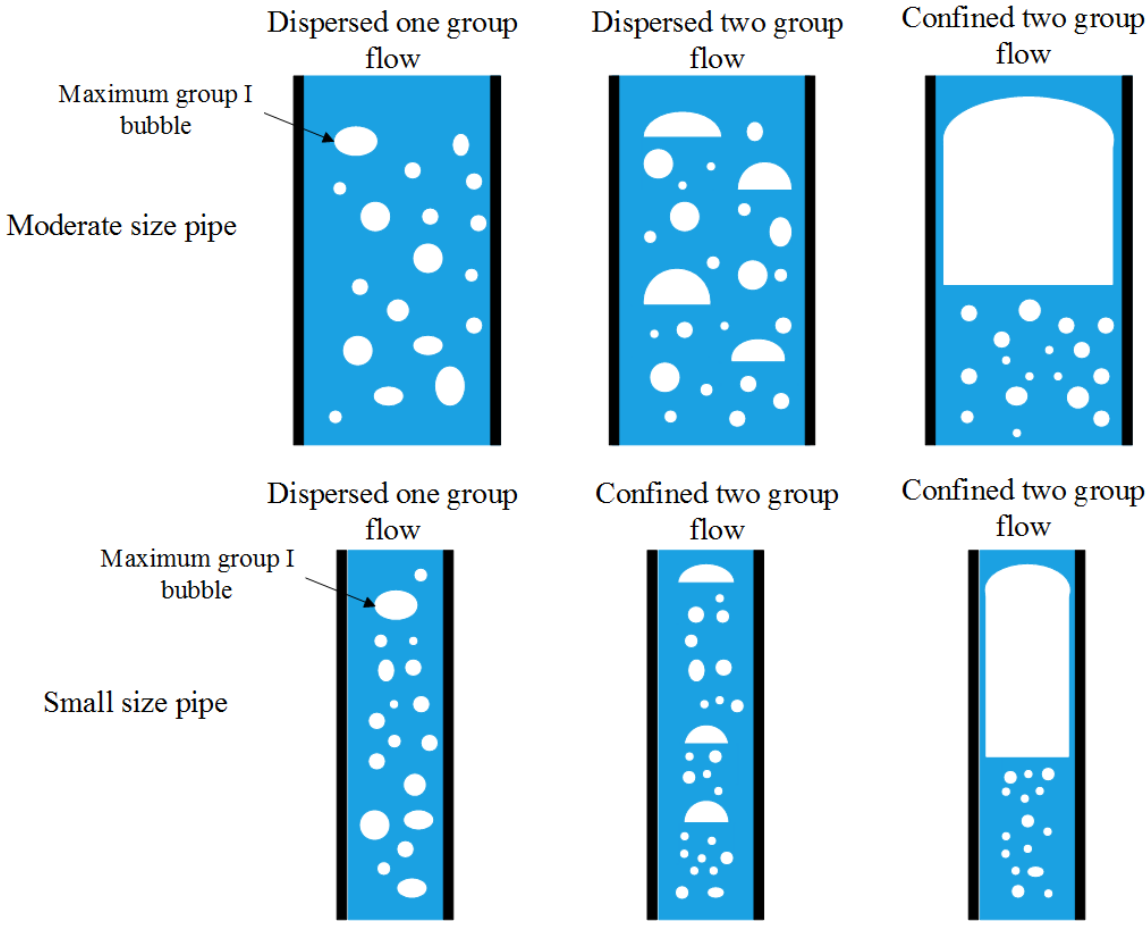

Figure 3-8 Schematic of one group flow to two group flow transition

3.5 IATE Model Improvement for Bubbly to Slug Transition Flow

3.5.1 Model Optimization Approach

To benchmark and optimize the inter-group transfer terms in a more reasonable way, a new approach using inter-group void transport equations to benchmark the inter-group transport is proposed. The schematic of the newly proposed IATE benchmarking approach is shown in Fig. 3-9. First, the gas velocity of each group will be carefully checked to ensure accuracy. To make sure of the accuracy of the velocity measurement, a two-step check process will be performed

before inputting the velocity information into the calculation. First, the velocity measured by the probe will be compared with the velocity converted from the rotameter, and the error can be checked using two independent instruments. The second step is to compare the experimental value with the velocity calculated from the drift-flux model. By doing this two-step check, the velocity error can be estimated and those flow conditions with large errors (>25%) will not be used in the IATE evaluation. Then the inter-group transfer terms will be calibrated using void transport equations and the void fraction measured by experiment. After benchmarking the inter-group void transport terms, the inter-group interfacial area transport terms will also be determined because both void transfer terms and IAC transfer terms are derived from the same particle number interaction mechanisms. Then using the newly calibrated inter-group IAC transport terms in the IATE calculation, compare the calculated IAC with the experimentally measured value. If a large deviation exists, the intragroup terms calibrated previously should also be improved at the group I to group II transition flow.

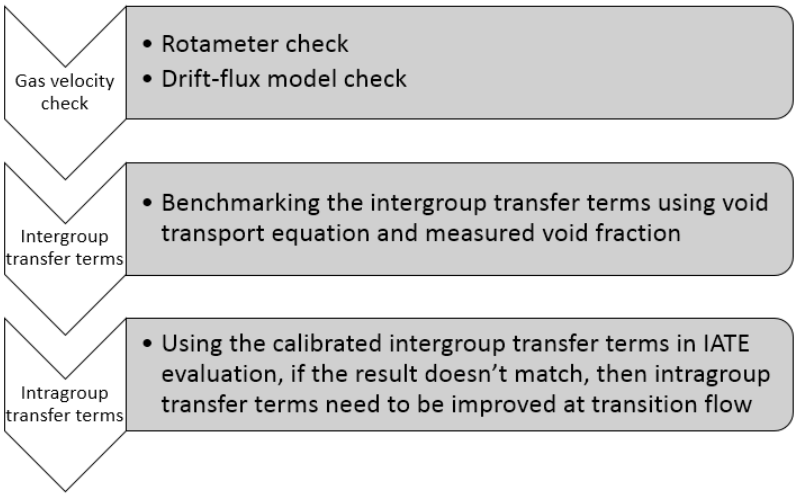

Figure 3-9 Schematic of the new IATE optimization approach

3.5.2 New Model of Group I Intergroup Wake-Entrainment ($WE_{11,2}$)

Before developing a new model, a preliminary parametric study has been performed. It was found that the experimental constant $C_{WE11,2}$ needs to be increased to get a reasonable prediction of the intergroup transfer for transition conditions. Although just increasing the experimental constant can get a better prediction for flow conditions near the transition line, the predictions for other conditions become worse due to the overestimation of group I wake entrainment. Therefore, the

model cannot be fixed by simply adjusting the experimental constant, the mechanistic model should be included to make sure the group I wake entrainment increases at the transition boundary and diminishes after the transition.

Based on the derivation of Sun [19], the group I bubble wake-entrainment reaction rate can be expressed as

$$R_{WE}^{(1)} = 7.05\times10^{-3} C_{WE}^{(1)} C_{D1}{}^{1/3} u_{r1} \frac{a_{i1}{}^{4}}{\alpha_1{}^{2}} \tag{3.23}$$

Similarly, the group I intergroup bubble wake-entrainment rate can be expressed as

$$R_{WE}^{(11,2)} = 7.05\times10^{-3} C_{WE}^{(11,2)} C_{D1}{}^{1/3} u_{r1} \frac{a_{i1}{}^{4}}{\alpha_1{}^{2}} T(D_{sm1}) \tag{3.24}$$

Where $T(D_{sm1})$ is a transition function that describes the ratio of group I intergroup wake-entrainment to the group I total wake entrainment. The group I intergroup wake-entrainment is possible only when a group I bubble is large enough, so it can gather several small bubbles into its wake to become a group II bubble. Currently, the critical size is preliminarly set to be 5.8 mm, since this is a critical size for the change of lift force direction [71] and bubbles larger than this size will go from the near-wall region to the pipe center and form a stable wake region. Then the transition function can be expressed as the ratio of bubbles larger than this critical size to the overall bubble numbers. To calculate the transition function, the group I bubble size is assumed to follow the upper-limit log-normal distribution [72]:

$$f(V) = C\frac{1}{\sqrt{2\pi}\sigma_0}\exp\left[-\frac{1}{2}\left(\frac{\ln(aD)-\ln(D_c-D)}{\sigma_0}\right)^2\right]\frac{1}{D} \tag{3.25}$$

where

$$a = \frac{D_c}{D_{sm1}} - 1 \tag{3.26}$$

and D, D_c, and D_{sm1} is bubble diameter, maximum group I bubble diameter, and group I Sauter mean diameter, respectively. σ_0 is the geometric standard deviation. By analyzing the bubble size distribution of the current experiment results, σ_0 has a range of 0.3-0.5 and can be approximately set as 0.4. C is the normalization factor. Once the D_{sm1} is known, the bubble size distribution can be determined using Eq. (3.25) and the bubble number fraction over the critical size can be obtained. The bubble size distribution obtained using Eq. (3.25) for several Sauter mean diameters

are plotted in Fig. 3-10. When D_{sm1} is 2 mm, almost no group I bubble is larger than 5.8 mm, and the intergroup wake-entrainment is negligible. When D_{sm1} is 4 mm, the upper tail of the distribution is larger than 5.8 mm, and for D_{sm1} is 6 mm, more than half of bubbles are available for intergroup wake-entrainment, therefore, this mechanism becomes dominant.

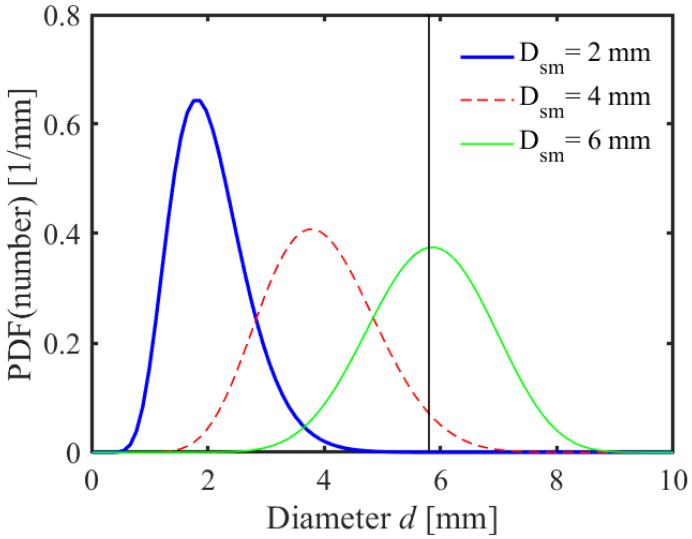

Figure 3-10 Maximum log-normal bubble size distribution

The number fraction of bubbles larger than the critical diameter (D_{change} = 5.8 mm) is plotted against D_{sm1}, as shown in Fig. 3-11. This is also the transition function in Eq. (3.24). It should be mentioned that the experimental constant for intergroup wake-entrainment $C_{WE}^{(11,2)}$ is also different from the intragroup wake-entrainment $C_{WE}^{(1)}$, and is determined based on minimizing the error to be 0.02, compared to $C_{WE}^{(1)}$ of 0.002. This is because that Eq. (3-23) is derived based on binary bubble collision analysis while the intergroup wake entrainment could be a successive reaction consisting of coalescence of several bubbles instead of a binary reaction. As a result, the coalescence rate of any two bubbles during this process could be faster than the estimation given by binary bubble collision analysis.

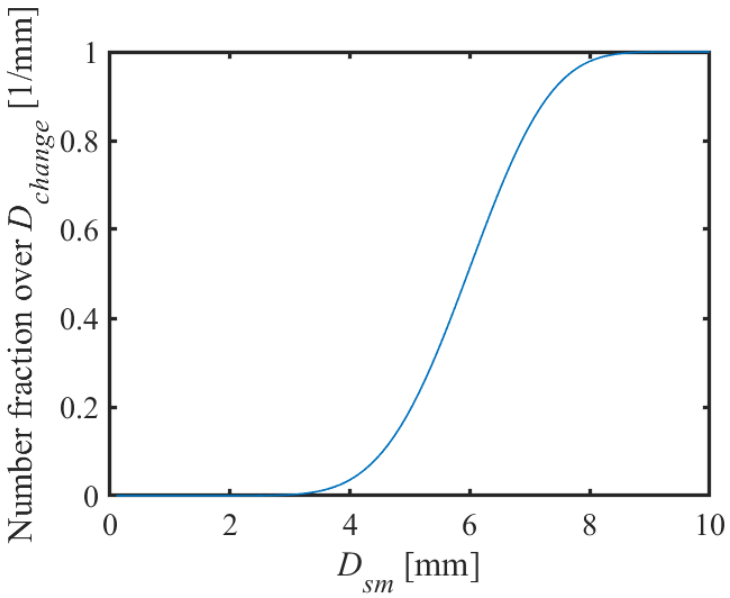

Figure 3-11 Transition function

The IATE prediction for Run 7 using the new group I wake-entrainment model is shown in Fig. 3-12. Although the void fraction prediction and the group I IAC prediction is good, the group II IAC is overestimated. As discussed in 3.5.1, the intergroup terms should be correct since the void fraction is well predicted. Therefore, the problem is the intragroup term, which is the group II wake entrainment for the current case. The intergroup wake-entrainment $WE_{11,2}$ can only generate small cap group II bubbles, which still have a relatively large interface concentration. The change of group II bubbles from the cap bubble to the slug or churn bubble should rely on the group II wake entrainment. In the next section, the group II wake entrainment will be optimized to improve predictions for both void fraction and IAC.

3.5.3 Optimization of Group II Intragroup Wake-Entrainment (WE_2)

Like the group I wake-entrainment, the experimental coefficient $C_{WE}^{(2)}$ will be optimized first to get good results, as the previous coefficients may not apply to the small size pipe data. The optimization is performed by setting $C_{WE}^{(2)}$ as the function inputs and the overall prediction error as the output. Then the Nelder-Mead method [73] is adopted to find the target inputs which is corresponding to the minimum output. The optimized $C_{WE}^{(2)}$ is 0.4, compared to the original value 0.005.

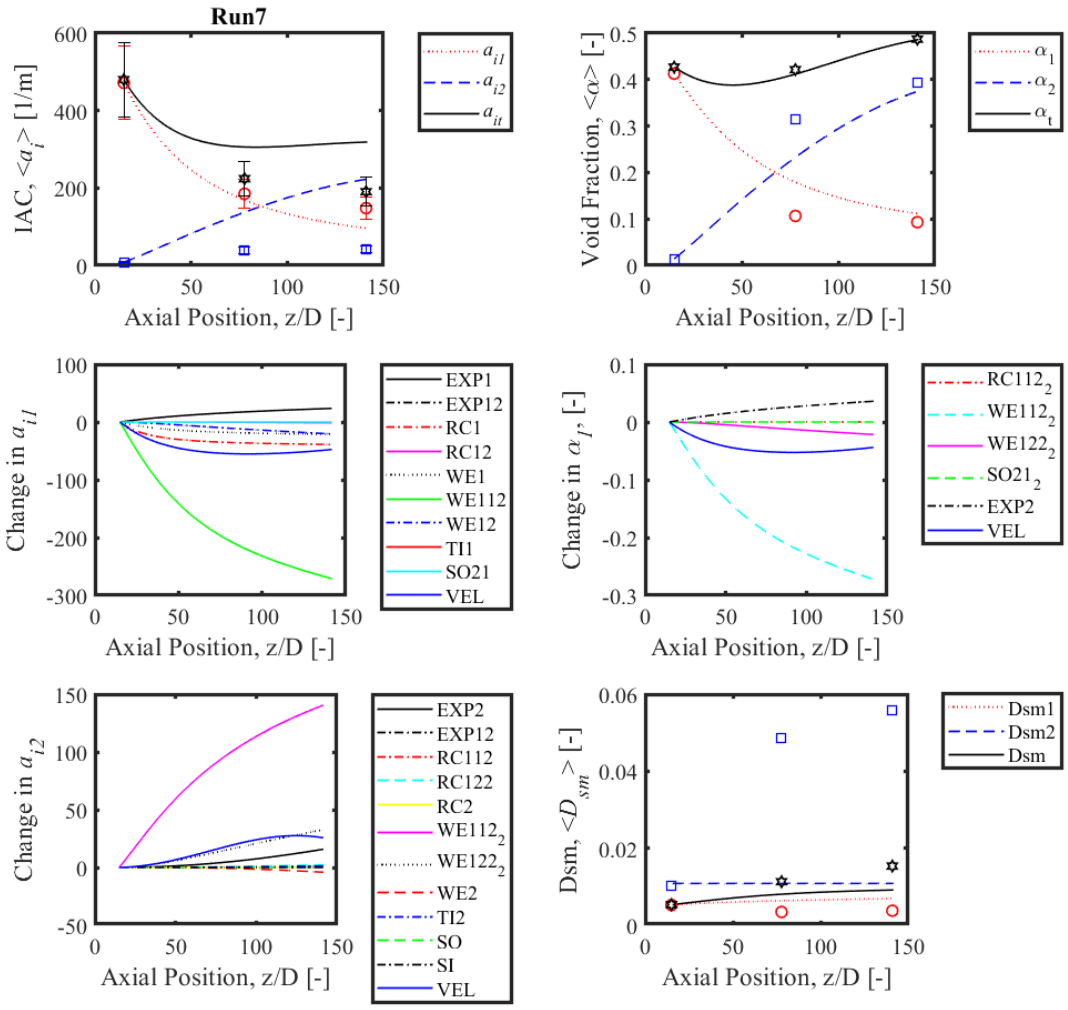

Figure 3-12 IATE prediction details for Run 7 using transition function

3.5.4 Evaluation of the New Model

The IATE prediction of Run 7 using the improved model with optimized $C_{WE}^{(2)}$ is shown in Fig. 3-13. Using the optimized experimental coefficient, both the IAC and void fraction can be well predicted. The bottom left subplot of Fig. 3-13 shows the change of group II IAC for various mechanisms. For group II IAC, initially, it increases due to the group I intergroup wake-entrainment, then the group II intragroup wake entrainment become important and the group II IAC decreases. The prediction results for Runs 5, 13, and 21 are plotted in Fig. 3-14.

The overall prediction error comparison of the new model and the previous models for IAC and the void fraction is presented in Fig. 3-15 and 3-16, respectively. The improved model can predict both the IAC and the void fraction development for all 24 flow conditions with reduced errors.

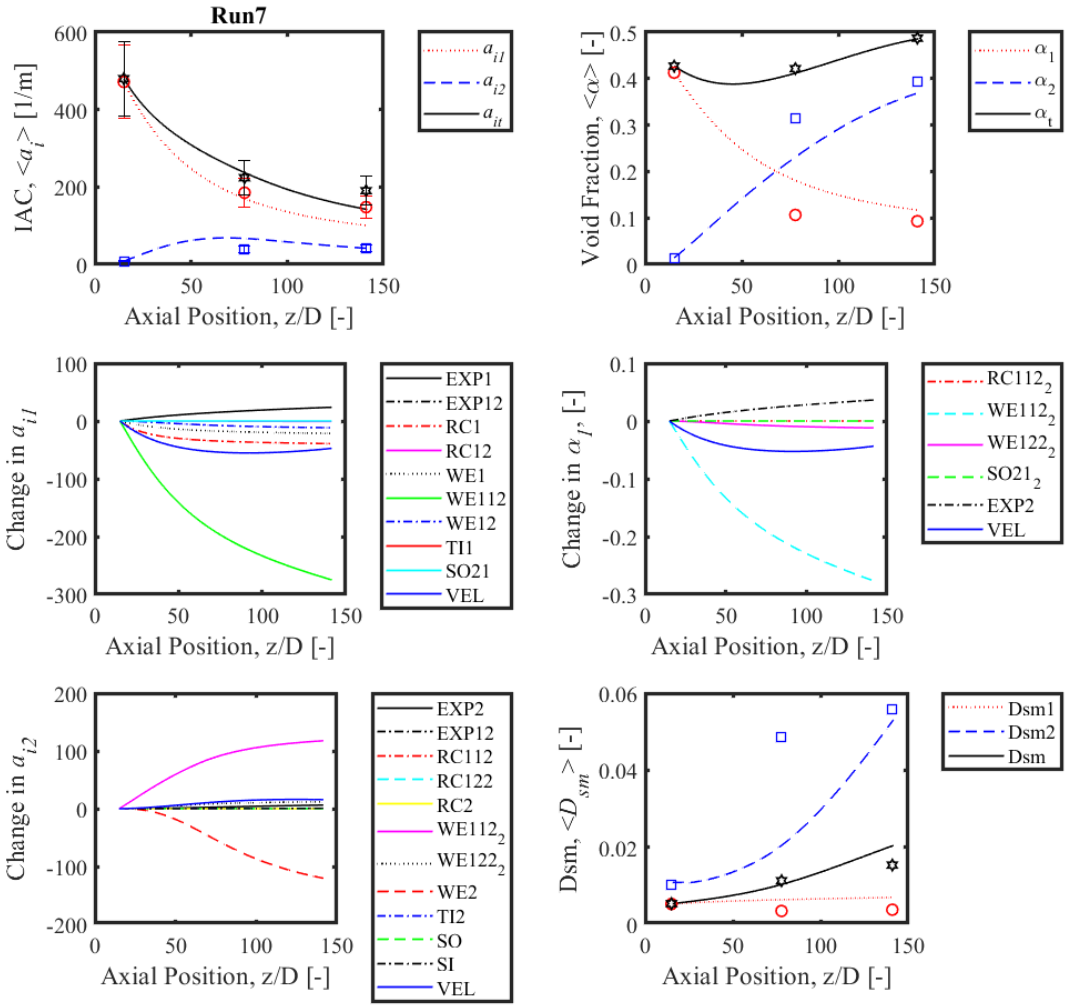

Figure 3-13 IATE prediction details for Run 7 using transition function and optimized $C_{WE}^{(2)}$

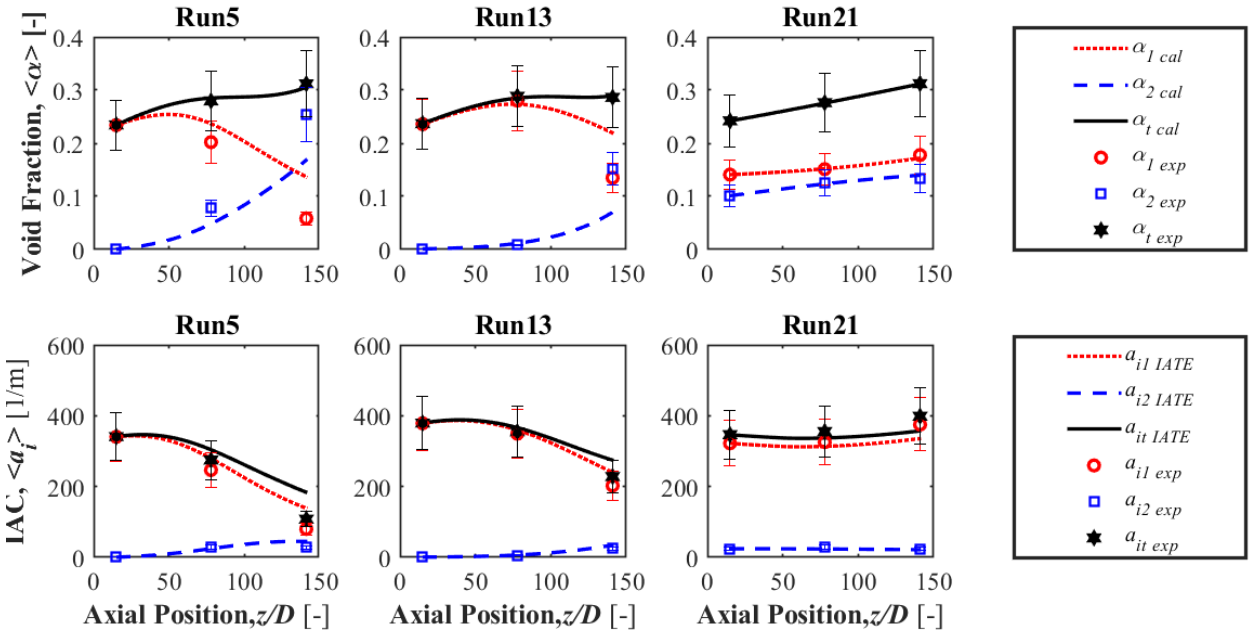

Figure 3-14 IATE prediction using the new model for flow conditions with void fraction of 0.3

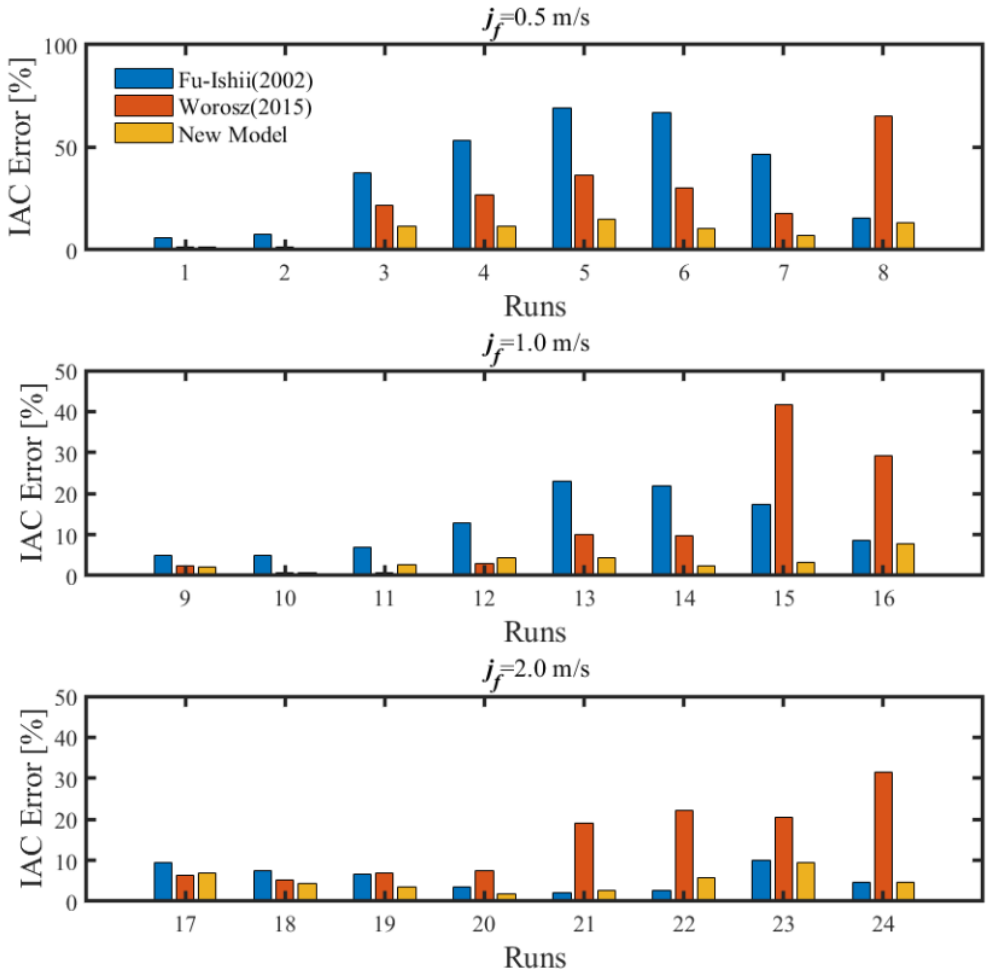

Figure 3-15 IAC error comparison of the new model and previous models

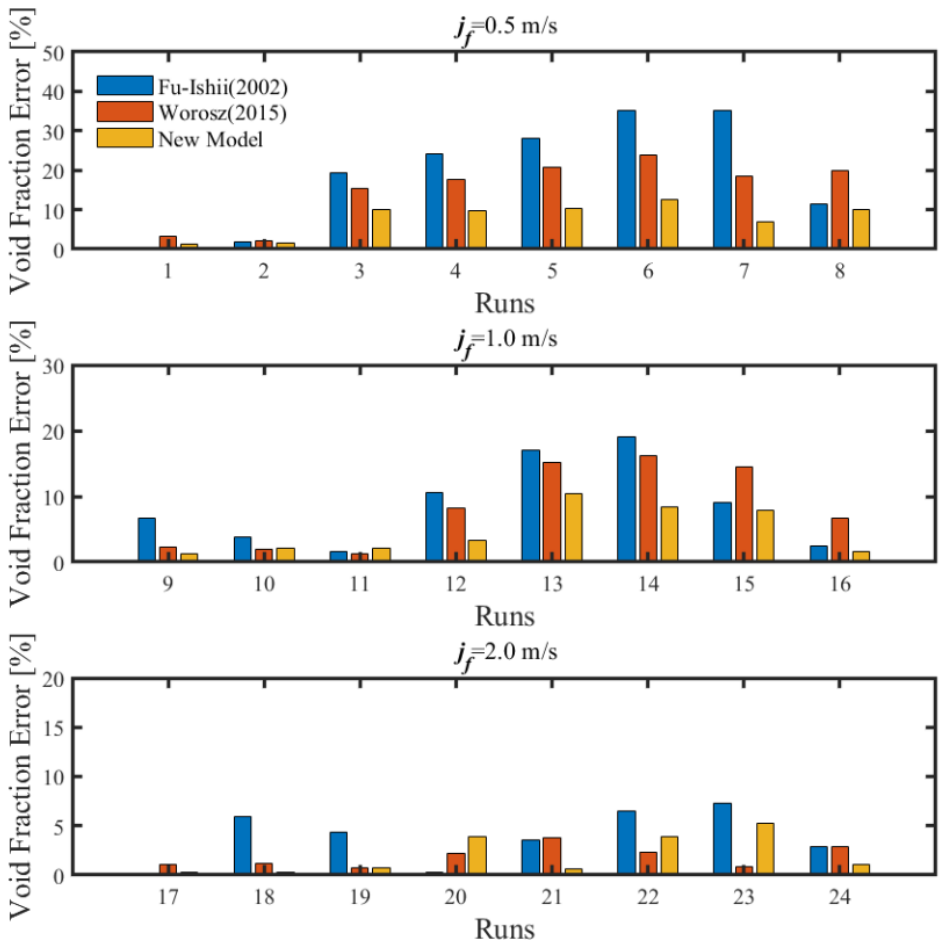

Figure 3-16 Void fraction error comparison of the new model and previous models

3.5.5 Applicability of the New Model on the Moderate Size Pipe

Given that significant change of the experimental constant $C_{WE}^{(2)}$ has been made, it is desirable to check if the new model is still capable to predict the flow in the moderate size pipe. The data collected by Worosz in a 50.8 mm pipe is used to evaluate the newly developed IATE model, and the prediction errors are presented in Fig. 3-17. Comparing to the Worosz model, which developed based on this data, the new model developed for 1-inch has larger prediction error for several runs. But the errors for all flow conditions are still less than 10%, indicating that the new model is applicable to predict the flow in a moderate size pipe. Besides, the prediction details of Run 6 are shown in Fig. 3-18 to illustrate the reason for the error. The prediction error comes from the underestimation of the group I IAC and void fraction, and the data shows an increasing trend of group I void fraction and IAC as the flow developing. Therefore, the error comes from the

underestimation of the shearing-off or turbulence impact mechanisms that can generate group I bubbles along with the flow, instead of previously modified intergroup or intragroup wake-entrainment.

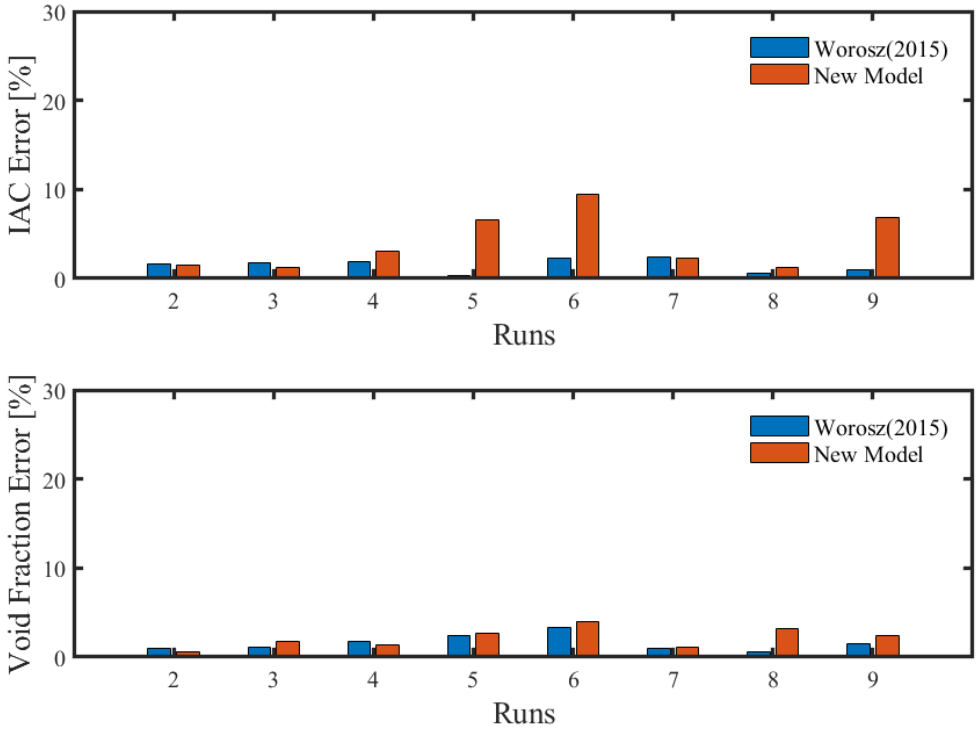

Figure 3-17 IATE prediction error comparison for 2-inch data by Worosz [28]

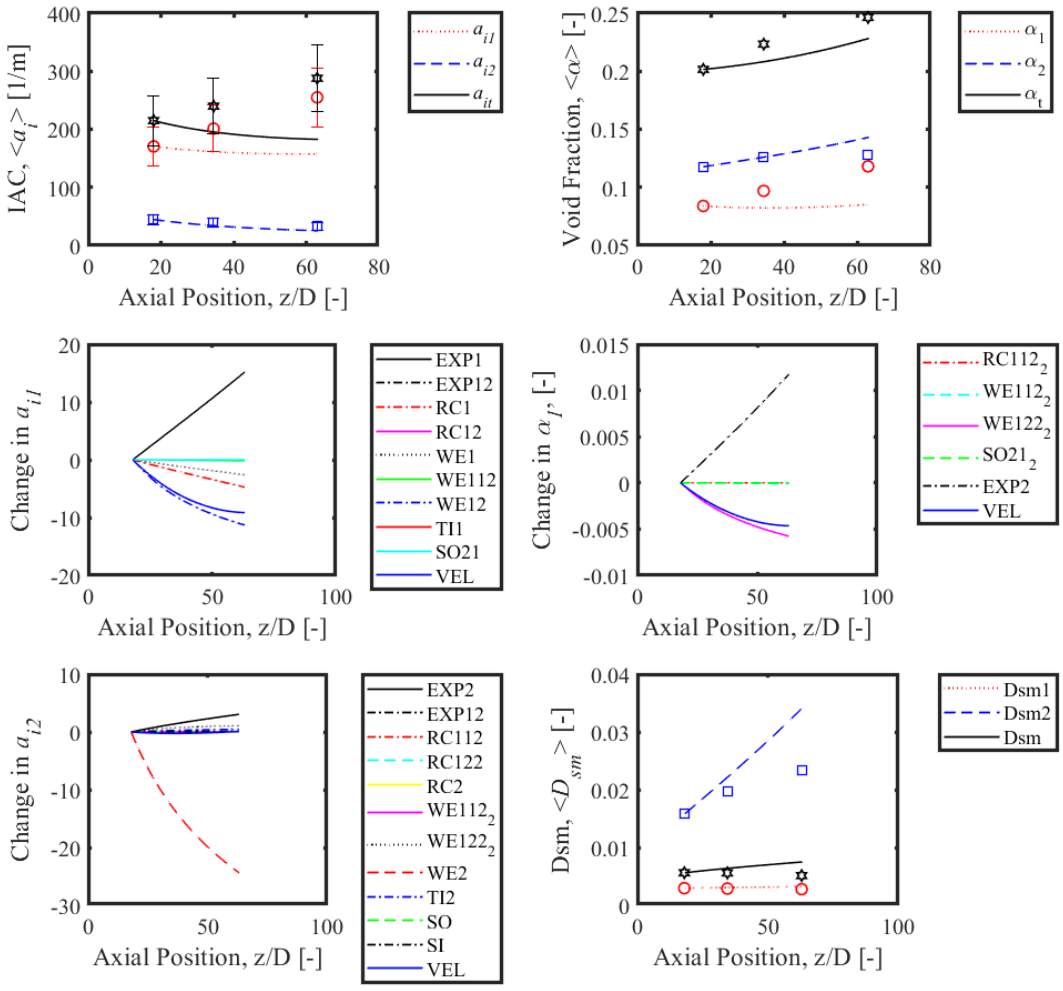

Figure 3-18 IATE new model prediction details for Run 6 of Worosz 50.8 mm pipe data

4. DEVELOPMENT OF THE INSTRUMENTATION FOR CHURN-TURBULENT AND ANNULAR FLOW MEASUREMENT

Currently, few models have been proposed to quantitively describe the flow structure at churn to annular transition flow, because it is very difficult to experimentally capture the flow structure at these regimes. To extend the capability of the conductivity probe to the liquid dispersed two-phase flow (churn-turbulent and annular flow), a new double-sensor Droplet Capable Conductivity Probe (DCCP-2) was proposed by Liu et al [55]. In this design, one more sensor called a 'common sensor' was added to the conventional double-sensor conductivity probe. Using this extra sensor, the dispersed liquid can be detected by measuring the conductance between the common sensor and other sensors. However, the double-sensor probe including the DCCP-2 can only measure the interfacial area concentration of spherical particles like small bubbles and droplets. It is not capable of measuring an irregular interface, which is often encountered in slug, churn-turbulent, and annular flows.

4.1 Four-Sensor Droplet-Capable Conductivity Probe (DCCP-4)

To address this experimental research gap at the churn-turbulent to annular transition and support modeling in these flow regimes, the four-sensor droplet capable conductivity probe (DCCP-4) is developed in this study. By taking advantages of the droplet capable conductivity probe and the conventional four-sensor probe, the DCCP-4 can measure various kinds of interfaces existing in churn-turbulent to annular flow regime transition including droplets and ligaments.

4.1.1 Design of DCCP-4

The schematic of the DCCP-4 is shown in Fig. 4−1. The DCCP-4 consists of four needles which are insulated by a coating except for the needle tip. One uncoated needle, the common sensor, is nestled within the coated needles, adjacent to the leading sensor. For the four coated sensors, one leading sensor is located further forward and three trailing sensors are located about 1 mm behind relative to the flow direction. The radial distance between the leading sensor and the common sensor is about 0.2 mm and the radial distance between the leading sensor and the trailing sensors is around 0.5 mm. As mentioned in the introduction, the conventional four-sensor conductivity

probe circuit uses sensor tips and the probe casing as two electrodes and measures the voltage between them to identify the phase. The probe casing is always connected to the continuous liquid phase as long as the continuous liquid phase exists. If the sensor tip is in a gas phase, a high voltage will be detected, and if the sensor tip is in a continuous liquid phase, a low voltage will be detected. However, if the sensor tip is in a dispersed liquid phase like droplets, a gas phase will be detected. In the DCCP-4 design, the dispersed liquid can be distinguished from the gas phase by measuring the voltage between leading and trailing sensors and the common sensor. The voltage between the common sensor and the probe casing is measured to determine whether the probe is in continuous liquid or continuous gas. The DCCP-4 signal types are summarized in Table 4-1. In addition to the probe design, the circuit of the DCCP-4 is improved to reduce the response time and minimize the cross-channel interference and noise.

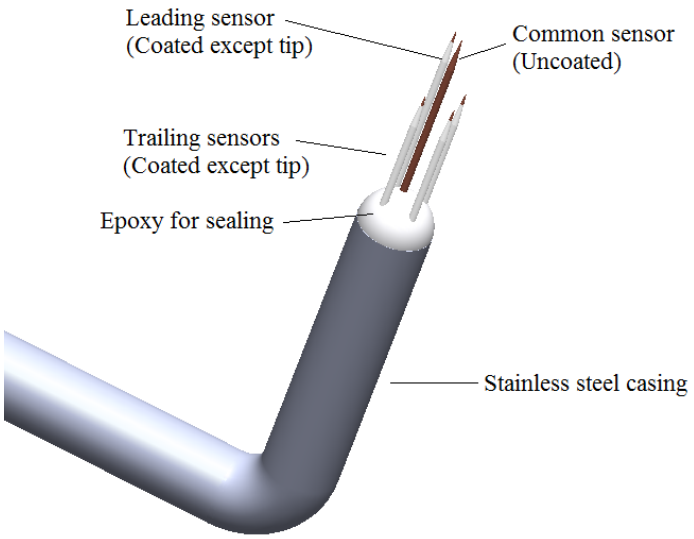

Figure 4-1. Schematic of the DCCP-4 design

Table 4-1. Signal types of the DCCP-4 Signal

Common-Casing Voltage	Common-Leading/Trailing Voltage	Signal Type
Low	Low	Continuous liquid (ligaments/liquid film)
Low	High	Dispersed gas (bubble)
High	Low	Dispersed liquid (droplet)
High	High	Continuous gas (gas core)

4.1.2 Signal Processing Algorithm

The measured voltage signals need to be processed before calculation of two-phase flow parameters. The procedure can be divided into the following steps: signal filtering, normalization, squaring, and pairing. Signal filtering uses the moving median filter technique to eliminate high-frequency noise, which can make the signal smoother without losing physical information. Signal normalization is a procedure that converts the original range of voltage signals to a non-dimensional range between zero and one. Given the actual output voltage value could be affected by factors like the liquid conductivity, cable length, and circuit resistance, normalizing the raw signal is important to standardize the following processing steps. Signal squaring converts the continuous signal to the equivalent indicator function indicating phase. Pairing groups of the squared signals determines interfacial structure information. These last two steps will be described in greater detail below.

After normalization, the signal needs to be converted to a square signal to calculate two-phase flow parameters. The reason is that there is a finite response time when the sensor pierces through the interface, which results from the charge-discharge process of the capacitance and inductance in the probe circuit. To better represent the flow characteristics from the signal, the squaring procedure identifies the start and end points of a sensor passing through a particle. The DCCP-4 data processing software uses signal magnitude and gradient as the criteria to identify the starting and ending points of the interface interaction.

Two typical measurement DCCP-4 signals for a droplet and ligament are plotted in Fig. 4-2 (a) and (b), respectively. Each figure consists of two subfigures. The upper part is the normalized raw signal, and the lower part is a corresponding square signal. The legend 'C-G' means the voltage difference between the common sensor and the probe casing, which is connected to the ground, the 'L-C' represents the voltage difference between the leading sensor and the common sensor, and 'T1/T2/T3-C' are the trailing sensors to common sensor voltage differences. From Fig. 4-2 (a), when the leading/trailing signals decrease, the C-G signal is still high, which means this liquid particle is not connected to the continuous liquid phase and can be identified as a droplet. By comparing the square signal and the normalized signal in Fig. 4-2 (a), it can be verified that the signal processing software correctly identified the starting and ending points when the sensor pierces a droplet. A typical ligaments signal is presented in Fig. 4-2 (b). The C-G signal decreases correspondingly with the other signals, implying the detected liquid phase is connected to the continuous liquid phase, therefore they are classified as ligaments. The ligament signals are much more complicated than the droplet signals. This is because of the complexity of the ligament interfacial structure. The shape of ligaments are irregular and unstable, and usually contain bubbles.

After the signal squaring, the volume fraction of each phase can be calculated based on the square signal of a single channel. The velocity information is not available until the pairing process has been finished. The signal paring finds the particle signals detected by all four channels (L/T1/T2/T3-C) and matches them to represent a particle. The velocity information can be calculated using the time lag of different channels and the probe geometry information; then, the interfacial area concentration can be calculated. The principle of using the 4-sensor probe to detect the interfacial area concentration of an irregular interface was developed by Kataoka and Ishii [74].

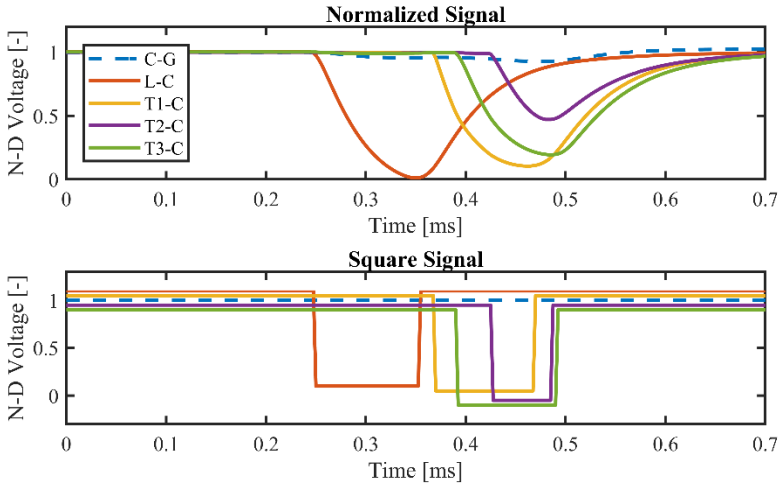

(a)

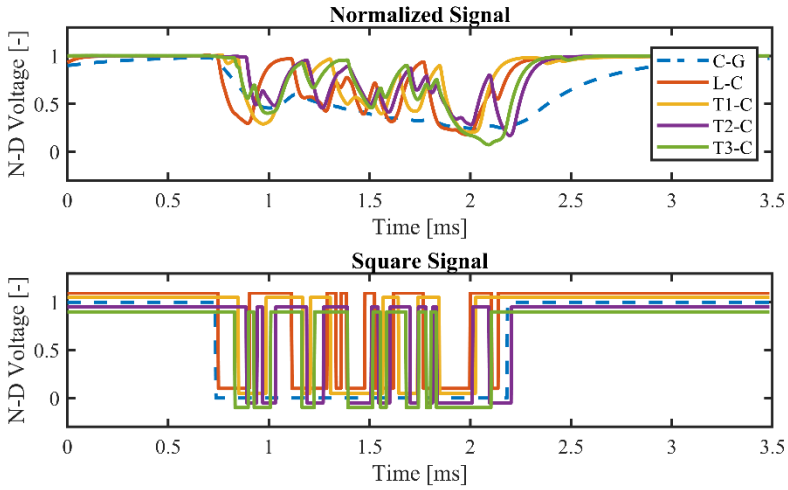

(b)

Figure 4-2. Typical droplet signal (a) and ligaments signal (b) measured by the DCCP-4 for j_f=0.99 m/s j_{g0}=9.38 m/s

4.2 Film Thickness Conductance Probe

Apart from the DCCP-4, conductance film thickness probes are also used to measure the film thickness and the wave velocity in wispy annular flow. Since the conductance between two electrodes of the probe is related to the film thickness, the film thickness can be obtained by measuring the probe conductance and using a calibration curve to convert the measured conductance to the film thickness.

In this study, two types of conductance film probe are used: a flush-mounted and parallel-wire probes, as shown in Fig. 4-3. The flush-mounted probe consists of two stainless steel electrodes with a diameter of 1.49 mm flush-mounted on the measurement surface, and the distance between the two electrodes is 3.5 mm. Given the non-intrusive nature of this kind of design, it has been widely used to measure the film thickness in the annular flow [75]–[77]. The shortcoming of the flushed mounted design is that it saturates for thick films, therefore it can only be used to measure a thin film. The parallel-wire probe design is a usual option for measuring the thick films [78]–[82], which uses two electrodes mounted vertical to the measurement surface and parallel to each other. Stainless steel needles with a diameter of 0.35 mm are selected as electrodes, and the separation between two electrodes is also 3.5 mm. Because of the special geometry of the flow channel (200 mm × 10 mm rectangular), the film thickness at the wide side is expected to be thinner than the film on the narrow side. Therefore, two types of parallel-wire probes with different intrusive lengths are employed. For the parallel-wire probe on the wide side, the intrusive length is 5 mm, while for the probe in the narrow side, the intrusive length is 10 mm.

The design graphs of the film thickness probe ports on the wide side and the narrow side are presented in Figs. 4-4 and 4-5, respectively. The wide side port includes two rows of probes and each row consists of three flush-mounted probes and three parallel-wire probes. The distance between these two rows of film probes is 25.4 mm. The wave velocity can be estimated using the cross-correlation analysis of the film thickness signals at each row. The narrow side port consists of three 10 mm parallel-wire probe. The flush-mounted probe is not used in the narrow side port because the film at the narrow side is expected to be thicker than the maximum measurement limit of the flush-mounted probe.

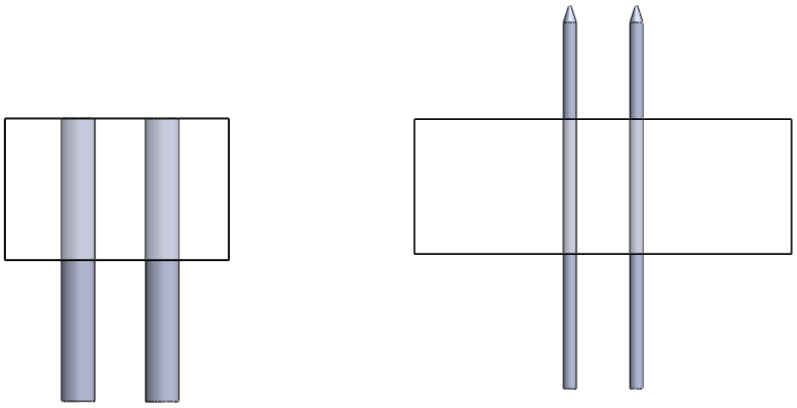

Figure 4-3 Schematic of flush-mounted probe (left) and parallel-wire probe (right)

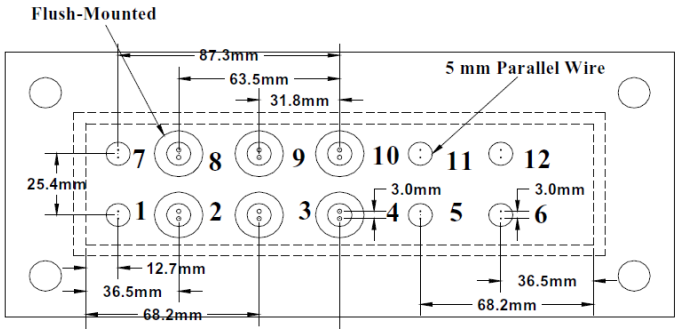

Figure 4-4 Film thickness probe port on the wide side

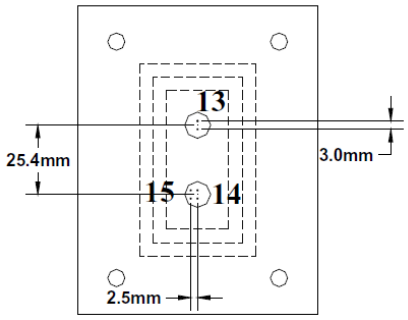

Figure 4-5 Film thickness probe port on the narrow side

The calibration of the film thickness probe is performed in a specifically designed rig. The probe port can be inserted into the calibration setup and forms a cuboid pool where the surface with probes serves as the bottom. By injecting different volumes of water into the pool, films with

various thicknesses can be formed in the pool and their thickness can be calculated using the volume divided by the bottom area. This method is used for the calibration of the parallel-wire probe. For the flush-mounted probe, since its measurement range is usually less than 1 mm, it cannot be calibrated by just injecting the water. The water film will break up due to the surface tension when the film is too thin. An acrylic block with a micrometer is used to form the desired film in the pool filled with water for calibrating the flush-mounted probe. When the acrylic block is touching the probe surface, the film thickness is zero. By moving up the acrylic block with a known distance, a known thickness film can be formed at the measurement surface. The sample calibration results are shown in Fig. 4-6. The measured voltage is nondimensionalized using the voltage measured at no film and very thick film conditions. For the flush-mounted probe (a), The measured non-dimensional voltage saturates when the liquid film is thicker than 2 mm. The slope of the calibration curve starts increasing when the liquid film reaches 1 mm. Therefore, the uncertainty of the flush-mounted probe measuring film thicker than 1 mm is larger than measuring film thinner than 1 mm. For the parallel-wire probe (b, c), the linearity between the film thickness and the non-dimensional voltage is well reflected by the data, and both get saturated when the film is thicker than their intrusive length.

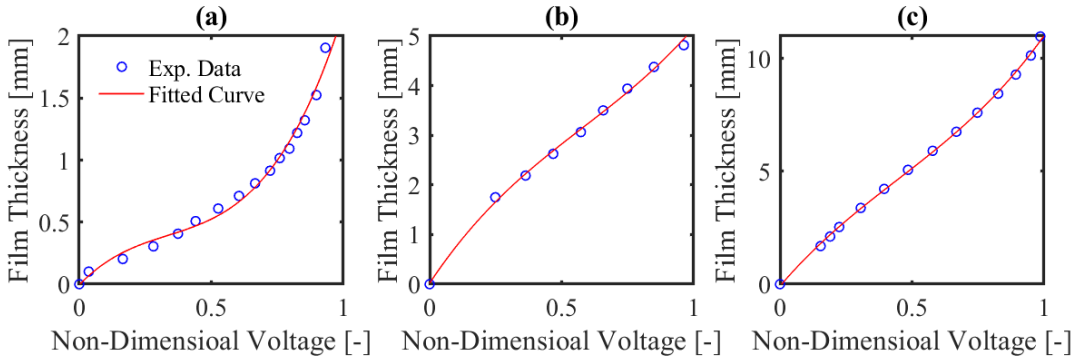

Figure 4-6 Calibration results for the flush-mounted film probe (a) and the parallel-wire probe with intrusive length of 5 mm (b) and 10 mm (c)

5. CHURN-TURBULENT AND ANNULAR FLOW EXPERIMENTS

5.1 Experimental Setup

The experiments are performed in a 200×10 mm narrow rectangular test facility, which has been introduced in detail in section 3.2 The facility is built for the upward air-water two-phase flow experiments, as shown in Fig. 5-1. The main components include air/water supply systems, the two-phase mixing section, the test section, the upper plenum, and the instrumentation system. The 200 mm×10 mm rectangular test section is made of acrylic for the favor of flow visualization. The total height is 3 m. The water is supplied by a centrifugal pump and the water flow rate is measured by a vortex flowmeter with ±2% error of full scale. The air is supplied by an air compressor through a compressed air tank and the airflow rate is measured by several rotameters with an accuracy of ±2% of full-scale reading.

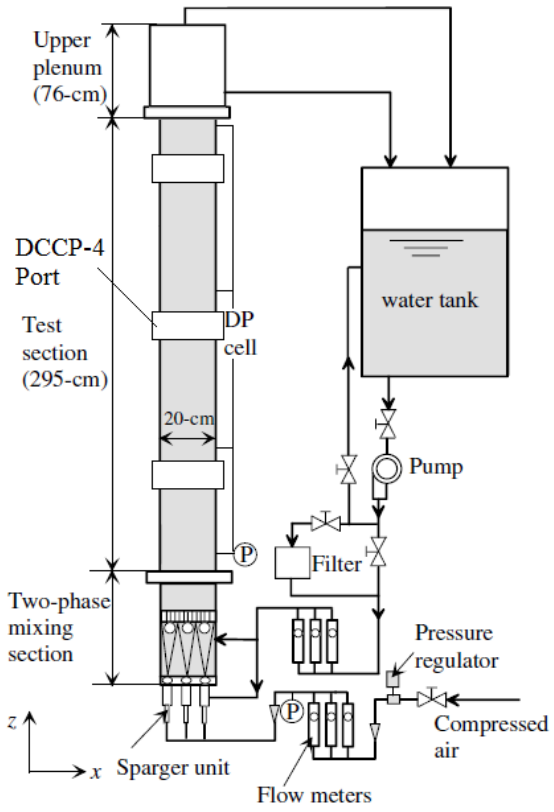

Figure 5-1 Schematic of the experimental facility

In this study, the DCCP-4 local measurements were performed at seven flow conditions, which is plotted in the rectangular channel flow regime map and compared with the previous four-sensor probe data (Fig. 5-2) collected in a narrow rectangular channel [29] [61]. In the previous database, the maximum superficial gas velocity is only 2 m/s. This is mainly limited by the sampling frequency and the signal quality. The sampling frequency of previous data is less than 50 kHz, which would introduce significant uncertainty when measuring the very high gas velocity. Besides, as the gas flow increases, the flow structure will be more chaotic, which requires the signal to have a fast response and minimum interference to reflect the flow physics. The previous probe circuit design could not be applied to the very high gas flow conditions. To address these difficulties, a high sampling frequency (400-600 kHz) is used, and the probe circuit design is optimized to improve the signal quality. The detailed inlet condition of these experimental conditions as well as the pressure measurement results are shown in Table 5-1. Among these seven flow conditions, the first three flow conditions are performed at a superficial liquid velocity about 1 m/s and superficial gas velocity ranges from 9.38 m/s to 19.91 m/s. The goal of these 3 conditions is to investigate the flow structure for the churn-turbulent to annular transition, and the results will be discussed in section 6.2. The remaining four flow conditions are performed at higher superficial gas and liquid velocities, which is in the wispy-annular flow, and the target is to study the flow structure in wispy-annular flow.

Some details of the experiment for the churn-turbulent to annular transition conditions (Runs 1-3) and the wispy-annular flow conditions (Runs 4-7) are slightly different. For the churn-turbulent to annular transition experiment, the DCCP-4 measurement port is installed at z/D_h= 81.6, and 30 cross-sectional locations are measured at each port, with X range from 3 mm to 100 mm and Y range from 2 mm to 5 mm. The sampling frequency is 400 kHz. For the wispy-annular flow experiment, the DCCP-4 measurement port is installed at z/D_h= 132.3. Both the DCCP-4 and the conductance film thickness probe are used to measure the flow structure. 36 cross-sectional locations are selected for the DCCP-4 measurement, as shown in Fig. 2-14. The sampling frequency is 600 kHz, because of the higher superficial gas and liquid velocities.

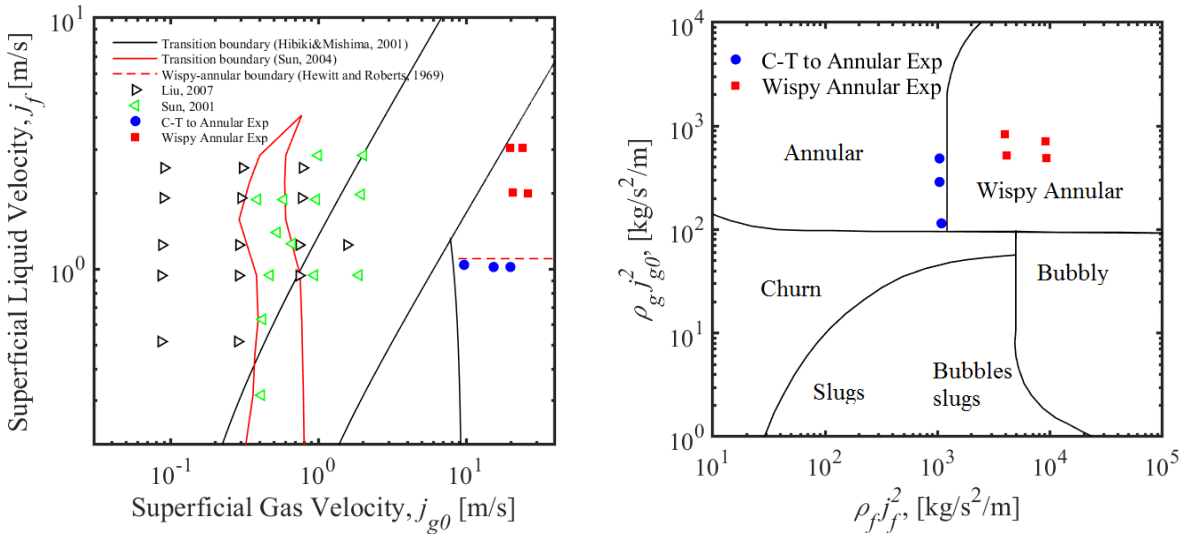

Figure 5-2 Test matrix plotted in flow regime maps by Hibiki and Mishima (left) [65] and Hewitt and Roberts (right) [83]

Table 5-1. Inlet conditions and pressure measurement results

Run#	Inlet Conditions		Pressure (kPa)		
	j_f (m/s)	j_g (m/s)	z/D_h=30.9	z/D_h=81.6	z/D_h=132.3
1	0.99	9.38	125.07	115.14	105.29
2	1.02	15.34	135.53	121.77	107.00
3	1.02	19.91	141.42	125.69	108.30
4	3.03	24.00	235.24	193.94	130.17
5	2.00	26.21	196.67	161.66	118.18
6	3.05	19.95	220.05	182.30	126.69
7	2.03	20.61	183.44	153.62	115.74

5.2 Churn-turbulent to Annular Transition Flow Experiment

5.2.1 Results Verification

Before analyzing the local measurement results, it is desired to check the reliability of the DCCP-4 on measuring churn-turbulent and annular flow. Although the capability of DCCP on measuring droplets has been verified on a facility that can artificially generate liquid droplets [55], the DCCP-4 has not been tested in the actual conditions (churn-turbulent and annular flow). The major difficulty of directly verifying the DCCP-4 results is that few reliable instruments can distinguish the droplet and ligament and measure their fraction/velocity in the churn-turbulent and annular

flow. Instead of direct comparison, several ways to verify the reliability of the DCCP-4 measurement results are discussed in the following sections.

5.2.1.1 Comparison with the conventional 4-sensor probe data

The four-sensor conductivity probe has been used to in a wide range of flow conditions including bubbly, slug, and churn-turbulent flow [18], [29], [54], and the accuracy and reliability for measuring irregular-shaped interfaces has been verified. To confirm that the probe and the circuit design of the DCCP-4 preserve the capability of measuring irregular interfaces, one previous air-water experiment employing the conventional four-sensor probe in churn-turbulent flow condition by Sun [84] are repeated using the DCCP-4, and the result comparison is shown in Fig. 5-3. The inlet superficial liquid and gas velocity is 1.0 m/s and 2.0 m/s, respectively. The conventional four-sensor probe data is represented by a blue circle and the DCCP-4 data is shown as a red square, the error bar is ±10%. The group I bubble refers to the bubbles whose size is smaller than the maximum distorted bubble diameter [27]. Group II signifies bubbles larger than this diameter. Both these two experiments are performed in a 200 mm × 10 mm test section, and Fig. 5-3 presents the data measured in the centerline of the narrow side (Y=5 mm). From the comparison, both the IAC and the void fraction distributions along the wide side (X) measured by the conventional four-sensor probe and the DCCP-4 are close to each other, which supports that the DCCP-4 preserves the capability of the conventional four-sensor probe. It should be mentioned that the void fraction measured by the DCCP-4 is higher than that of the conventional probe, and the deviation is more than the usual probe uncertainty (±10%). There are some reasons for this phenomenon. First, the casing size as well as the sensor geometry of the DCCP-4 are smaller than the conventional probe, which allows the DCCP-4 to detect some smaller bubbles, which are not detectable by the conventional probe. Second, the probe traversing method in previous experiment is different from the current method. In Sun's experiment, the probe traverse from the narrow side of the test section, which will result in a large intrusive length up to 100 mm by the probe casing and may affect the flow symmetry. In the current experiment, the probe traverses from the wide side and the maximum intrusive length is only 5 mm. The different intrusive effect could be responsible for the deviation in the void fraction profile. Given these variations in the probe geometry and the experiment setup, the deviations of the void fraction and IAC profiles are within the experimental

uncertainty and the DCCP-4 is as capable to measure an irregular interface as the conventional four-sensor probe.

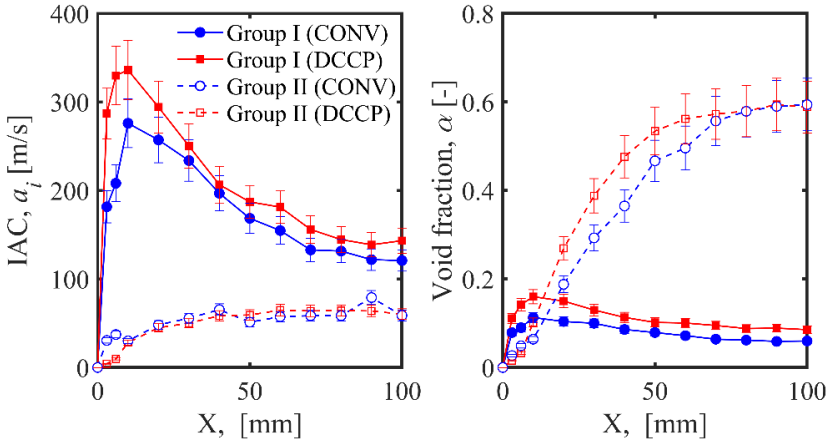

Figure 5-3 Comparison of DCCP-4 data with the four-sensor conductivity probe data [84]

5.2.1.2 Cross-check with area-averaging instrumentation

Since the DCCP-4 can measure the volume fraction and the velocity distribution in a cross-section for the liquid droplets and ligaments, the area-averaged superficial liquid velocity can be estimated using the following equations

$$\left\langle j_f \right\rangle_{lig} = \left\langle \alpha_{lig} v_{lig} \right\rangle \tag{5.1}$$

$$\left\langle j_f \right\rangle_{drop} = \left\langle \alpha_{drop} v_{drop} \right\rangle \tag{5.2}$$

$$\left\langle j_f \right\rangle = \left\langle j_f \right\rangle_{lig} + \left\langle j_f \right\rangle_{drop} \tag{5.3}$$

where j_f, α, and v represents superficial liquid velocity, volume fraction, and velocity, respectively, the subscripts '*drop*' and '*lig*' means it is a droplet or liquid ligament parameter, the pointy brackets are the area-averaging operator. The liquid ligaments mentioned in this paper refers to the liquid phase that is connected to the liquid film on the wall, so it could be the liquid film itself or its wave. It should be mentioned that the above equations may not give an accurate estimation of superficial liquid velocity. This is because the probe can only measure the interface velocity and cannot measure the velocity of the continuous phase without any interface. If there is a significant velocity difference between the continuous liquid (i.e. base film) and the ligament interface, using the ligament interface velocity to represent all the continuous liquid phase could introduce a deviation.

The comparison between the estimated superficial liquid velocity using Eq. (5.1) - (5.3) and the superficial liquid velocity measured by the vortex flowmeter are shown in Fig. 5-4, and the error bar is ±20%. The legend 'j_f-inlet' represents the superficial liquid velocity measured by the flow meter at the inlet and it is assumed to be a constant along the test section due to the incompressibility of the liquid. Runs 1-3 have very close superficial liquid velocities but increasing inlet superficial gas velocities from 9.38 m/s to 19.91 m/s. For all three conditions, the superficial liquid velocity measured by the DCCP-4 is close to the flow meter measurement, which supports the reliability of the DCCP-4. As the superficial gas velocity increasing, more liquid should be entrained from the continuous liquid to the gas core and becomes droplets, which results in the increase of j_f from droplets and decreasing j_f from ligaments. This trend is also reflected in the DCCP-4 measurement.

Apart from the superficial liquid velocity, the superficial gas velocity can also be estimated using the DCCP-4 local measurement results and compare with the converted rotameter reading. Although the continuous gas phase velocity cannot be detected by the probe, it can be approximately estimated using the droplet velocity distribution. The superficial gas velocity calculated using the distributions of void fraction and droplet velocity is compared with the rotameter measurement in the right part of Fig. 5-4. For all conditions the j_g measured by these two different methods are very close, the error is about 10%. It is also noticed that the j_g by the DCCP-4 is always lower than j_g measured by the rotameter. This is because the actual continuous gas phase velocity is higher than the velocity of droplet inside the gas core, using the droplet velocity instead of the actual gas velocity will result in underestimation of j_g.

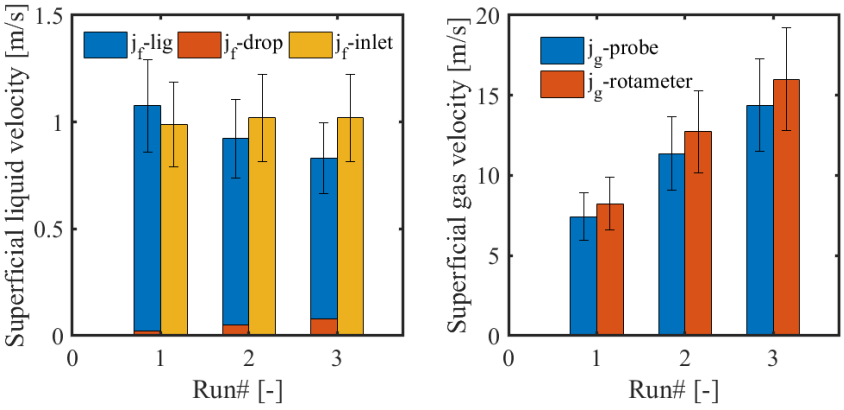

Figure 5-4 Cross check of superficial liquid velocity (left) and superficial gas velocity (right)

5.2.1.3 Droplet size distribution and shape validation

Since there are some models developed for the droplet size distribution in the annular flow, it is desired to compare the measured droplet size distribution with these models to check the measurement reliability. The droplet size distribution model developed by Kataoka et al. [85] is selected for this comparison, which is formulated as

$$\frac{d\Delta}{dy} = -\frac{0.884}{\sqrt{\pi}} e^{-0.781y^2} \tag{5.4}$$

with

$$y = \ln\left(\frac{2.13D}{D_{\max} - D}\right) \tag{5.5}$$

$$D_{\max} = 0.031\frac{\sigma}{\rho_g j_g^{\ 2}} \mathrm{Re}_g^{\ 2/3} \left(\frac{\rho_g}{\rho_f}\right)^{-1/3} \left(\frac{\mu_g}{\mu_f}\right)^{2/3} \tag{5.6}$$

the Δ (D) represents the volume fraction over size D. The droplet size distribution in terms of volume (instead of number density) for a specific flow condition can be estimated using Eq. (5.4)-(5.6). Given that the model is developed for the pure annular flow and most benchmark data are collected in very high j_g (>30 m/s) conditions, only the highest j_g condition (Run 3) in this study will be used for this comparison. In Fig. 5-5, the measured droplet chord length number density distribution for Run 3 in the center of the flow channel is shown as a histogram, and the fitted chord length probability density function (PDF) using lognormal distribution is represented by a red solid line. This fitted distribution cannot be compared to the Kataoka model directly for the following two reasons: First, the chord length is smaller than the droplet diameter unless it is pierced by the probe in the centerline; Second, the fitted PDF is a number density distribution, while the model prediction is a volume distribution.

To convert the chord length distribution to the Sauter mean diameter (D_{sm}) distribution, the chord length distribution is multiplied by a modification factor k, which is the ratio of droplet D_{sm} to the mean chord length (CL_m). For a sphere, the mean chord length can be calculated as:

$$CL_m = \frac{\int_{-R}^{R} CL(r)dr}{\int_{-R}^{R} dr} = \frac{\pi}{2}R = \frac{\pi}{4}D \tag{5.7}$$

where CL is the chord length, D is the particle diameter. Then we can get the diameter to chord length ratio for sphere particles as $k=4/\pi$. The droplet diameter distribution can be estimated by

multiplying the chord length distribution with the modification factor of $4/\pi$. The second step is converting the droplet size distribution in number density $f_n(D)$ to the droplet size distribution in volume $f_V(D)$, which can be achieved by the following relation:

$$f_V(D) = \frac{d\Delta}{dD} = \frac{f_n(D)D^3}{\int_0^{D_{\max}} f(D)D^3 dD} \tag{5.8}$$

In Fig. 5-5, the converted droplet diameter distribution in volume is plotted as a black solid line while the prediction by the Kataoka model is represented by a green dashed line. The PDF converted from the DCCP-4 droplet measurement generally agrees with the model prediction, while the model indicates there should be more small droplets than the experimental results. This deviation is expected given the limitation of the instrumentation. The radial distance between the leading sensor and the trailing sensor is about 0.5 mm, which means the droplet with a diameter smaller than 0.5 mm is very difficult to be detected by both the leading and the trailing sensor. Therefore, the chord length of these small droplets is undetectable to the DCCP-4. Reducing the radial distance between sensors could address this issue, but it will introduce new problems like difficulty in liquid film draining between sensors due to surface tension. If there are liquid films that always connect different sensors, the probe signal will no longer be sensitive to the gas-liquid interface. Although the DCCP-4 is not good at detecting tiny droplets, it is still one of the few methods that can distinguish and measure the dispersed liquid phase in the churn-turbulent to annular transition flow. For the well-developed annular flow (usually very high j_g), the flow structure is quite clear and there are already a lot of methods and data for the droplet size and fraction. But for the churn-turbulent to annular transition flow and low j_g annular flow, the flow field is much more complicated, and very few experimental results are available. This study bridges the gap between different flow regimes and provides experimental data for comprehensive two-phase flow model development, the shortcoming of the DCCP in missing smaller droplets is not critical.

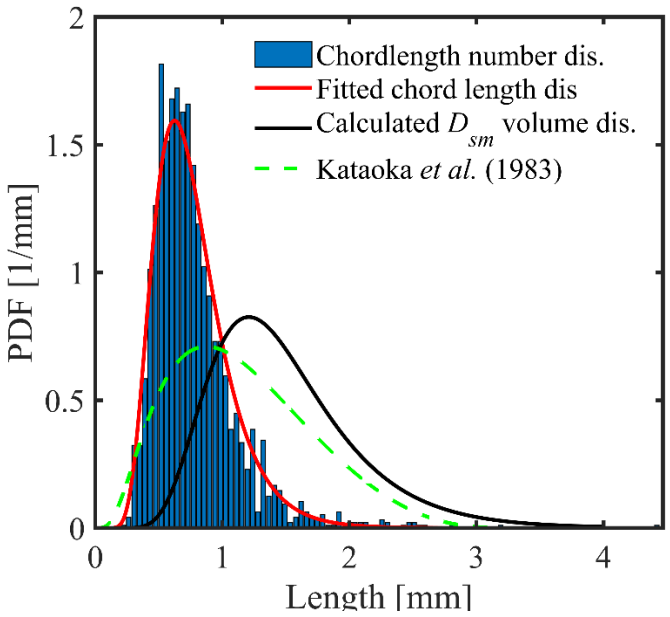

Figure 5-5 Measured droplet chord length distribution at the channel center

As mentioned previously, D_{sm} to CL_m ratio for sphere particles should be $4/\pi$. The D_{sm} of the measured droplets can be calculated as:

$$D_{sm} = \frac{6\alpha_d}{a_{id}} \tag{5.9}$$

where α_d and a_{id} is the volume fraction and the interfacial area concentration of the droplets, respectively. The CL_m can be obtained by averaging the measured chord length. Then the D_{sm} to CL_m ratio for the measured droplets can be compared with the theoretical value to check the shape of the droplets. Figure 5-6 presents the experimental D_{sm} to CL_m ratio for all three conditions. The X-axis is the distance to the wall from the narrow side (Y side), where Y=5 mm is the centerline. The right side of Fig. 5-6 is a schematic of the relation between the shape of a particle and the D_{sm} to CL_m ratio. If the D_{sm} to CL_m ratio is larger than the theoretical value, it means the averaging shape of measured droplets approximately has a major axis vertical to the flow direction and minor axis parallel to the flow direction. If the ratio is less than $4/\pi$, the major axis should be along the flow direction and the minor should be perpindicular to the flow direction. As shown in Fig. 5-6, at the channel center, the measured droplets are spherical. As the measurement location gets closer to the wall, the D_{sm} to CL_m ratios become larger for all three conditions, indicating the droplet changing from spherical to an elliptical shape with major axis perpindicular to the flow direction.

This trend is most obvious for Run 1, which has the lowest j_g. This phenomenon agrees with our understanding of the formation of droplets in the annular flow. The droplets come from the entrainment of the continuous liquid, and are closely related to the liquid waves and ligaments. If the height of a liquid wave or ligament is large enough, it will be entrained by the gas core and disintegrated into droplets. Therefore, the entrained liquid wave or ligament is more likely to have a shape with a major axis perpindicular to the flow direction since its height from the wall should be large, otherwise, it could not be separated from the bulk liquid. In the near-wall region, there is a high probability that the probe detects dispersed liquid particles that were just separated from the continuous liquid and preserve their original shape. Therefore, the D_{sm} to CL_m ratio in the near-wall region is larger. For the high j_g flow condition, the disintegration process happens quicker than the low j_g condition. This explains why the increasing of the D_{sm} to CL_m ratio near the wall for the high j_g condition (Run 3) is not as obvious as the low j_g condition (Run 1).

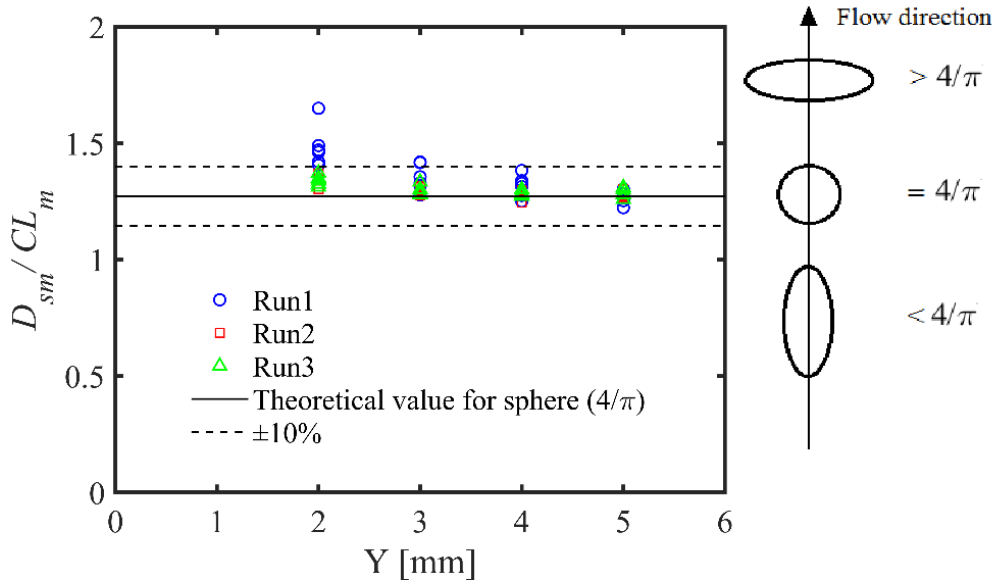

Figure 5-6 Ratio of Sauter mean diameter to the mean chord length of measured droplets

5.2.2 Local Measurement Results

The DCCP-4 local measurement results of Runs 1-3 are shown in Figs 5-7 to 5-9. The X and Y-axis represent the wide side and the narrow side of the flow channel, while X=100 mm and Y=5 mm is the symmetric axis of the cross-section. The value of the two-phase flow parameters is reflected by the color of the contour and the scale is indicated by the color bar. Each figure contains

6 subplots, the upper three subplots are parameters of droplets and the lower three subplots are liquid ligament parameters. From left to right, each subplot shows volume fraction (α), interfacial area concentration (a_i), and the interface velocity (v). It can be observed that the droplet spatial distribution is center peaked and the ligament fraction peaks near the wall, which is expected at the churn-turbulent to annular flow transition. To get a better view of the effect of the inlet superficial gas velocity, the measured two-phase flow parameters are line-averaged over the narrow side (Y), and their distributions along the wide side are plotted in Fig. 5-10. As the j_{g0} increases from 9.38 to 19.91 m/s, the droplet volume fraction increases from 0.3% to 0.6%, while the ligament volume fraction at X=100 mm decreases from 11% to about 2%. For a typical annular flow condition, there should be no ligament that exists in the channel center since the annular flow is characterized by a gas core with droplets inside. From this point of view, even Run 3 (j_{g0} =19.91) may not be the typical annular/annular mist flow. Other than the void fraction, IAC and the interface velocity also show reasonable trends as the j_{g0} increases. The droplet IAC increases with the gas flow. This is because more liquid is entrained to the gas core and becomes droplet. The ligament IAC decreases with the increasing j_{g0}, since the flow is getting closer to the typical annular flow and the irregular ligament interface near the wall becomes small. The droplet interface velocity is close to the inlet superficial gas velocity, while the ligament interface velocity is lower than the droplet interface velocity.

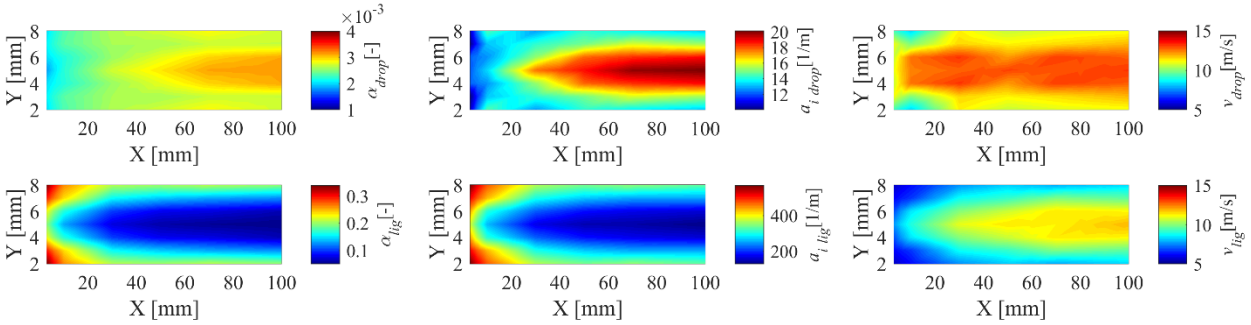

Figure 5-7 Local measurement results of Run 1 (j_f =0.99 m/s, j_{g0}=9.38 m/s)

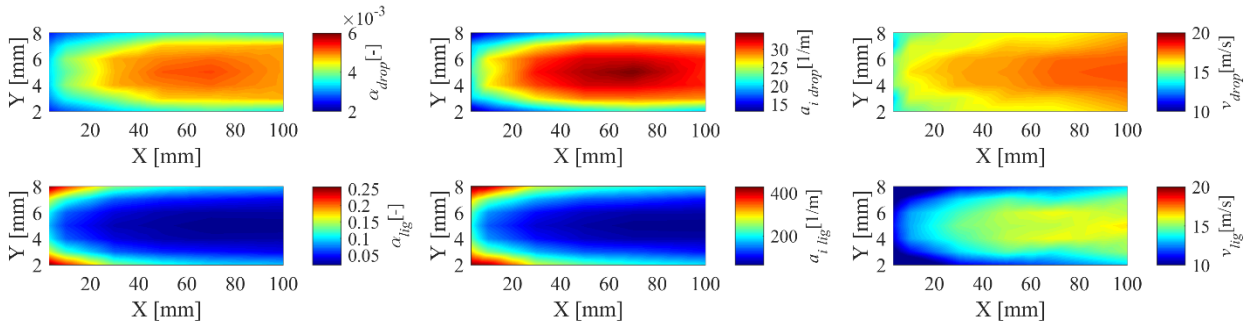

Figure 5-8 Local measurement results of Run 2 (j_f=1.02 m/s, j_{g0}=15.34 m/s)

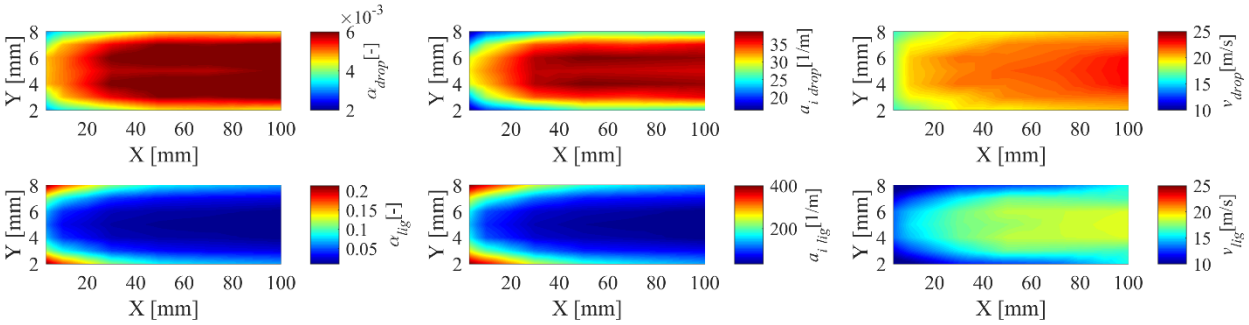

Figure 5-9 Local measurement results of Run 3 (j_f=1.02 m/s, j_{g0}=19.91 m/s)

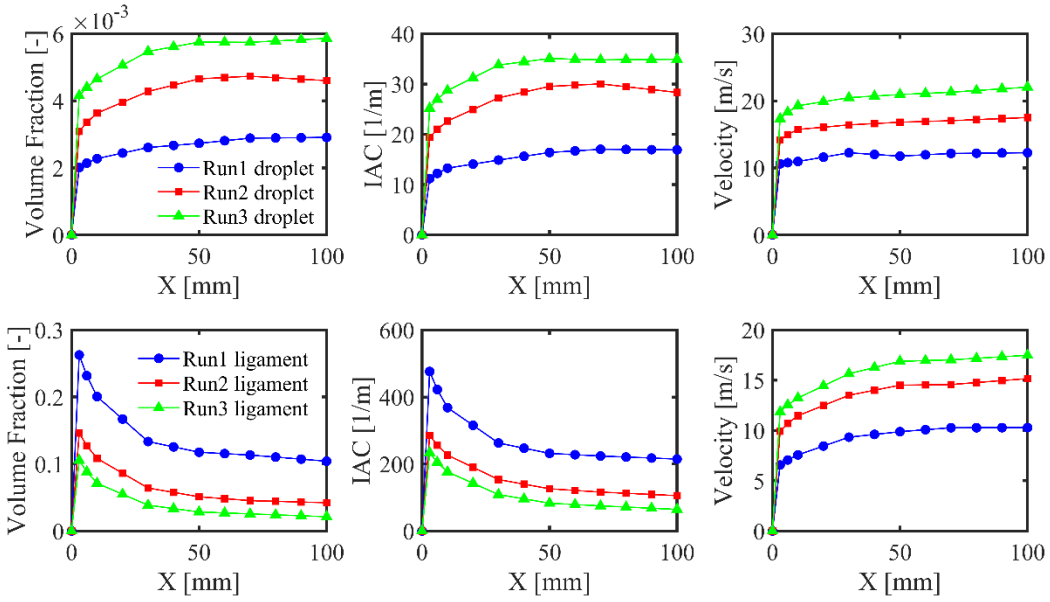

Figure 5-10 Line-averaged DCCP-4 local measurement results

5.3 Wispy Annular Flow Experiment

In this section, the experiment results of wispy-annular flow (Runs 4-7) will be discussed.

5.3.1 Results Verification

Using the same approach mentioned in section 5.2.1.2, the uncertainty of the local data can be evaluated by area-averaging the results and comparing them with the bulk instrumentation, as shown in Fig. 5-11. The error bar represents ±20%. The superficial liquid velocity measured by the DCCP-4 agrees well with the vortex flowmeter results and the error is less than 10%. The superficial gas velocity measured by DCCP-4 is slightly lower than the rotameter measurement, which is expected since the droplet velocity used in the calculation should be less than the continuous gas velocity, which cannot be detected by the probe.

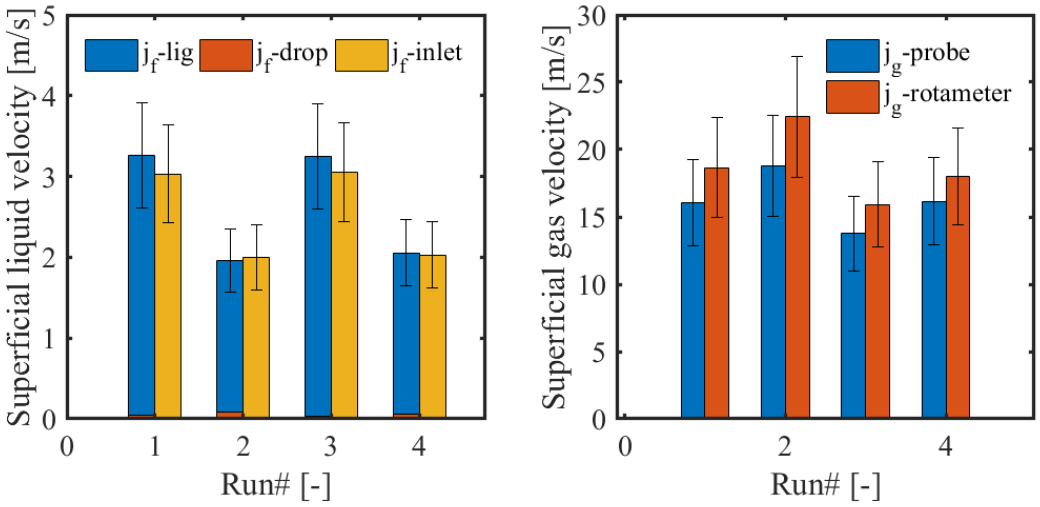

Figure 5-11 Cross check of superficial liquid flow rate (left) and superficial gas flow rate (right)

5.3.2 DCCP-4 Local Measurement Results

The local measurement results for wispy annular conditions (Runs 4-7) are plotted in Figs 5-12 to 5-15, respectively. The droplet volume fraction shows center peaked distribution while the ligament volume fraction shows wall peaked distribution. The maximum ligament IAC is more than 1500 1/m for all these four flow conditions.

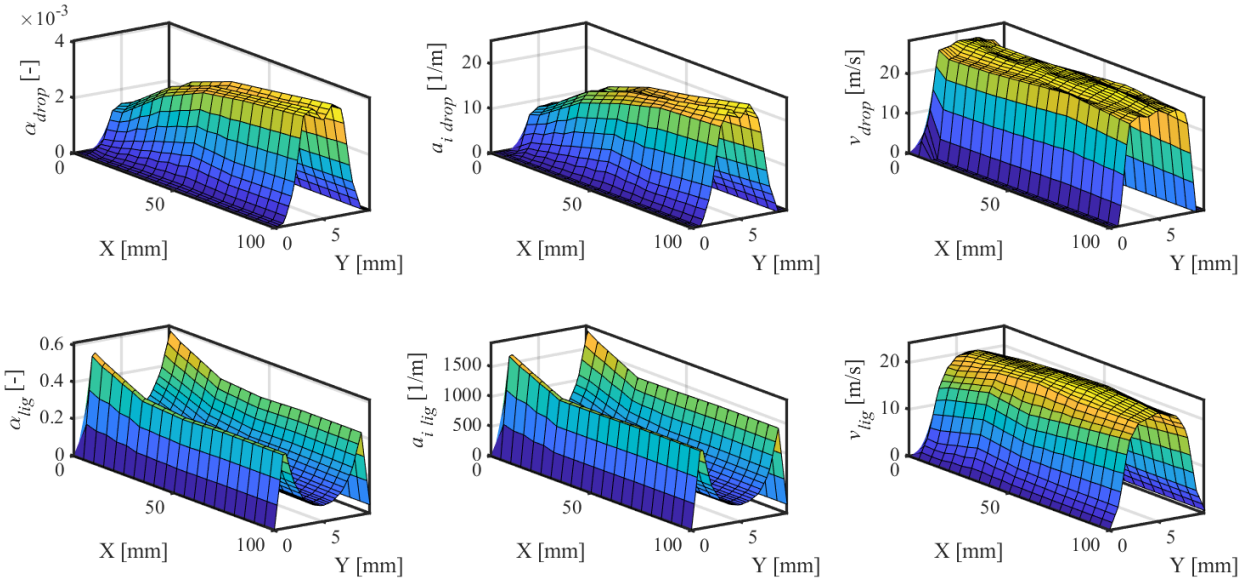

Figure 5-12 Local measurement results of Run 4 (j_f=3.03 m/s, j_{g0}=24.00 m/s)

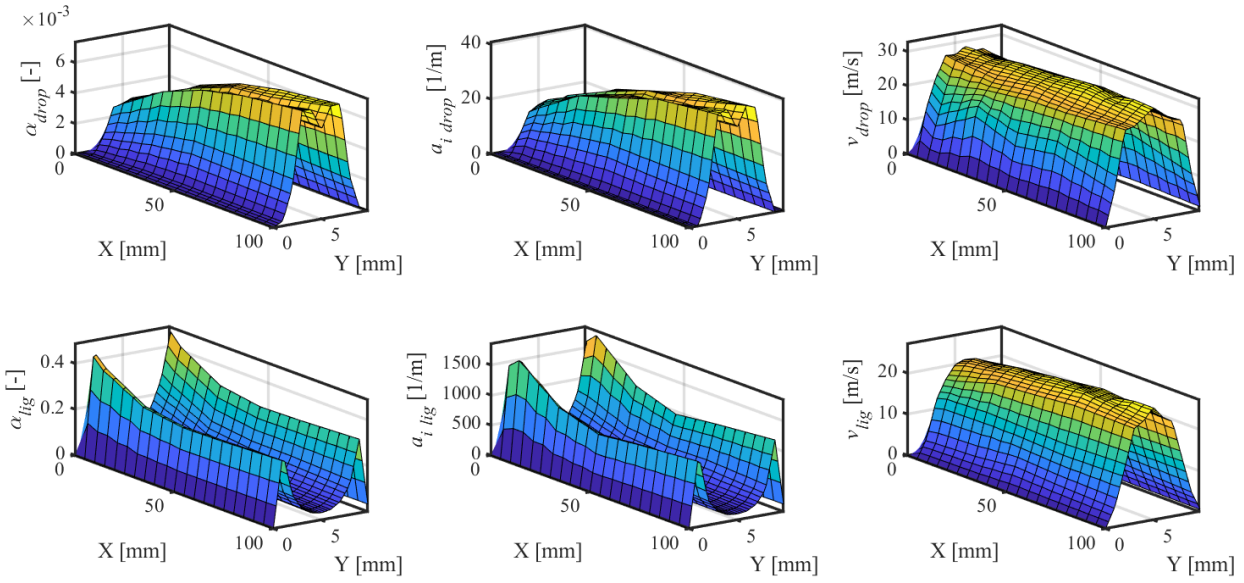

Figure 5-13 Local measurement results of Run 5 (j_f=2.00 m/s, j_{g0}=26.21 m/s)

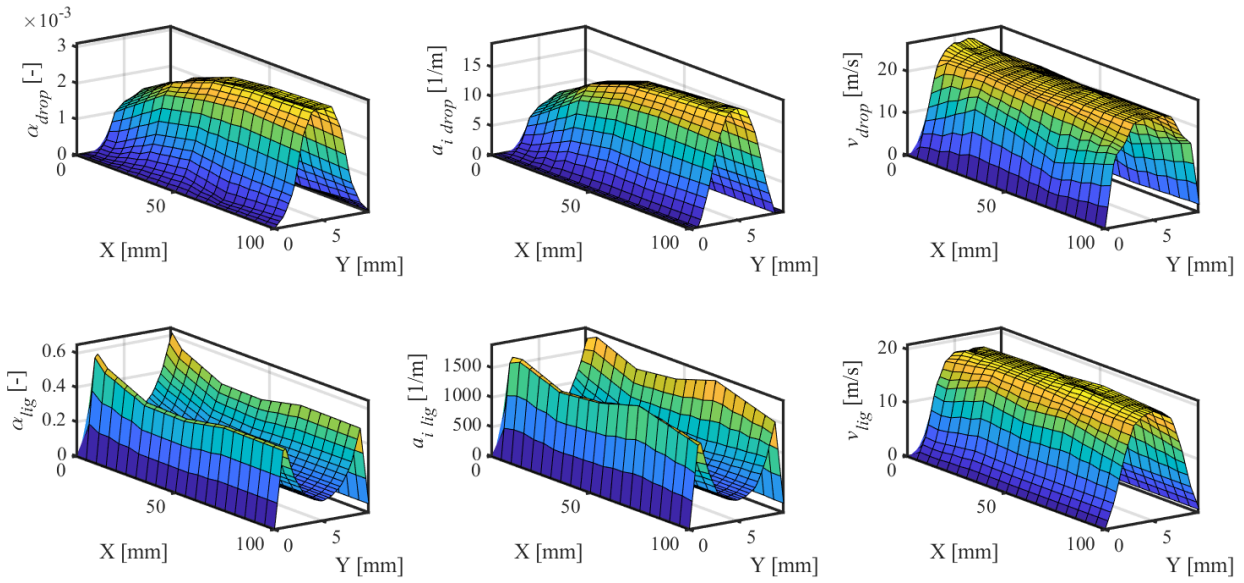

Figure 5-14 Local measurement results of Run 6 (j_f=3.05 m/s, j_{g0}=19.95 m/s)

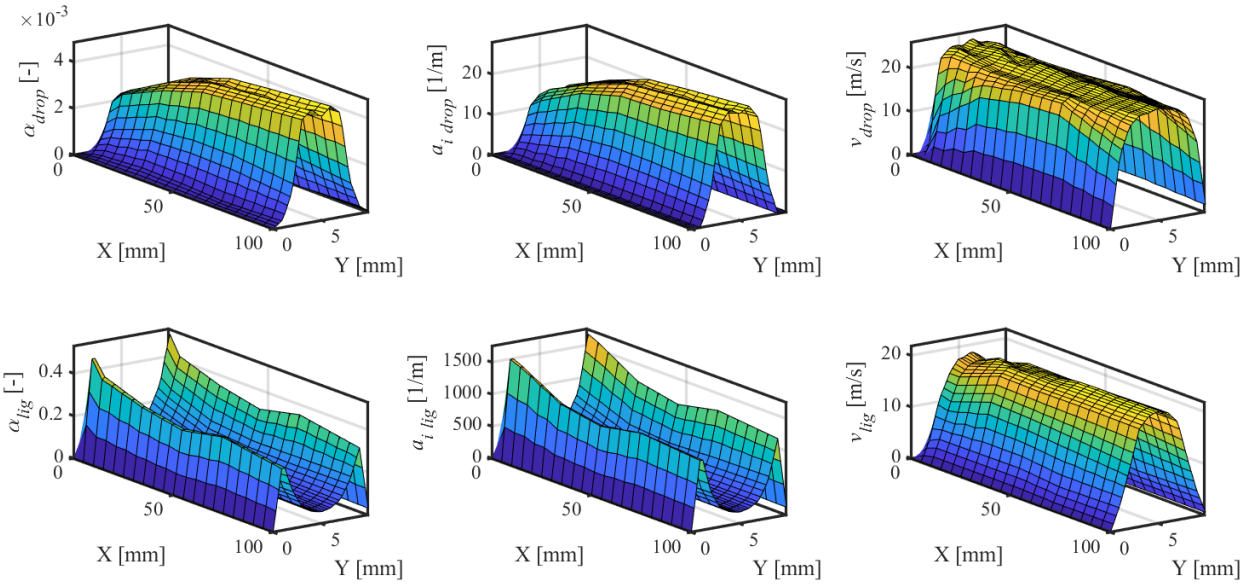

Figure 5-15 Local measurement results of Run 7 (j_f=2.03 m/s, j_{g0}=20.61 m/s)

The line-averaged results over the Y direction are plotted in Fig. 5-16. The empty symbol represents flow conditions with the superficial liquid velocity of about 3 m/s and the solid symbol represents flow conditions with the superficial liquid velocity of about 2 m/s. When fixing j_f and

increasing the j_g, the droplet fraction increases, and the ligament fraction decreases. If j_g is fixed and increases j_f, the droplet fraction decreases, and the ligament fraction increases.

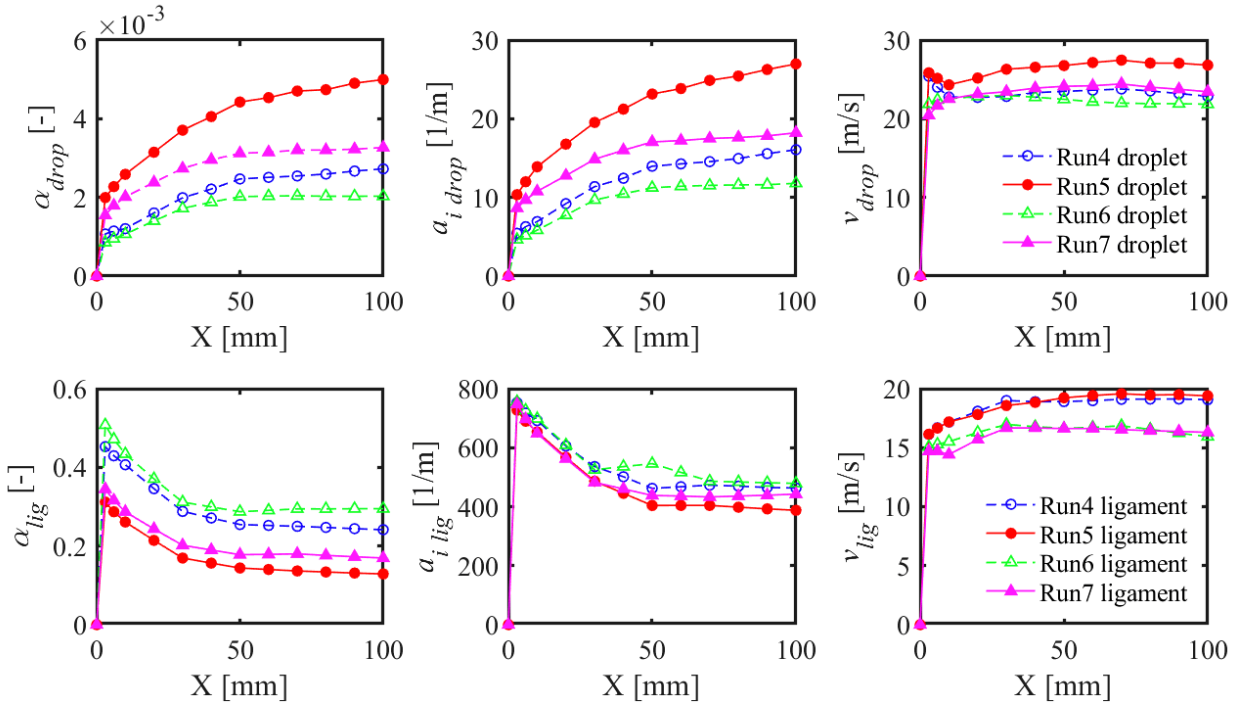

Figure 5-16 Line-averaged DCCP-4 local measurement results for wispy-annular flow

5.3.3 Film Thickness Measurement Results

As mentioned in 5.1, the film thickness probe is also used to measure the film dynamics at wispy-annular flow, and the test matrix is shown in Fig. 5-17. The solid symbol represents the conditions measured by both the film thickness probe and the DCCP-4, while the empty symbol are the conditions measured by the film probe only. The measured mean film thickness is plotted against the local superficial gas velocity in Fig. 5-18. As the superficial gas velocity increases from 10 m/s to 25 m/s, the mean film thickness at X=70 mm decreases from 1.2-1.4 mm to 0.75-0.85 mm. The effect of superficial liquid velocity on film thickness is not obvious once the superficial liquid velocity is more than 1 m/s.

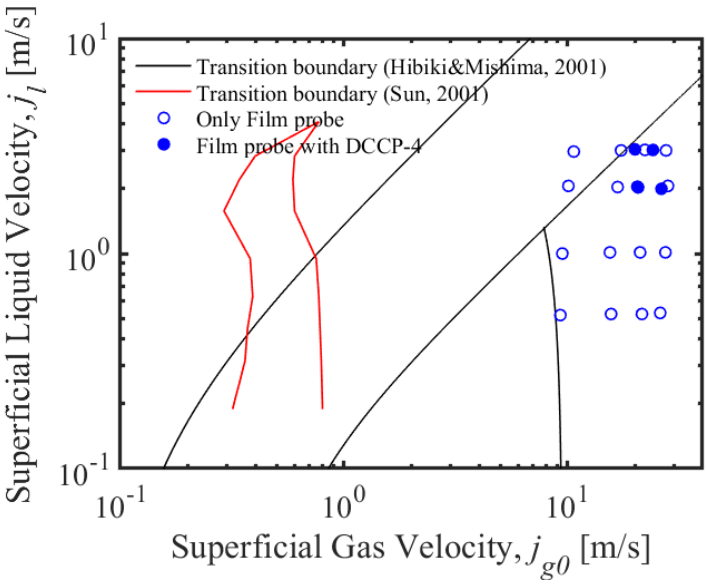

Figure 5-17 Test matrix of the film thickness experiment

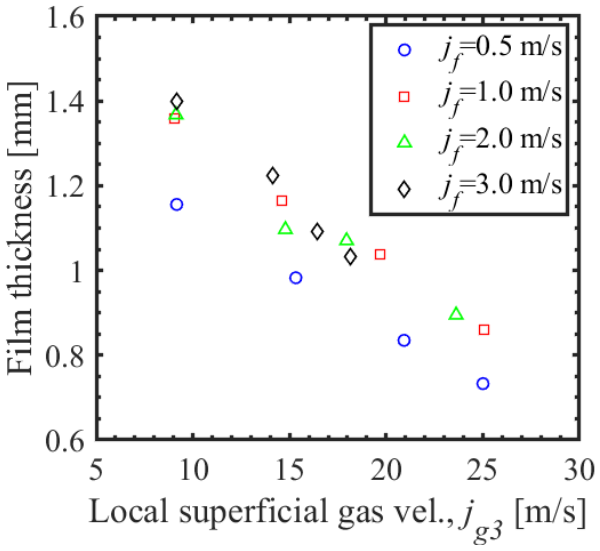

Figure 5-18 Averaged film thickness for various conditions

Given that the most interfacial area in the near-wall region of annular flow mainly exists in terms of the interface between the continuous gas core and the liquid film, the IAC for annular flow can be predicted by measuring the instantaneous film thickness, namely the wave structure. The schematic of getting IAC from the wave structure is presented in Fig. 5-19. For a 2-D control volume as indicated by two black lines in Fig. 5-19, the interfacial area concentration in this control volume can be expressed as

$$a_i(x) = \frac{T_i}{T\Delta x} \tag{5.10}$$

where T_i is the time that interface exists within the control volume, which is expressed as red lines in Fig. 5-19. T is the total time to be averaged, and Δx is the spatial interval of the IAC, which is set to be 40 μm in this study. The liquid fraction for each location is known given the measured wave structure as a function of time. The liquid volume fraction and the IAC distributions obtained from the film thickness measurement results are plotted in Figs. 5-20 and 5-21 respectively. For each figure, the left subplot shows the effect of the superficial liquid velocity and the right subplot shows the effect of the superficial gas velocity. As the superficial gas velocity increases, the liquid fraction distribution becomes closer to the wall, and the IAC distribution becomes narrower and steeper. This is because the fluctuation of the liquid wave is smaller as the superficial gas velocity increases, and the gas-liquid interface is more stable and closer to a straight line. If the interface is a straight line parallel to the wall, the IAC will be infinity at the interface location and be zero at other locations. This is the laminar, undisturbed film limit.

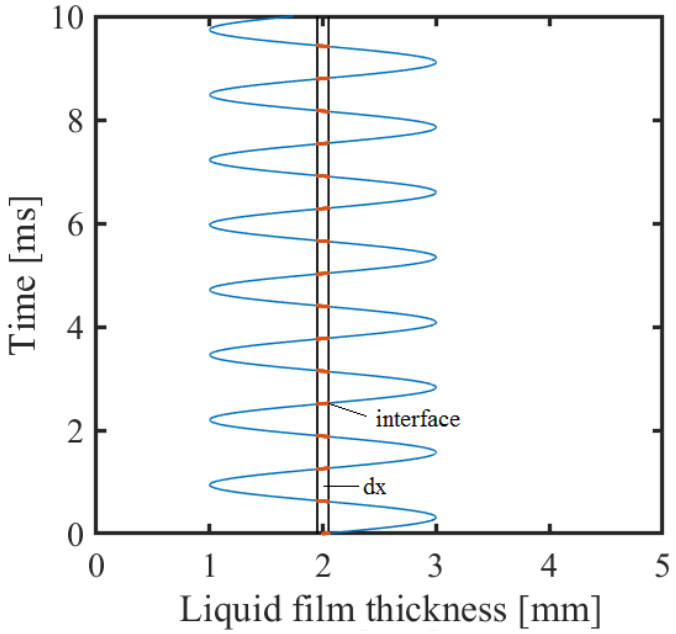

Figure 5-19 Schematic of getting IAC from wave structure

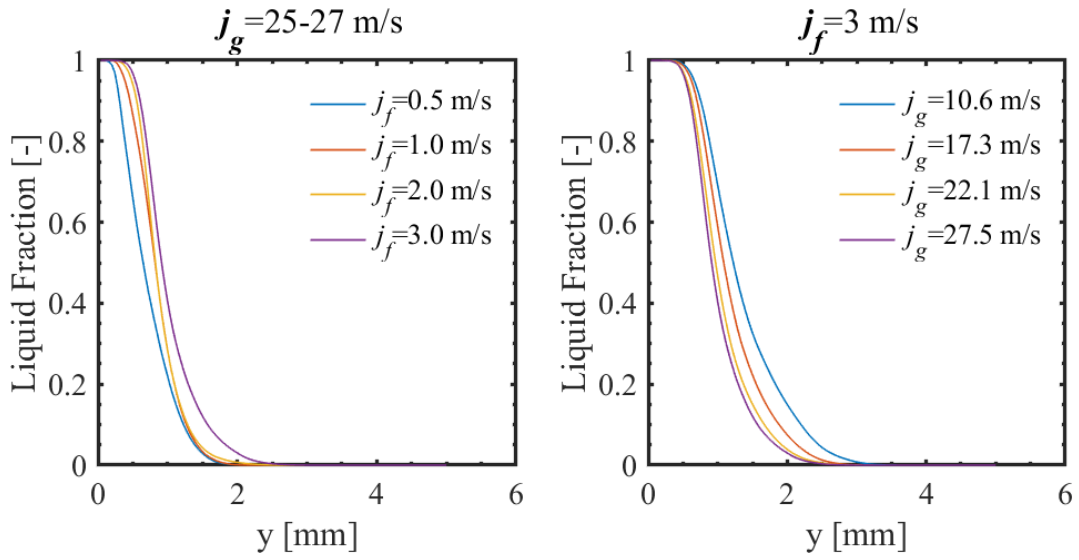

Figure 5-20 Near wall liquid volume fraction profiles by the film probe

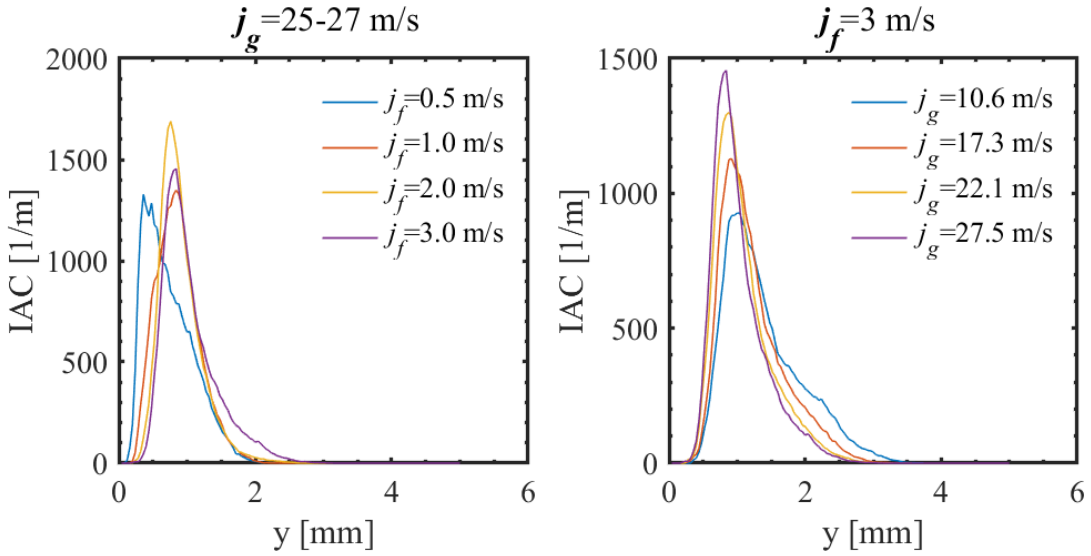

Figure 5-21 Near wall IAC profiles by the film probe

If two film thickness probes are separated a known distance in the flow direction, like probe 5, 11 in Fig. 4-4, the average time for waves to go through these two probes can be obtained by cross-correlation. Then the averaged wave velocity can be calculated by dividing the separation distance of these two probes with the time lag of the signals. The calculated wave velocity at X= 70 mm is plotted against the local superficial gas velocity in Fig. 5-22. When the superficial liquid velocity

is low, the wave velocity is lower than the superficial gas velocity. If the superficial liquid velocity is high, the wave velocity is close to or even higher than the superficial gas velocity.

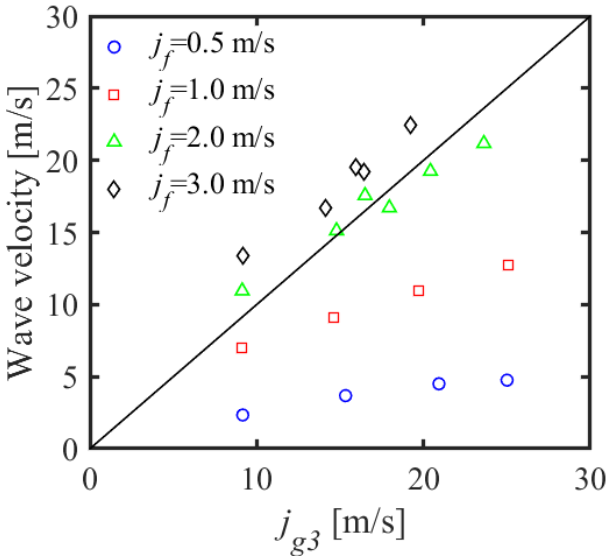

Figure 5-22 Wave velocity measurement result

5.3.4 Comparison between Film Probe and DCCP-4 Results

Since both the DCCP-4 and film probe can get near-wall distributions of liquid volume fraction and IAC, it is desired to compare these two results. The comparison of DCCP-4 and film probe results for Runs 4, 5, 6, and 7 are shown in Figs 5-23 to 5-26, respectively. For the near-wall location Y=1 mm, the measured IAC and liquid volume fraction agree well with the profile calculated from the wave structure by the film probe. For other locations closer to the channel center, the DCCP-4 measured more IAC and liquid fraction than the film probe. This is expected as the film probe is designed to measure the conductance of the liquid film, which is related to the film thickness. If the film structure is too complicated – containing bubbles inside or the shape of the liquid ligament is too irregular – the film probe may not able to distinguish these interfaces.

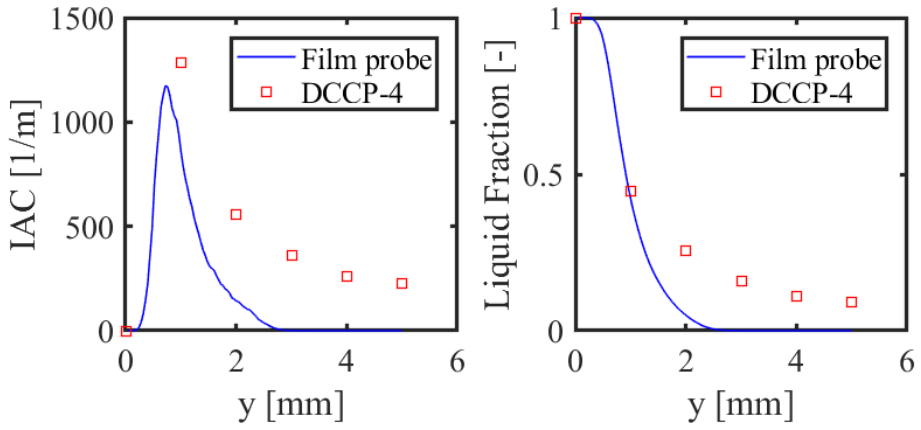

Figure 5-23 Comparison of DCCP-4 and film probe results for Run 4 (j_f=3.03 m/s j_g=24.00 m/s)

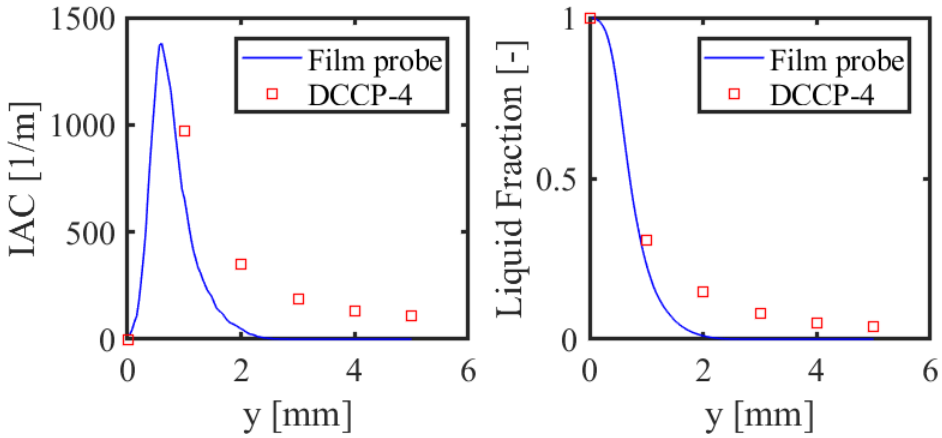

Figure 5-24 Comparison of DCCP-4 and film probe results for Run 5 (j_f=2.00 m/s j_g=26.21 m/s)

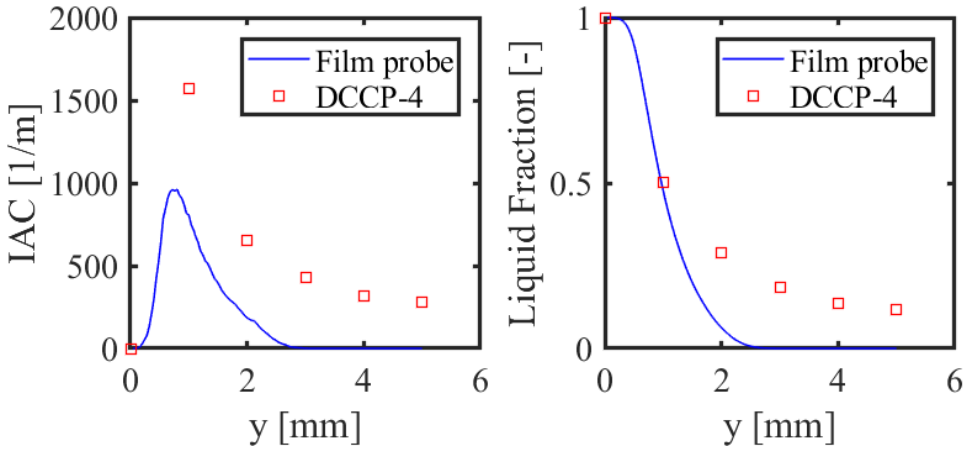

Figure 5-25 Comparison of DCCP-4 and film probe results for Run 6 (j_f=3.05 m/s j_g=19.95 m/s)

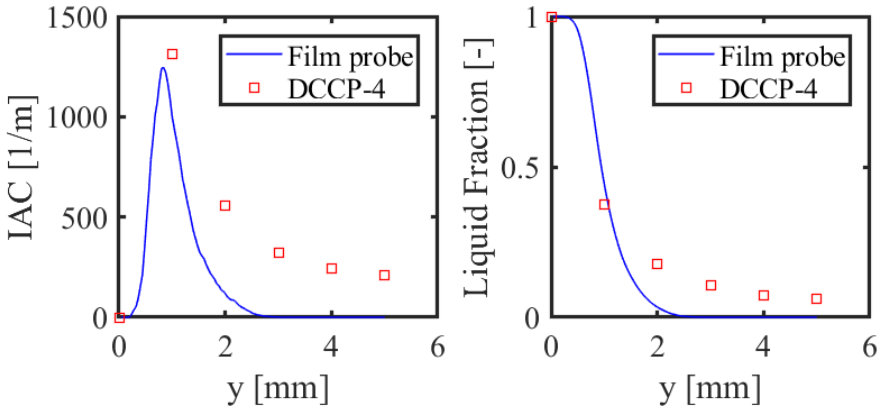

Figure 5-26 Comparison of DCCP-4 and film probe results for Run 4 (j_f=2.03 m/s j_g=20.61 m/s)

6. ANNULAR FLOW WAVE STRUCTURE

Since the disturbance wave is the primary source of the entrained droplet, a solid understanding of disturbance wave properties is necessary for the mechanistic interfacial area transport model development in annular flow. By reviewing the disturbance wave database of annular flow, it can be found that most previous data focus on the low liquid velocity region and very few data are available with the superficial liquid velocity (j_f) larger than 0.3 m/s [86]. Therefore, the priority of this chapter is developing a comprehensive database over a wide range of flow conditions, especially high j_f conditions. Both the static parameters (mean film thickness, wave height, base film thickness) and dynamic parameters (wave velocity, wave frequency) are measured and analyzed. A comprehensive evaluation of various models for wave properties is performed using the new database, which can guide future modeling and code development.

6.1 Experimental Setup and Instrumentation

6.1.1 Experimental Facility

The schematic of the test facility is shown in Fig. 6-1, which is an air-water two-phase flow system. The test section is made of an acrylic pipe with an inner diameter of 25.4 mm, and the total height is 3.81 m. The two-phase flow mixture injection systems are located at both the top and the bottom of the test section, which consists of a sparger and two water flow channels. The sparger is made up of porous material with an average pore size of 10 μm. The water supply line is divided into two lines before entering the two-phase mixture injector, namely primary flow and secondary flow. The secondary flow shears the bubbles off in the sparger and then mixes with the primary flow. Air is supplied by a compressor and a tank, and a pressure regulator is used to maintain a constant pressure. Three rotameters with different measuring ranges (0.01-0.57 m^3/h, 0.14-1.42 m^3/h 2.83-28.32 m^3/h, respectively) are used to measure the gas flow rate with an accuracy of ±2% of full scale. Water is supplied via a centrifugal pump and controlled by valves and a frequency converter. The water flow rate is measured using electro-magnetic liquid flow meters with an accuracy of ±1%. Three measurement ports equipped with a parallel wire film thickness probe are located at z/D_h = 15, 78, 141, respectively. Since entrainment/deposition influences the film thickness, it is important to ensure the flow is at an equilibrium condition, so the results are comparable to other

data and models. Kataoka et al. [87] proposed a criterion to estimate the distance required to reach the equilibrium condition:

$$\frac{z}{D_H} = \frac{440We'^{0.25}}{\mathrm{Re}_f^{0.5}} \tag{6.1}$$

where We' is Weber number for entrainment

$$We' = \frac{\rho_g j_g^2 D}{\sigma}\left(\frac{\Delta\rho}{\rho_g}\right)^{1/3} \tag{6.2}$$

and Re_f is liquid Reynolds number

$$\mathrm{Re}_f = \frac{\rho_f j_f D}{\mu_f} \tag{6.3}$$

Using this criterion, the maximum required developing length for the current experimental conditions is z/D_h = 85. Therefore, the film measurement results at z/D_h = 141 will be presented and used for model evaluation in this study.

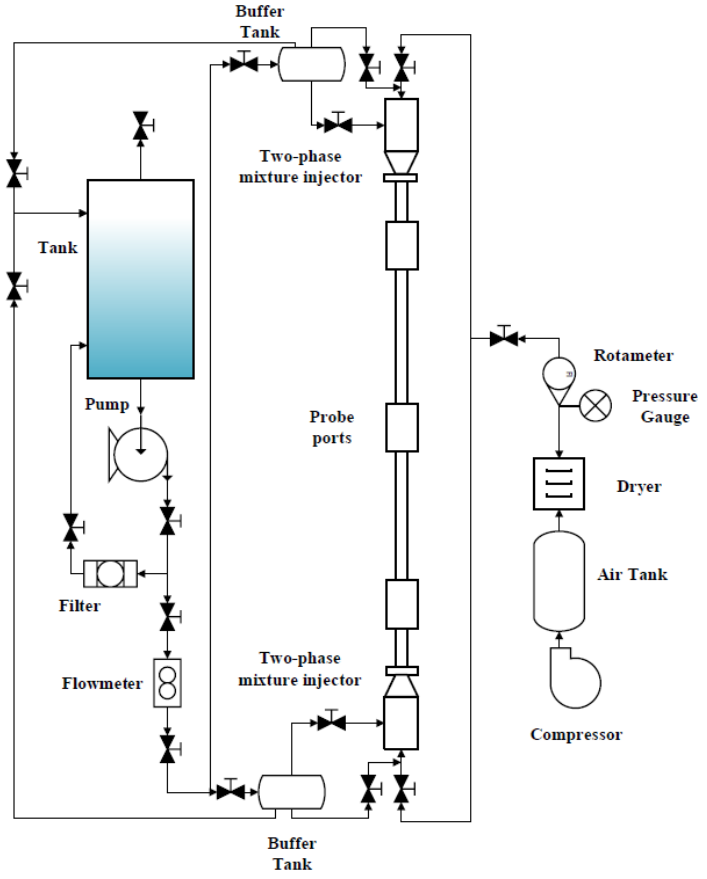

Figure 6-1 Schematic of the test facility

6.1.2 Film Thickness Probe

In this study, the parallel-wire conductance probe is used to measure the film thickness. The schematic of the probe is shown in Fig. 6-2. The probe is made of two stainless steel needles with a diameter of 0.28 mm, the separation distance between two electrodes is 3 mm, and the intrusive length is 9 mm. These two electrodes are connected to a circuit and the voltage between them is measured. Since the voltage between two electrodes is related to the film thickness (conductance), the film thickness measurement can be achieved by measuring the voltage and convert it into film thickness using a calibration curve. The calibration curve is obtained by measuring the voltage signals with various known film thickness. As shown in Fig. 6-3, the calibration is performed in two different surfaces, the flat surface, and the pipe inner surface. By installing the probe on a flat surface, the film thickness can be easily defined as the distance between the liquid free surface and the flat surface as shown in Fig. 6-3 (b). The calibration curve can be obtained by applying different amounts of water on the surface and measuring the voltage and the film thickness. But since the test section is a curved pipe surface, it is desired to perform the calibration with the probe installed in the test section. However, it is difficult to generate an annular film with a uniform known thickness in a pipe, especially considering the intrusive structure of the probe. Therefore, in the calibration process, the film thickness is defined as the largest distance between the free surface and the wetted inner wall, as shown in Fig. 6-3 (a). The calibration curves using these two different calibration approaches are presented in Fig. 6-4. For the thick film, the curved surface effect is not obvious, and the calibration curves are close to each other. For the thin film, the calibration curves are slightly different from each other, which should result from the surface curvature effect. In general, the calibration curves obtained using two different approaches are similar, and the flat surface calibration curve is used to convert the voltage signal into the film thickness signal due to its accuracy in film thickness definition. To measure the wave velocity, two parallel-wire probes are arranged in the same circumferential location with a separation in the axial direction of 10 mm. Since the measurement locations of these two probes are very close, the measured film thickness time traces of these two probes would be similar. The time lag between these two signals can be obtained by cross-correlation and the average wave velocity can be calculated. The data acquisition frequency is 50 kHz, and the sampling time is 60 s.

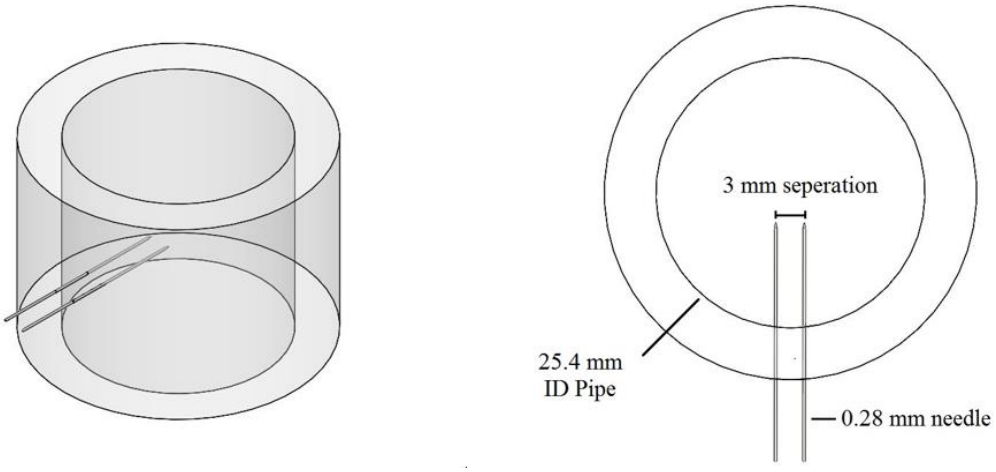

Figure 6-2 Schematic of the parallel-wire film thickness probe

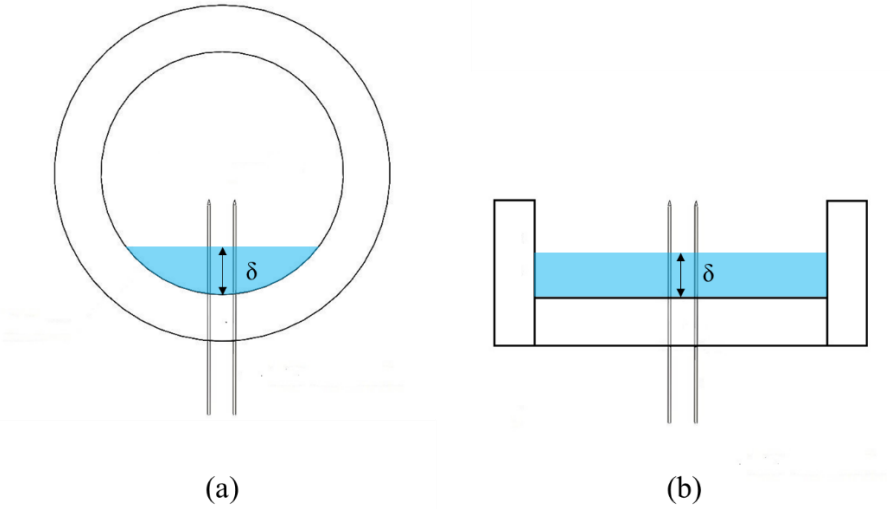

Figure 6-3 Schematic of two different calibration approaches (a) calibration in a pipe (b) calibration on a flat surface

6.1.3 Test Matrix

The test matrix consists of 30 flow conditions, which are plotted in Fig. 6-5 on different flow regime maps. The inlet superficial gas velocity ranges from 10 m/s to 30 m/s and the inlet superficial liquid velocity ranges from 0.06 m/s to 2 m/s. As mentioned in the introduction, most pervious experiments are performed in flow conditions with relatively small superficial liquid velocity (j_f <0.3 m/s). In this study, the conditions with high superficial liquid velocities (j_f =0.5,

1.0, and 2.0 m/s) are also covered to address the experimental gap. Inlet conditions, as well as the experimental results, can be found in Appendix B.

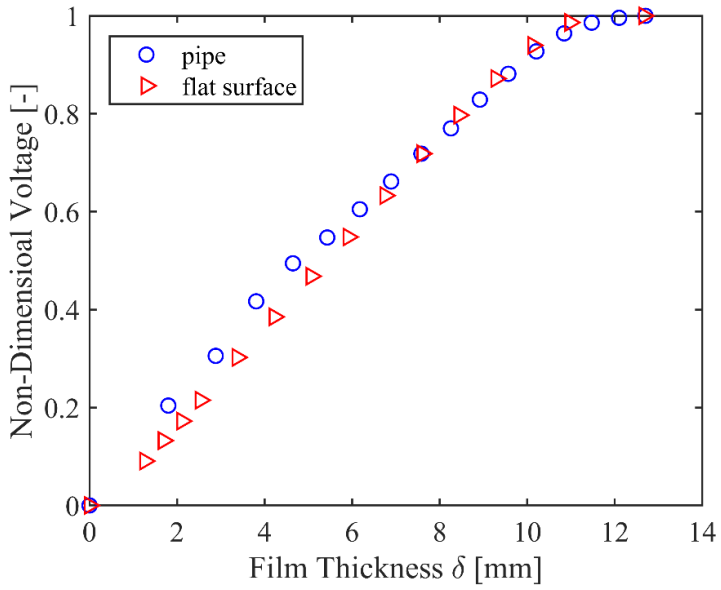

Figure 6-4 Calibration curves for two different calibration approaches

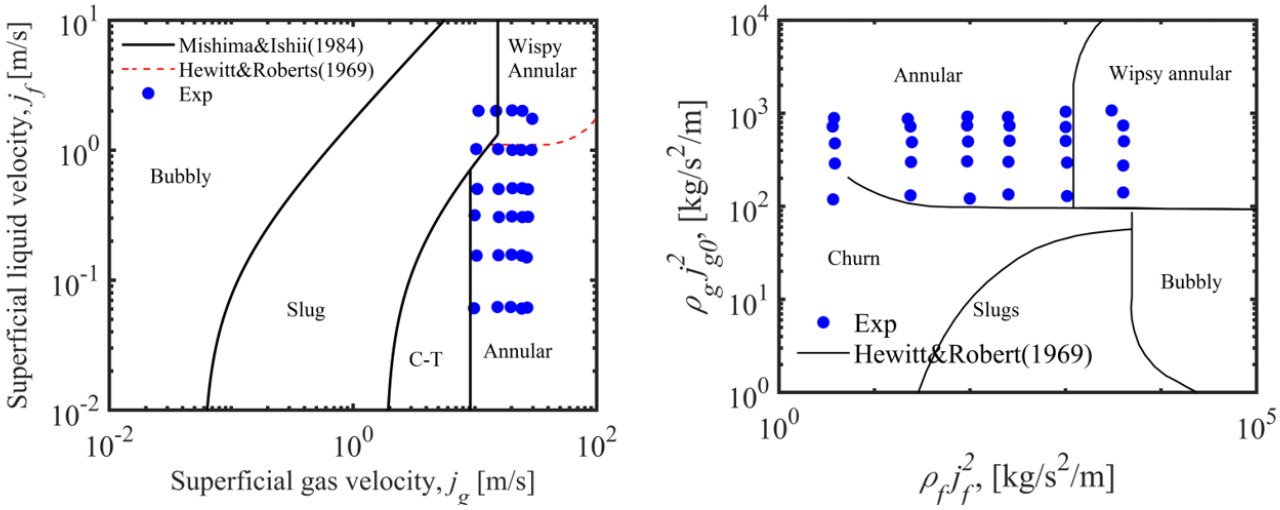

(a) (b)

Figure 6-5 Test Matrix plotted in flow regime maps

(a) Mishima&Ishii map [57] (b) Hewitt&Roberts map [83]

6.2 Experimental Results

6.2.1 Average Film Thickness

The effects of superficial gas velocity and superficial liquid velocity on average film thickness are shown in Fig. 6-6 (a) and (b), respectively. For a fixed superficial liquid velocity, the average film thickness decreases with the increasing of superficial gas velocity, and the decreasing gradient becomes less for higher superficial gas velocity. For the superficial liquid velocity effect, the film thickness increases with the superficial liquid velocity for j_f <0.5 m/s, then the increasing slope becomes very small when 0.5 m/s < j_f <1.0 m/s.

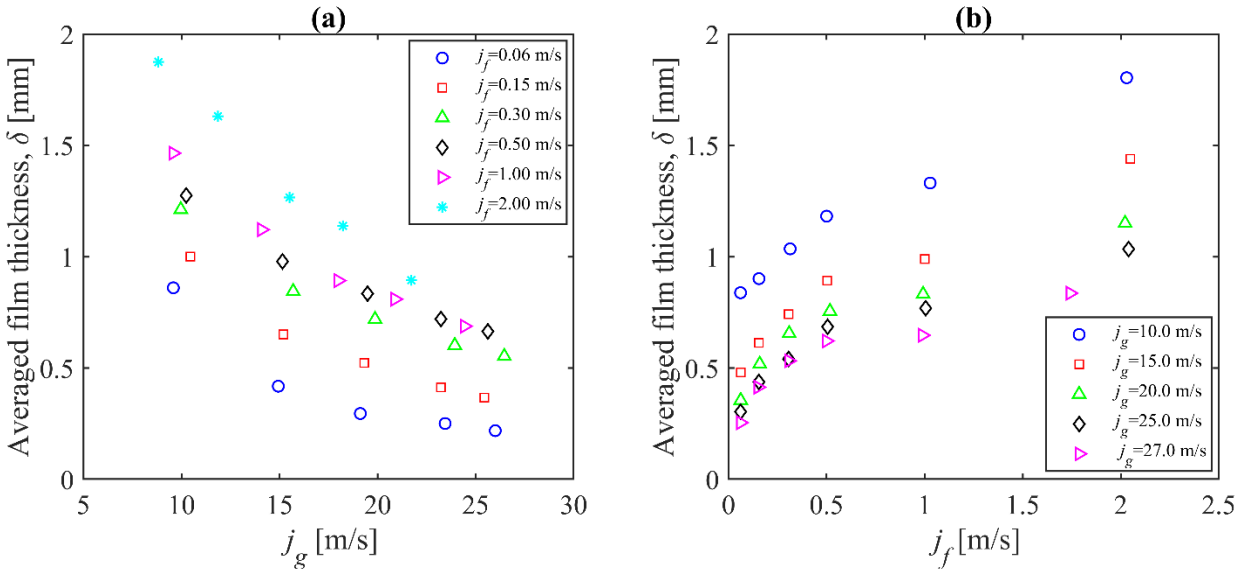

Figure 6-6 Average film thickness (a) effect of superficial gas velocity (b) Effect of superficial liquid velocity

Table 6-1 summarizes several previous film thickness correlations. They are evaluated using the current data and the result is presented in Figs. 6-7 and 6-8. Fig. 6-7 shows the comparison of data and various models' prediction with the superficial gas velocity increasing. Each subplot contains flow conditions with a similar superficial liquid velocity. The error bar of the data point represents ±10%. Among the six models evaluated in this study, the correlations by Ju et al. [88] and Berna et al. [89] have relatively good performance for low j_f conditions (j_f = 0.06-0.50 m/s). For high j_f conditions (j_f = 1.00-2.00 m/s), the Ju model overestimates the film thickness, because the test

conditions are out of the application range for the correlation. Berna still can predict the film thickness for high j_f conditions (j_f = 1.00-2.00 m/s). Fig. 6-8 provides the mean absolute percentage error (MAPE) over all flow conditions for each model. The MAPE of the Ju and Berna models are less than 15%. The author suggests using the Ju model for j_f < 0.5 m/s and using the Berna model for j_f > 0.5 m/s.

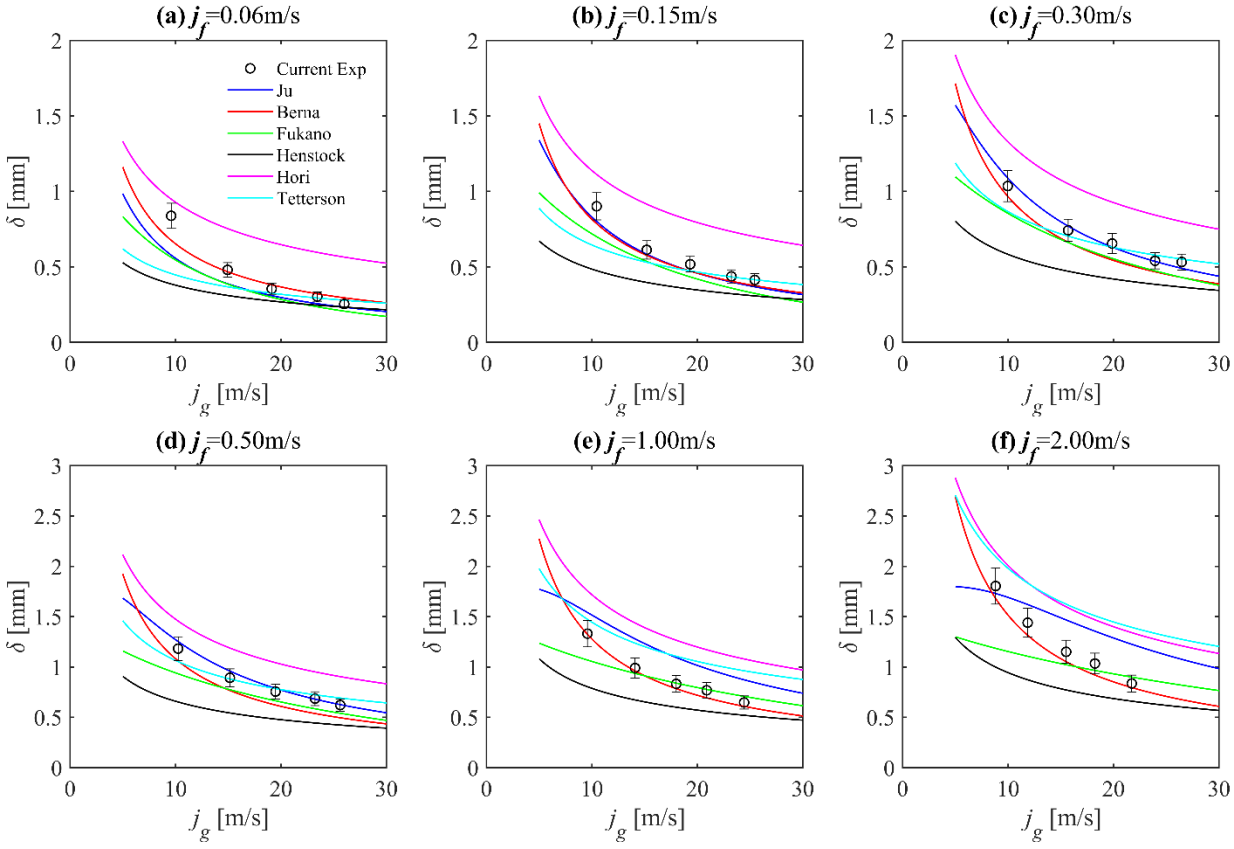

Figure 6-7 Comparison of average liquid film thickness with predictions of various correlations

Table 6-1 Previous models on average film thickness

Reference	Models
Berna [89]	$\frac{\delta}{D}=7.165\mathrm{Re}_g^{-1.07}\mathrm{Re}_f^{0.48}\left(\frac{Fr_g}{Fr_f}\right)^{0.24}$
Fukano [90]	$\frac{\delta}{D}=0.0594\exp\left(-0.34Fr_g^{0.25}\mathrm{Re}_f^{0.19}x^{*0.6}\right)$ $x^*=\frac{j_g\rho_g}{j_g\rho_g+j_f\rho_f}$
Henstock [91]	For vertical flow $\frac{\delta}{D}=\frac{6.59F}{\left(1+1400F\right)^{0.5}}$ For horizontal flow $\frac{\delta}{D}=\frac{6.59F}{\left(1+850F\right)^{0.5}}$ $F=\frac{1}{\sqrt{2}\mathrm{Re}_g^{0.4}}\frac{\mathrm{Re}_f^{0.5}}{\mathrm{Re}_g^{0.9}}\frac{\mu_f}{\mu_g}\frac{\rho_g^{0.5}}{\rho_f^{0.5}}$
Hori [92]	$\frac{\delta}{D}=0.905\mathrm{Re}_g^{-1.45}\mathrm{Re}_f^{0.90}Fr_g^{0.93}Fr_f^{-0.68}\left(\frac{\mu_f}{\mu_{f,ref}}\right)^{1.06}$
Ju [88]	$\frac{\delta}{D}=0.071\tanh\left(14.22We_f^{0.24}We_g^{"-0.47}N_{\mu_f}^{0.21}\right)$ $We_f=\frac{\rho_f j_f{}^2D}{\sigma},\ We_g^{"}=\frac{\rho_g j_g{}^2D}{\sigma}\left(\frac{\Delta\rho}{\rho_g}\right)^{1/4},\ N_{\mu_f}=\frac{\mu_f}{\sqrt{\rho_f\sigma\sqrt{\frac{\sigma}{g\Delta\rho}}}}$
Tatterson [93]	For vertical flow $\frac{\delta}{D}=\frac{6.59F}{\left(1+1400F\right)^{0.5}}$ For horizontal flow $\frac{\delta}{D}=\frac{6.59F}{\left(1+850F\right)^{0.5}}$ $F=\frac{\gamma\left(\mathrm{Re}_{ff}\right)}{\mathrm{Re}_g^{0.9}}\frac{\mu_f}{\mu_g}\frac{\rho_g^{0.5}}{\rho_f^{0.5}}$ $\gamma\left(\mathrm{Re}_{ff}\right)=\left[\left(0.707\mathrm{Re}_{ff}^{0.5}\right)^{2.5}+\left(0.0379\mathrm{Re}_{ff}^{0.9}\right)^{2.5}\right]^{0.4}$

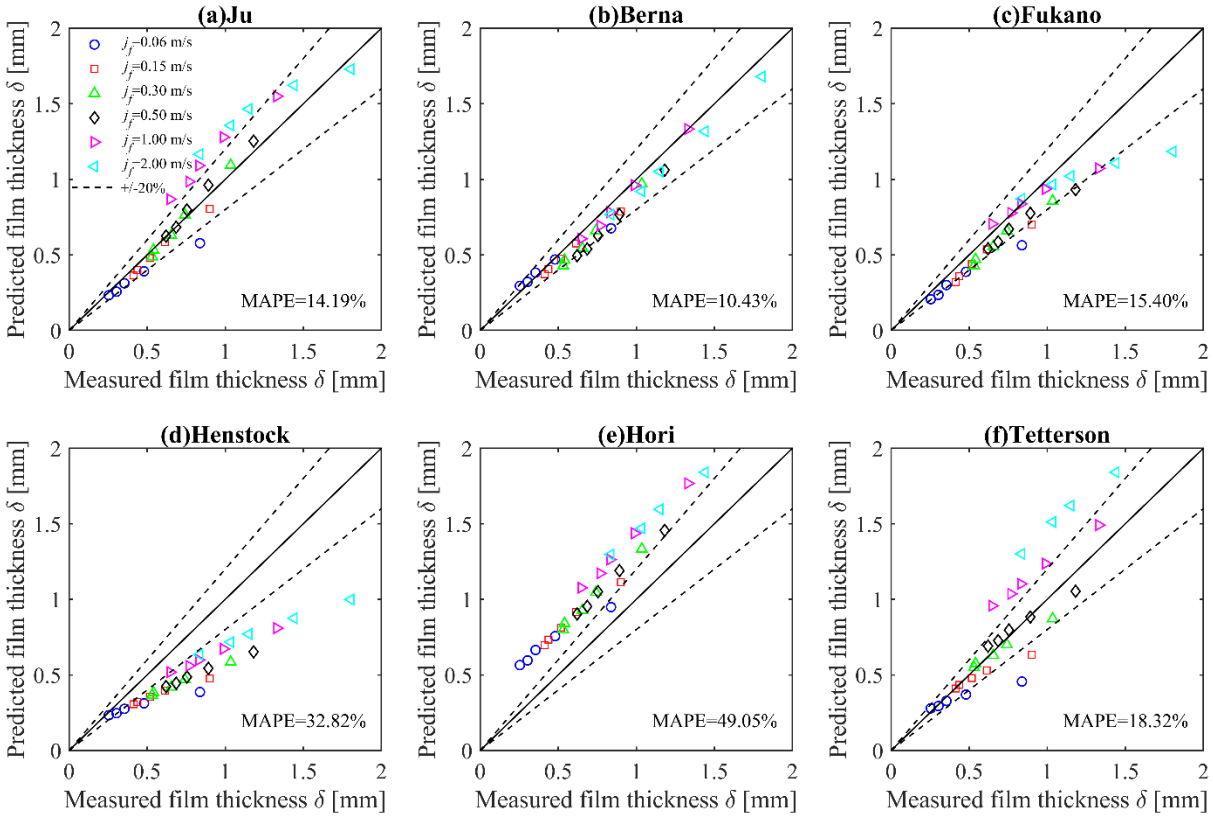

Figure 6-8 Evaluation of various film thickness correlations using the experimental data

6.2.2 Disturbance Wave Height and Base Film Thickness

Disturbance wave height and base film thickness are two parameters to characterize the disturbance wave structure. The base film refers to the liquid layer from the wall to wave trough, which is usually continuous and less disturbed. Unlike average film thickness, there is not a clear mathematical definition for the base film thickness. Because each wave has its trough and peak, and how to average or even define the trough and peak for various waves could be subjective. In this study, an objective way to define the base film thickness is used. Fig. 6-9 shows the probability density function (PDF) of film thickness time trace for a typical annular flow condition. If a less disturbed base film exists, there should be a peak in the PDF at the base film location, as shown in Fig. 6-9. Therefore, in this study, the base film location is obtained through the film thickness PDF peak location.

Fig. 6-10 shows the time trace of film thickness for the flow condition with j_f = 0.061 m/s j_g = 24.24 m/s. The red solid line and red dashed line represents the average film thickness and the base film thickness, respectively, and the identified wave peak is expressed as red circles. The disturbance wave is identified using the MATLAB built-in function 'findpeaks'[94]. The minimum peak distance is set to 0.01 s, which means only the waves with a frequency of less than 100 Hz will be recognized. Belt et al. [95] adopted the same 0.01s deadtime to avoid over counting the merging waves. This is a reasonable assumption because many studies [96], [97] indicate the disturbance wave frequency is much less than 100 Hz for our target flow conditions. Also, the minimum peak height is set to $\delta_{avg}+2\sigma_{film}$, where δ_{avg} is the average film thickness and σ_{film} is the standard deviation of the film thickness time trace. Note that there is no consensus on how to define the minimum disturbance wave height and identify the disturbance wave. Jong and Gabriel [98] and Pan et al. [99] used the threshold of $\delta_{avg}+\sigma_{film}$ as the minimum disturbance wave criterion. Zhao et al. [96] identified the wave with an amplitude larger than 1.6 δ_{avg} as the disturbance wave. Alekseenko et al. [100] assume minimum disturbance wave amplitude to be 1.5 times of base film thickness. To justify the selection of $\delta_{avg}+2\sigma_{film}$ as the minimum disturbance wave peak, Fig. 6-11 compares the performance of different disturbance wave identification criteria. Many waves that are significantly different from the large amplitude disturbance wave are identified as disturbance waves using these three thresholds mentioned above, while the performance of the $\delta_{avg}+2\sigma_{film}$ threshold is good with little misrecognition.

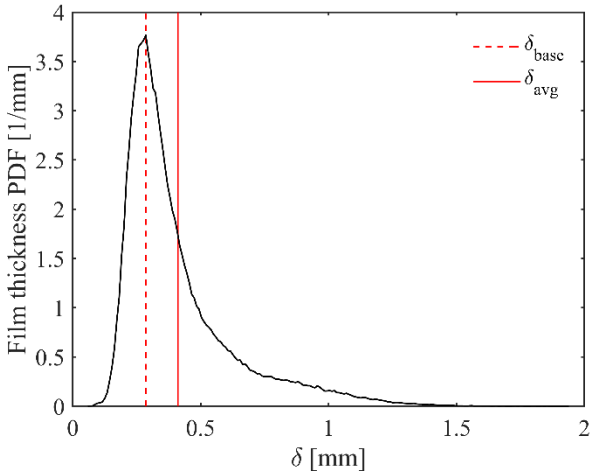

Figure 6-9 Obtaining base film thickness from PDF for a typical annular flow condition

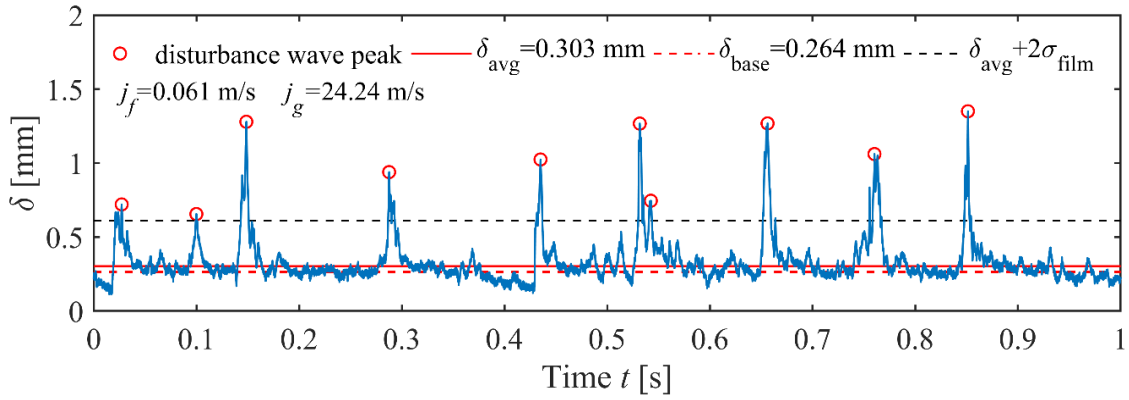

Figure 6-10 Time trace of the local film thickness for j_f = 0.061 m/s j_g = 24.24 m/s

The obtained disturbance wave height is presented in Fig. 6-12. The effect of the inlet conditions on the wave height is similar to the effect on the average film thickness. Increasing the gas flow rate decreases the wave height, and increasing the liquid flow rate increases the wave height. The ratio between the disturbance wave and the average film thickness is shown in Fig. 6-13. The X-axis is the nondimensional average film thickness using pipe diameter. The current data is compared with the wave height data by Belt et al. [95], which is collected in a pipe with a diameter of 0.05 m and shown in Fig. 6-13 as red circles. Each line represents the same superficial gas velocity. The j_f of their data ranges from 0.005 m/s to 0.082 m/s and the j_g ranges from 22 m/s to 42 m/s. Belt et al. [95] data indicate that for a fixed superficial gas velocity, the wave height to film thickness ratio decreases with the film thickness increasing, i.e., superficial liquid velocity increasing. However, this observation is only valid for low liquid flow rate condition, and the current data shows that the wave height to film thickness ratio starts to increase as the film thickness increases. The transition nondimensional film thickness depends on the gas velocity and is approximately within the range from 0.02 to 0.04.

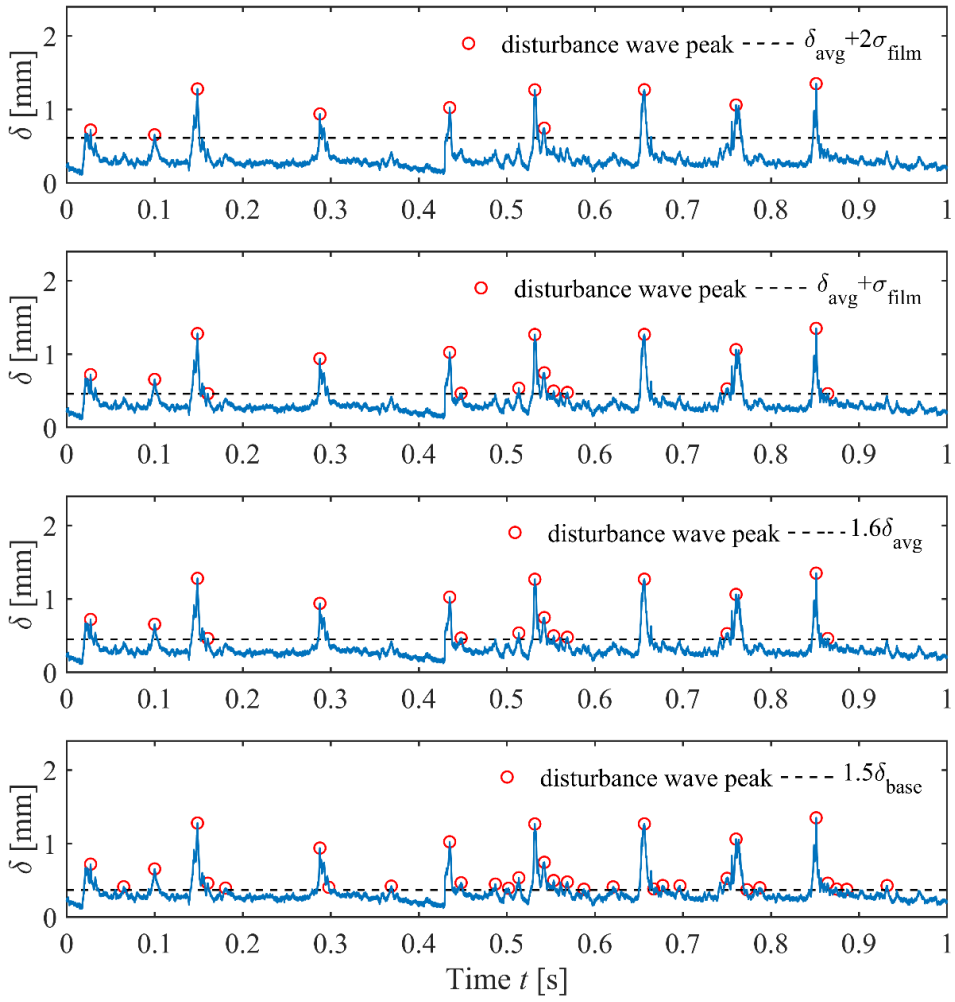

Figure 6-11 Comparison of different disturbance wave identification criteria

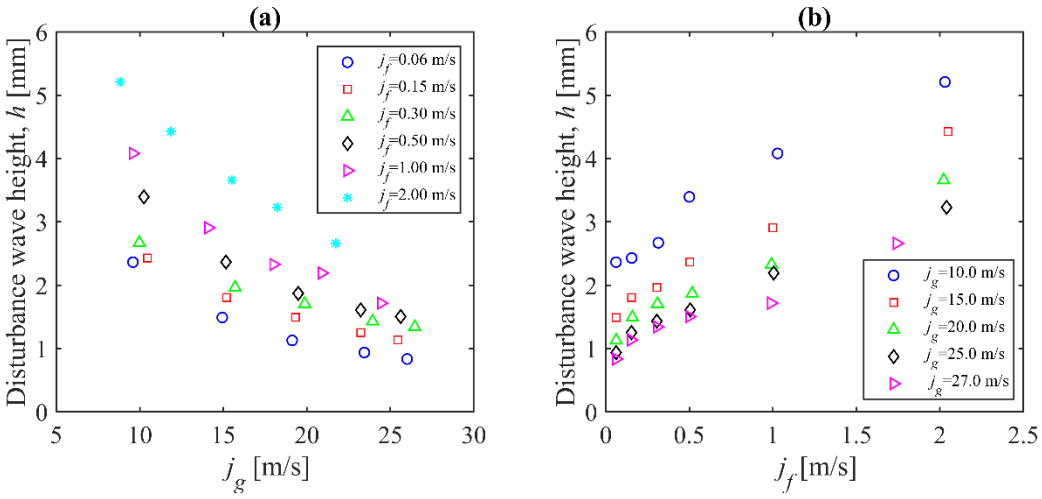

Figure 6-12 Disturbance wave height (a) effect of superficial gas velocity (b) Effect of superficial liquid velocity

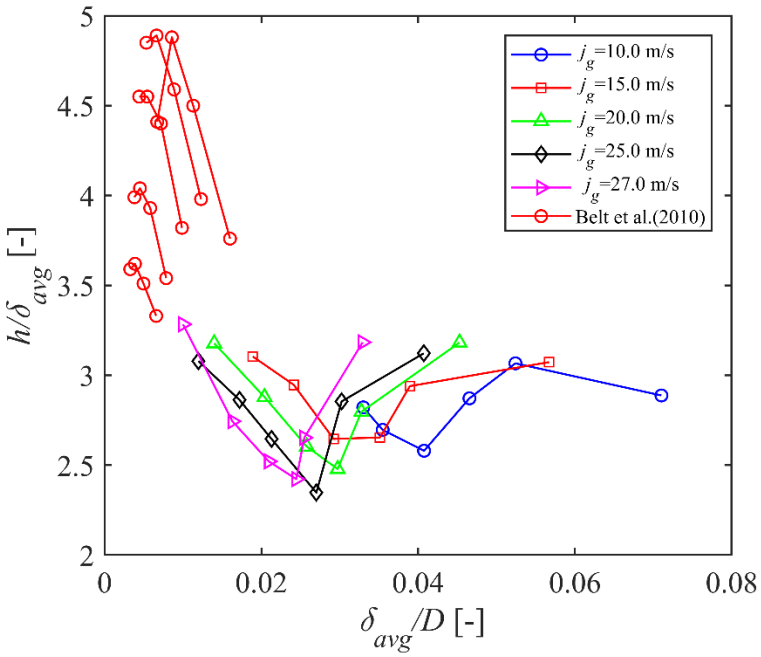

Figure 6-13 Ratio of the disturbance wave height to the average film thickness as a function of the average film thickness

Several wave height correlations are summarized in Table 6-2 with the corresponding prediction error of the current data. The comparison of the experimental data and the model prediction is presented in Fig. 6-14, where the error bar represents ±10%. For the very low j_f (j_f =0.06 m/s),

both the correlations by Han et al. [101] and Ju et al. [102] works well. For the moderate j_f (j_f =0.15-0.50 m/s), the Han model slightly underestimates the wave height while the Ju model slightly overestimates the wave height. For the high j_f (j_f =1.00-2.00 m/s), the Ju model can still predict the data trend with reasonable accuracy. Unlike the Han and Ju models, which are developed based on experimental data, the model by Chandrasekhar [103] is based on Kelvin-Helmholtz instability analysis, and the model by Holowach et al. [104] is developed using the force analysis between the shear stress, surface tension, and film velocity [105]. But their performance in predicting the current data is not as good as the Ju model and the Han model.

Table 6-2 Previous models on disturbance wave height and corresponding error (MAPE) in predicting the current data

Reference	Models	MAPE
Chandrasekhar [103]	$\Delta h = 3\pi \dfrac{\left(1+\dfrac{\rho_g}{\rho_f}\right)\sigma}{\rho_g\left(u_g-u_f\right)^2},\ h=\Delta h+\delta_{base}$	46.41%
Han [101]	$\Delta h = 4000 D\,\mathrm{Re}_g^{-1.12},\ h=\Delta h+\delta_{base}$	22.70%
Holowach [104]	$\Delta h = \dfrac{\sqrt{2}C_W\mu_f}{\left(\rho_g\tau_i f_{fi}\right)^{1/2}},\ h=\Delta h+\delta_{base}$	52.04%
Ju [102]	$\dfrac{h}{D} = 0.24\tanh\left(4.22We_f^{0.16}We_g^{"-0.46}\right)$	11.52%

In addition to the wave height, the correlations for base film thickness is also reviewed and summarized in Table 6-3. The comparison of the prediction of these models and the current data is shown in Fig. 6-15, and corresponding MAPE is listed in Table 6-3. The model by Dobran [106] and Schubring [107] underestimate the base film thickness with the MAPE of more than 40%. The performance of the model by Ju et al. [102] is good and the average error is about 15%.

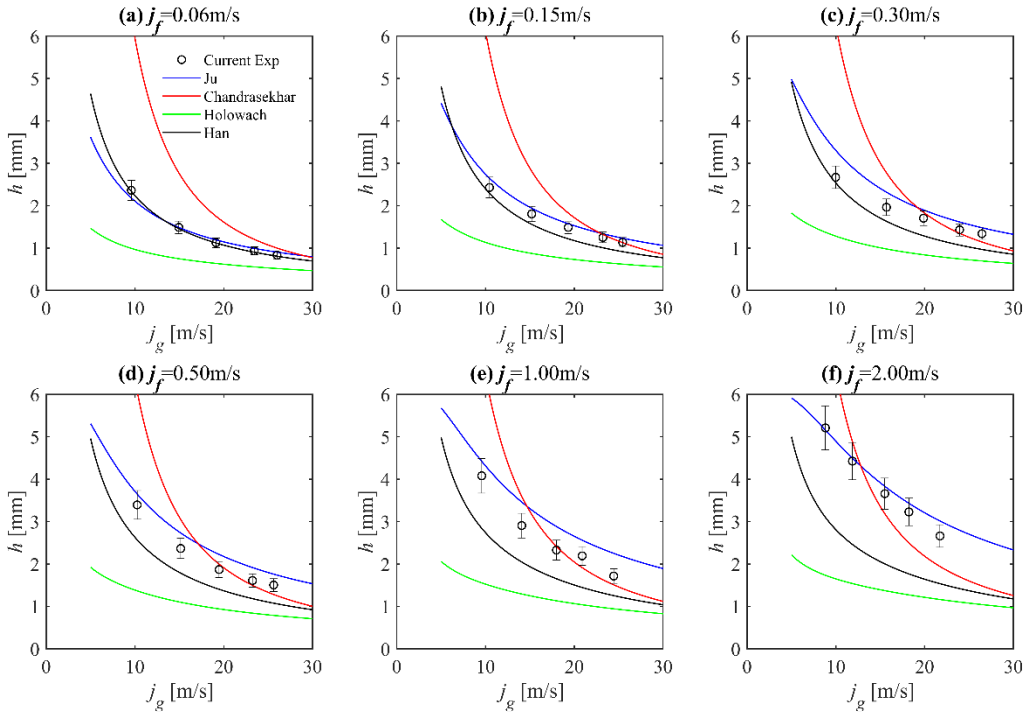

Figure 6-14 Comparison of disturbance wave height with predictions of various correlations

Table 6-3 Previous models on base film thickness and corresponding error (MAPE) in predicting the current data

Reference	Models	MAPE
Dobran [106]	$\delta_{base} = D\left(140 Gr_f^{0.2165}\,\mathrm{Re}_\alpha^{-1.35}\right)$ $Gr_f = \frac{gD^3\rho_f\left(\rho_f-\rho_g\right)}{\mu_f}$, $\mathrm{Re}_\alpha = \frac{j_g\rho_c D}{\mu_g}$ $\rho_c = \alpha_c\rho_g + \left(1-\alpha_c\right)\rho_f$ α_c is void fraction is gas core	58.79%
Ju [102]	$\frac{\delta_{base}}{D} = 0.04\tanh\left(4.31 We_f^{0.22} We_g^{"-0.44}\right)$	15.30%
Schubring [107]	$\delta_{base} = 4.8 D \mathrm{Re}_g^{-0.6}$	43.98%

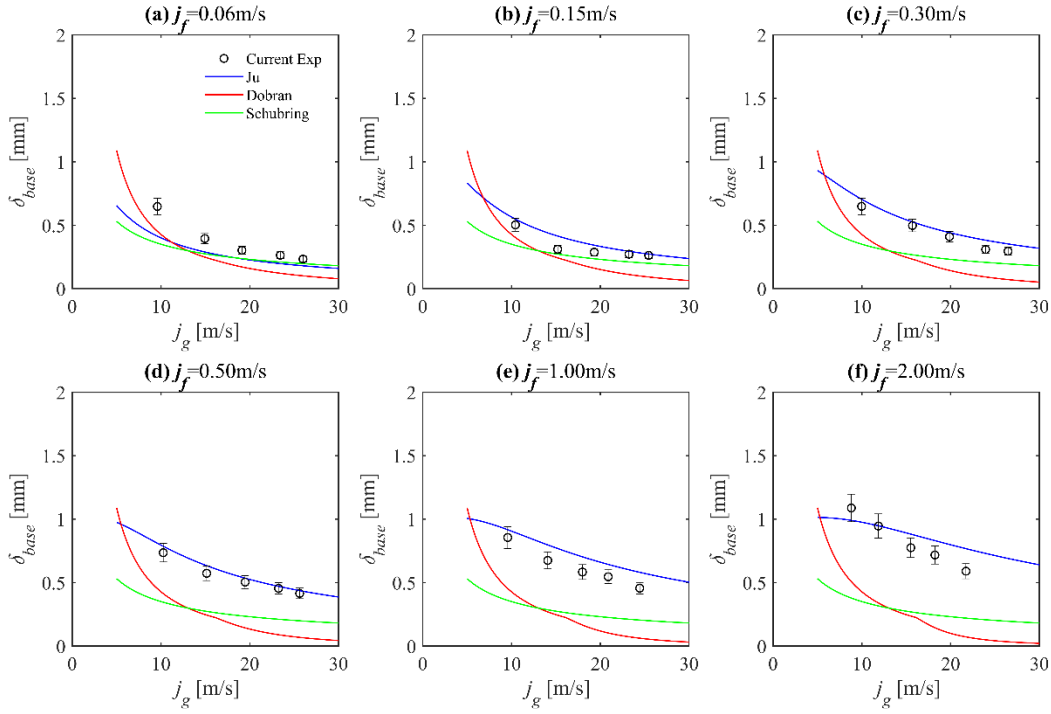

Figure 6-15 Comparison of base film thickness with predictions of various correlations

6.2.3 Wave Velocity

As mentioned in section 6.1.2, the wave velocity can be measured using two film thickness probes along the flow direction and quantifying the time lag between the two signals by cross-correlation. To get a reliable wave velocity measurement, the sampling time step (reciprocal of sampling frequency) should be much less than the time required for a wave traveling through two probes. The maximum relative truncation error for the velocity can be expressed as:

$$err_{\max} = \frac{v_{\max} - v}{v} = \frac{\dfrac{s}{s/v - 1/f} - v}{v} = \frac{v}{sf - v} \tag{6.4}$$

Where v is the velocity, s is the distance between to probes, and f is the sampling frequency. Fig. 6-16 shows the maximum relative truncation error calculated by Eq. (6.4). When measuring the wave with a velocity of 30 m/s, the error of using the 10 kHz sampling frequency can be more than 40%. If increasing the frequency to 50 kHz, the error reduces to less than 7%. It is worthy to mention that the error presented in Fig. 6-16 is the maximum truncation error, the actual uncertainty of velocity measurement due to the discontinuous sampling should be less. Therefore,

the sampling frequency of 50 kHz used in this study should be high enough to get a reliable wave velocity measurement.

The wave velocity for various flow conditions is presented in Fig. 6-17, which shows an increasing trend of wave velocity with both j_g and j_f as expected. When j_f is less than 1.0 m/s, the wave velocity increases slightly with the increasing j_g, its value is much lower than j_g. For the conditions with j_f of 1.0 and 2.0 m/s, the wave velocity is close to or larger than the local superficial gas velocity. The reason for the significantly increasing wave velocity when j_f increases from 0.5 to 1.0 m/s should be the transition from annular flow to wispy annular flow. In typical annular flow, the interface between the liquid film and the gas core is smoother and more stable than that in wispy annular flow. Therefore, the interfacial shear is much less, and the momentum of the gas and liquid phases are less coupled. As a result, the liquid wave could travel at a low velocity while the gas core is at a much higher speed. But in wispy annular flow, the film structure is more complicated, liquid ligaments connected to the film as well as liquid wisps could exist in the gas core. Therefore, the momentum transfer between the gas and liquid phase would be much more significant, and the wave velocity should be at the same order of magnitude to the gas velocity.

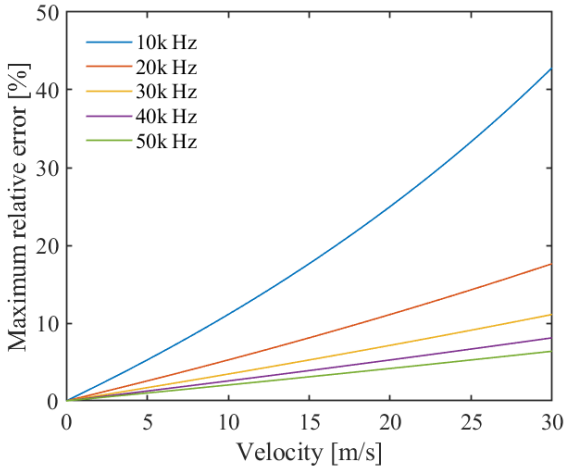

Figure 6-16 Sampling Frequency Effect on Wave Velocity Measurement

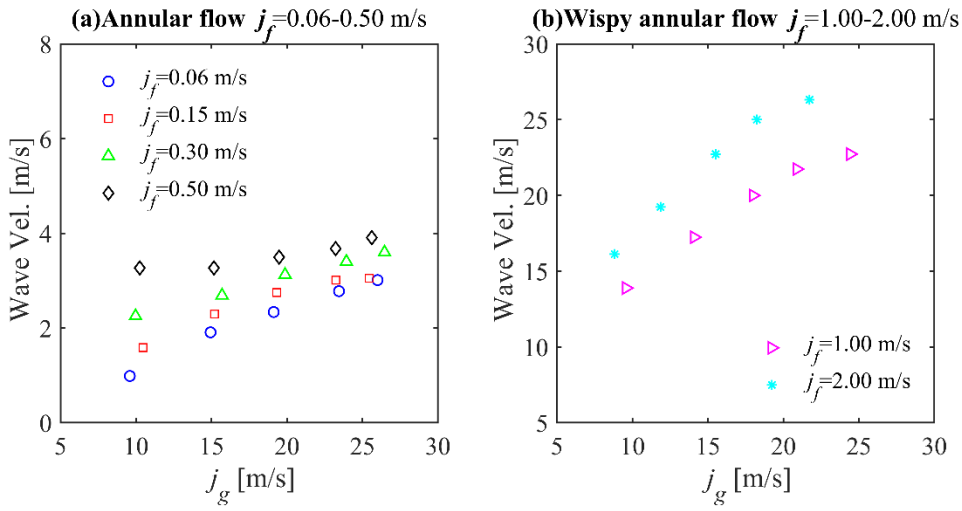

Figure 6-17 Wave Velocity Measurement Results (a) j_f = 0.06-0.50 m/s (b) j_f = 1.00-2.00 m/s

Several previous wave velocity correlations are evaluated using the current data, and the formulation of these correlations and the evaluation results are shown in Table 6-4 and Fig. 6-18. In view of the significant wave velocity difference between the annular flow conditions (j_f = 0.06-0.50 m/s) and the wispy annular flow (j_f = 1.00-2.00 m/s) conditions, the evaluation is performed separately for these two flow regimes. The annular flow results are shown in Fig. 6-18(a), the models by Berna et al. [89], Ju et al. [102], and Kumar et al. [108] have relatively good performance with the prediction error of less than 20% for most annular flow conditions. The Ju model slightly overestimates the wave velocity, while the Kumar model underestimates the wave velocity a little. The Berna model has the least MAPE, which is 15.99%. Overall, the wave velocity data for typical annular flow conditions (j_f = 0.06-0.50 m/s) can be well predicted by several previous correlations. However, for the wispy annular flow conditions, all previous correlations significantly underestimate the wave velocity. This is because all these models were developed for typical annular flow, and few data are available to characterize the wispy annular flow structure and wave velocity.

Table 6-4 Previous models on wave velocity and corresponding error (MAPE) in predicting the current data

Reference	Models	MAPE for annular flow (j_f = 0.06-0.50 m/s)	MAPE for wispy annular flow (j_f = 1.00-2.00 m/s)
Al-Sarkhi et al.[109]	$v_w = 1.942 X^{-0.91} j_f$ $X = \sqrt{\frac{\rho_f j_f^2}{\rho_g j_g^2}}$	58.77%	94.23%
Berna et al.[89]	$\frac{v_w}{\frac{\sqrt{\rho_f} j_f + \sqrt{\rho_g} j_g}{\sqrt{\rho_f} + \sqrt{\rho_g}}} = 50 \mathrm{Re}_g^{-0.38} \mathrm{Re}_f^{0.16} C_W^{-0.13}$ C_W is surface tension factor defined by Ishii and Grolmes [105] as $C_W = 0.028 N_{\mu f}^{-4/5}$ for $N_{\mu f} \le 1/15$ $C_W = 0.25$ for $N_{\mu f} > 1/15$	15.99%	51.70%
Ju et al. [102]	$v_w = 10.1 j_f We_f^{-0.392} We_g^{"0.227}$	20.41%	77.24%
Kumar et al. [108]	$v_w = \frac{\psi j_g + j_f}{1+\psi}$ $\psi = 5.5 \sqrt{\frac{\rho_g}{\rho_f}} \left(\frac{\mathrm{Re}_f}{\mathrm{Re}_g} \right)^{0.25}$	18.19%	80.39%
Marmottant and Villermaux [110]	$v_w = \frac{\sqrt{\rho_f} j_f + \sqrt{\rho_g} j_g}{\sqrt{\rho_f} + \sqrt{\rho_g}}$	68.57%	90.19%
Schubring and Shedd [111]	$v_w = 0.42 \frac{j_g}{\sqrt{x}} \mathrm{Re}_G^{-0.25}$	31.11%	77.87%

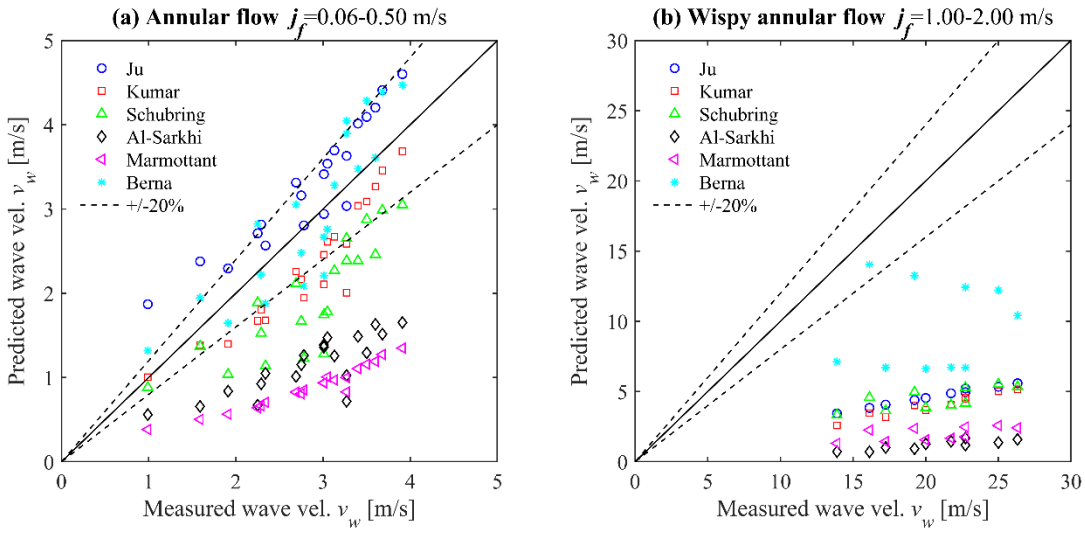

Figure 6-18 Comparison of measured wave velocity with various wave velocity correlations

The wave velocity is nondimensionalized using the superficial liquid velocity and plotted against the Lockhart-Martinelli parameter in Fig. 6-19. The data can be well collapsed into a line for various flow conditions. However, the trend line for the wispy annular flow conditions is quite different from the typical annular flow conditions, which is the reason that the previous model fails. To address this issue, a correlation for the wave velocity in wispy annular flow is proposed based on current data, which is

$$\frac{v_{w,wispy}}{j_f} = 25.95X^{-0.62} \tag{6.5}$$

Where $v_{w,wispy}$ is the wave velocity for wispy annular flow, and X is the Lockhart-Martinelli parameter:

$$X = \sqrt{\frac{\rho_f j_f^2}{\rho_g j_g^2}} \tag{6.6}$$

The MAPE of Eq. (6.5) in predicting the wave velocity of the wispy annular flow conditions (j_f = 1.00-2.00 m/s) is 2.67%. It should be noted that Eq. (6.5) is just a preliminary correlation, and its application range should be limited by the current data (Re_f 3×10^4~6×10^4, Re_g 1.5×10^4~5×10^4). The wave velocity maybe also influenced by the channel size and fluid physical properties other than density. However, since few datasets are available at wispy annular flow, it is infeasible to develop a comprehensive wave velocity model for wispy annular flow that works for a wide range of parameters at the present stage.

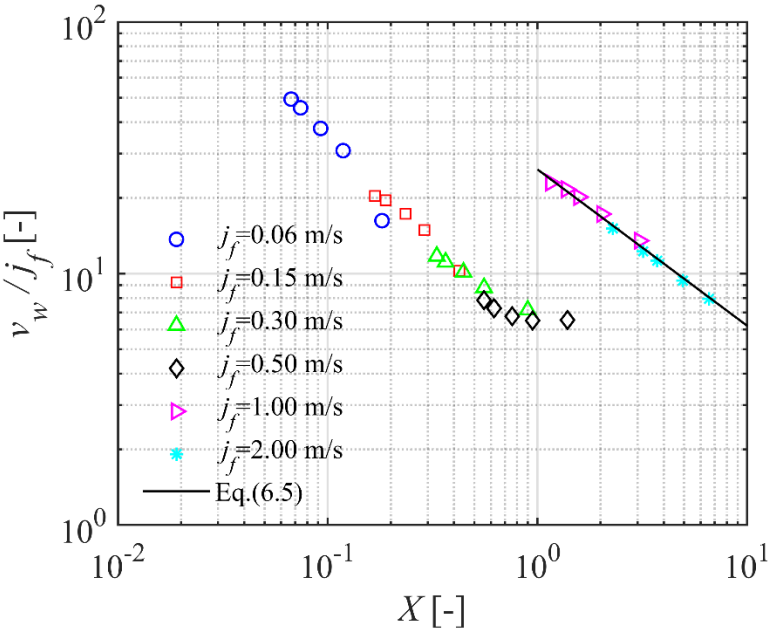

Figure 6-19 Nondimensional wave velocity versus Lockhart-Martinelli parameter

6.2.4 Disturbance Wave Frequency

Usually, two methods are used to determine the disturbance wave frequency: power spectral density (PSD) analysis and directly counting. Power spectral density analysis gives the predominant frequency of the time trace, which is considered as the disturbance wave frequency. Directly counting is achieved by identifying the disturbance wave peaks, as discussed in 6.2.2, and dividing the peaks counting by sampling time to get the frequency. Fig. 6-20 shows the comparison of the wave frequency obtained by PSD and direct counting. For most flow conditions the error between these two methods is less than 20%. However, for the very low j_f (j_f = 0.06 m/s), the wave frequency by PSD is much less than the frequency by direct counting, especially for high gas flow rate conditions. This phenomenon is also observed by Zhao et al. [96]. They explained that the PSD method may not be able to differentiate the disturbance wave from other waves, especially when the frequency of the disturbance wave is relatively low. Therefore, the wave frequency obtained by direct counting is used for the following analysis and model evaluation.

Fig. 6-21 presents the wave frequency obtained by direct counting. The wave frequency increase with the superficial gas velocity, although this trend becomes less obvious for wispy annular flow

conditions. The effect of the superficial liquid velocity is more complicated. At low j_f, the wave frequency increases with the j_f. When j_f reaches 0.2~0.3 m/s, roughly corresponding to Re_f of 6000~8000, the wave frequency reaches a maximum value and further increase of j_f leads to reduced wave frequency. This trend can also be found in the work by Hazuku et al. [112] (Fig. 12 and 13), although their focus is the wave axial development and they did not mention this trend. The time traces of film thickness measurement for flow conditions with the same j_g but increasing j_f are shown in Fig. 6-22. As the j_f increases from 0.06 m/s to 0.15 m/s, the wave frequency increases, while the maximum wave amplitude does not change obviously. With the j_f increases from 0.15 m/s to 0.31 m/s, the wave amplitude becomes higher while there is no further obvious increase of the wave frequency. Further increasing j_f from 0.31 m/s to 1.01 m/s leads to the wave frequency declining and the wavelength enlarging. At the highest superficial liquid velocity (j_f = 2.04 m/s), although the wave frequency is similar to the low liquid velocity conditions, the maximum wave amplitude reaches 5 mm, about 4 times larger than the lowest superficial liquid velocity (j_f = 0.06 m/s)

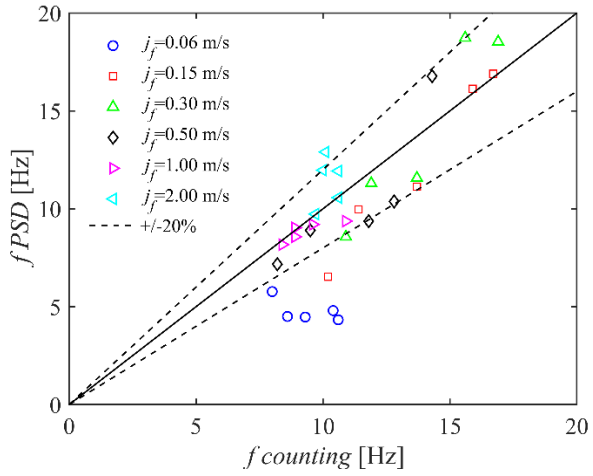

Figure 6-20 Comparison of wave frequency obtained by direct counting and PSD

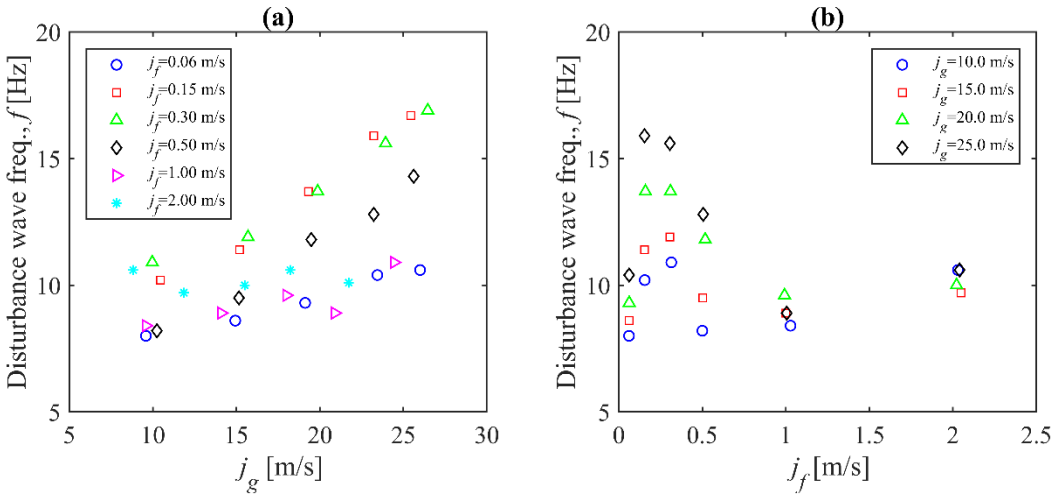

Figure 6-21 Wave frequency obtained by direct counting (a) j_g effect (b) j_f effect

Table 6-5 summarizes the previous wave frequency correlations. Strouhal number is often used to scale the frequency, which is defined as:

$$Sr = \frac{fD}{v} \tag{6.7}$$

where f is the frequency, D is the characteristic length, and v is the characteristic velocity. All models listed in Table 6-5 used Strouhal number, although some use superficial liquid velocity as characteristic velocity [113], [114] and some use superficial gas velocity as characteristic velocity [97], [115]. The evaluation results and corresponding MAPE are presented in Fig. 6-23 and Table 6-5. The model by Alamu and Azzopardi [113] has the least error of 20.59% in predicting the current data.

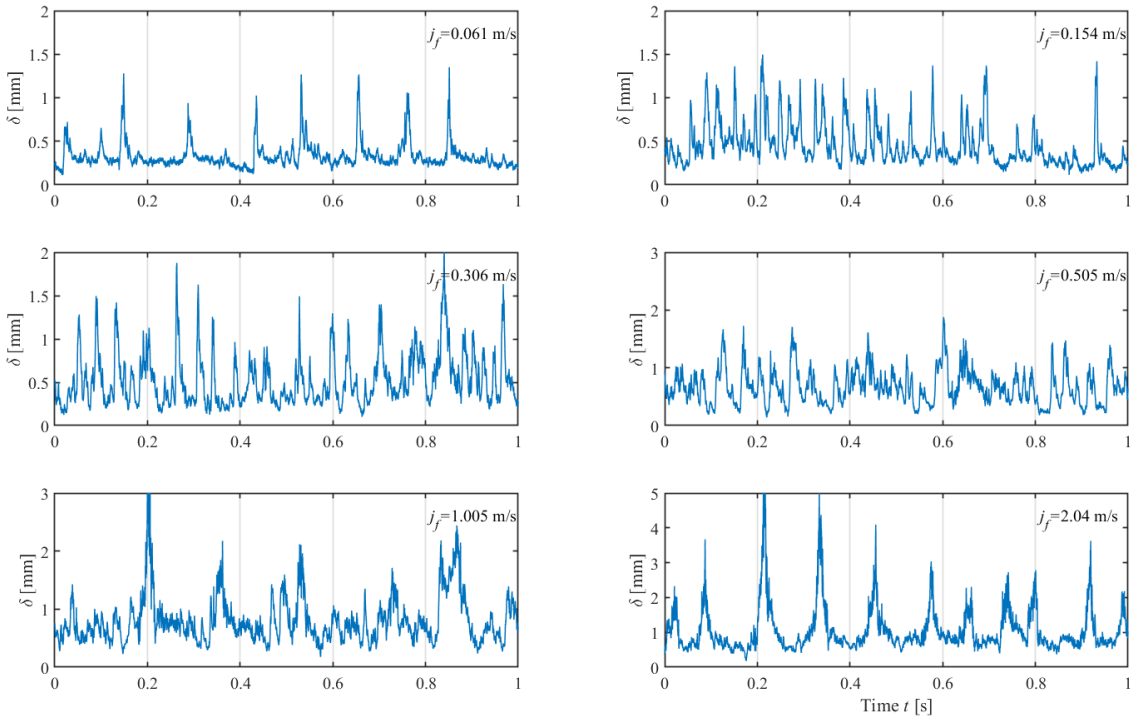

Figure 6-22 Time trace of film thickness signal for flow conditions with j_g = 25 m/s

Table 6-5 Previous models on wave frequency and corresponding error (MAPE) in predicting the current data

Reference	Models	MAPE
Alamu and Azzopardi [113]	$Sr_f = \frac{fD}{j_f} = 0.4292X^{-0.908}$	20.59%
Azzopardi [114]	$Sr_f = \frac{fD}{j_f} = 0.25X^{-1.2}$	42.39%
Sawant et al. [97]	$Sr_g = \frac{fD}{j_g} = 0.086\mathrm{Re}_f^{0.27}\left(\frac{\rho_f}{\rho_g}\right)^{-0.64}$	32.16%
Sekoguchi et al.[115]	$Sr_g = \frac{fD}{j_g} = f_1(Eo)\,g_1(\xi)$ $f_1(Eo) = Eo^{-0.5}\left(0.5\ln(Eo) - 0.47\right)$ $g_1(\xi) = 0.0076\ln\xi - 0.051$ $Eo = \frac{gD^2(\rho_f - \rho_g)}{\sigma}$, $\xi = \frac{\mathrm{Re}_f^{2.5}}{Fr_g}$, $\mathrm{Fr}_g = \frac{j_g}{\sqrt{gD}}$	29.71%

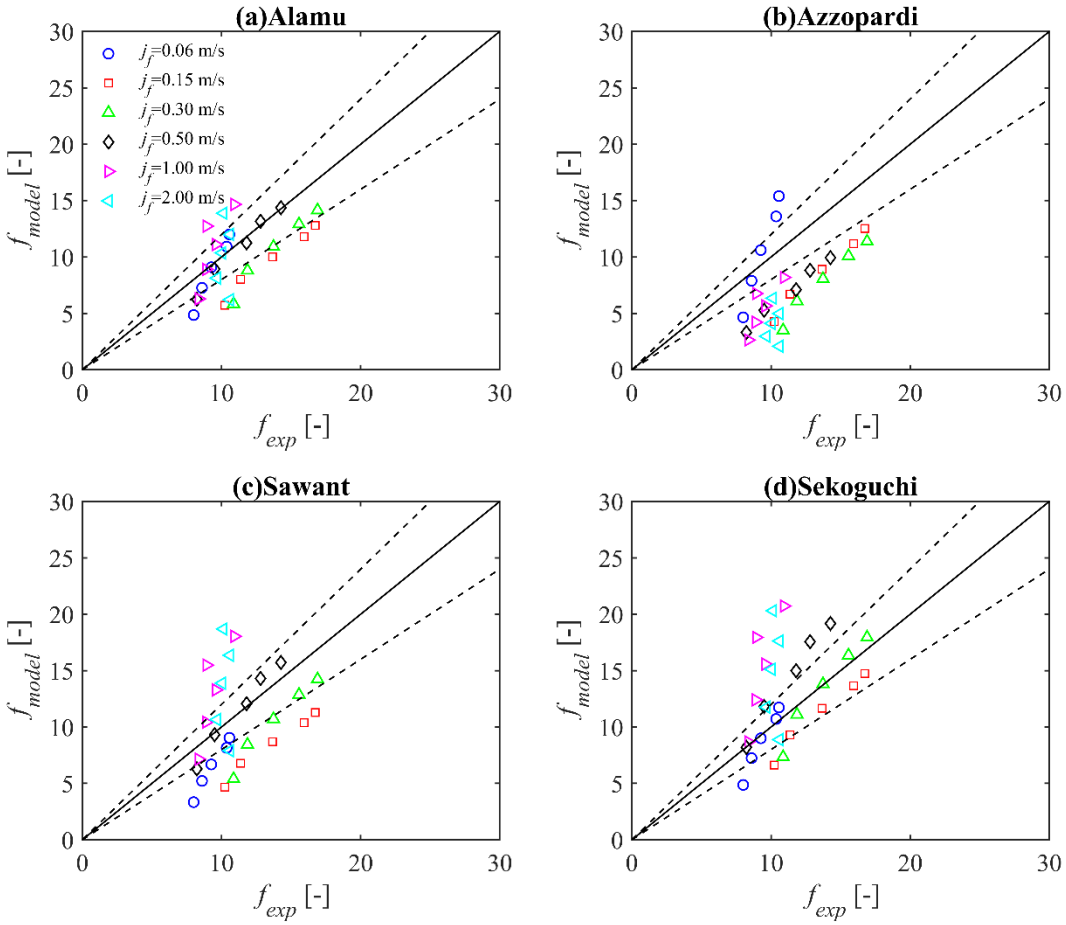

Figure 6-23 Comparison of measured wave frequency with various models

6.2.5 Interfacial Shear

The pressure gradient is calculated using the pressure measured at z/D_h = 78 and 141, which is presented in Fig. 6-24. For the flow conditions with j_f of 0.06 m/s and 0.15 m/s, the pressure gradient initially decreases with the superficial gas velocity, and then increases. This is because of the effect of liquid flow reversal. It is observed during the experiment that the liquid film intermittently stagnates or reverses for the flow conditions with j_g of 10 m/s, while this intermittent flow reversal disappears for 15 m/s superficial gas velocity condition. This kind of data trend is also reported by Owen [116], [117] and Liu [40]. In the Owen data, the pressure gradient trend transition happens at the dimensionless gas velocity of 1, corresponding to a j_g of 14.36 m/s for the

current test. This agrees with the current data. As the gas velocity increases further, the pressure gradient rises due to the increment of the relative velocity and the greater interfacial shear.

For equilibrium annular flow, the interfacial shear stress can be expressed as

$$\tau_i = -\frac{A_c}{P_c}\left[\frac{dp}{dz}\left(1-\frac{\rho_c v_g^2}{p}\right)+\rho_c g\right] - R_{d/e}\left(v_d - v_e\right) \tag{6.8}$$

On the right-hand side, the four terms are total pressure term, expansion term, gravity term, and entrainment/deposition term. A_c and P_c is the area and perimeter of the gas core, ρ_c is the average gas core density including the gas phase and the entrained droplet phase, $R_{d/e}$ is the entrainment or deposition rate, which are equal because of equilibrium condition, and v_d, v_e is the velocity of the deposited droplets and entrained droplets. The entrainment fraction model by Ishii and Mishima [118] is used to calculate the gas core density and the entrainment rate is estimated using the model by Wang et al. [119]. Since the gas flow rate for the current data is not very high, both the entrainment fraction and the entrainment rate are small and have little contribution to the interfacial shear. As a result, the interfacial shear can be roughly expressed as:

$$\tau_i = \frac{D-2\delta_{avg}}{4}\frac{dp}{dz} \tag{6.9}$$

The interfacial shear calculated using Eq. (6.8) and (6.9) are compared in Fig. 6-25. The maximum percentage deviation is 5.97% and the average deviation is 2.43%. Therefore, the contributions of various terms in Eq. (6.8) other than the total pressure drop term is negligible for the current flow conditions, which can rule out the effect of entrainment model selection.

The interfacial shear factor in annular flow is typically defined as [120]:

$$f_i = \frac{2\tau_i}{\rho_g v_g^2} \tag{6.10}$$

and the gas velocity can be estimated using:

$$v_g = \frac{j_g}{\alpha} = \frac{j_g D^2}{\left(D-2\delta_{avg}\right)^2} \tag{6.11}$$

The interfacial shear factor is calculated using the measured pressure drop and compared with several correlations, which are listed in Table 6-6. The evaluation result is presented in Fig. 6-26. Among these models, the model by Ju et al. [102] has the least prediction error (18.66%). The

Wallis model [1] can predict the interfacial shear factor for low liquid flow rate conditions but significantly underestimate the interfacial shear factor for high liquid flow rate conditions.

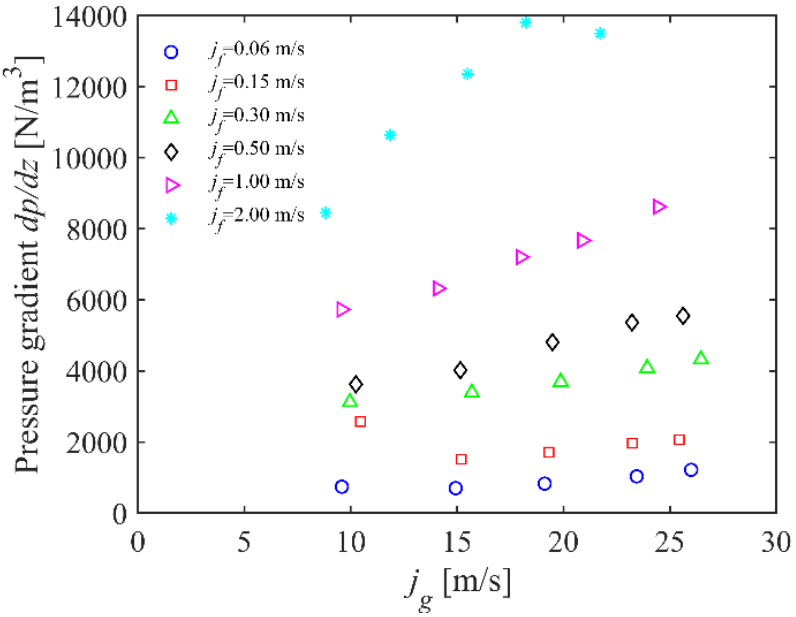

Figure 6-24 Average pressure gradient from z/D_h = 78 to 141

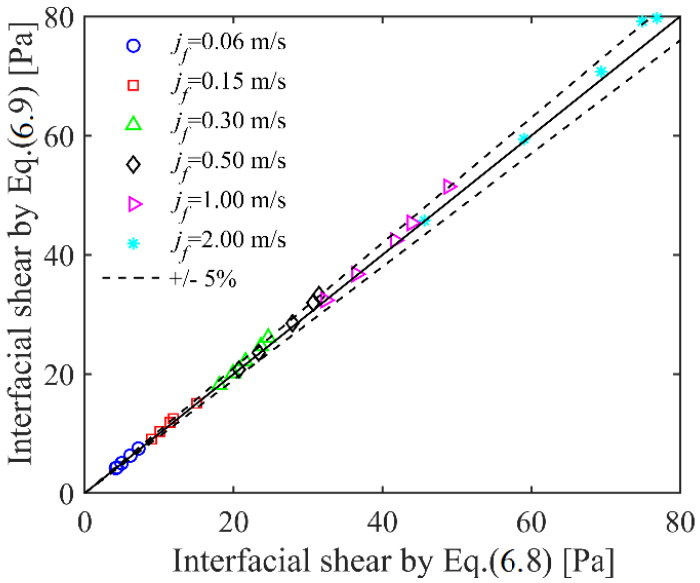

Figure 6-25 Comparison of interfacial shear stress calculated using Eq. (6.8) and (6.9)

Table 6-6 Models of interfacial shear factor and corresponding error (MAPE) in predicting the current data

Reference	Models	MAPE
Belt et al.[121]	$f_i = 2\left(1.158\frac{\delta}{D} + 3.413\times10^{-4}\right)$	41.45%
Ju et al. [102]	$f_i = 0.0028 + 4.28We_f^{0.28}We_g^{"-0.53}N_{\mu f}^{0.25}$	18.66%
Pan et al. [99]	$f_i = 67.2\mathrm{Re}_g^{-0.91}\mathrm{Re}_f^{0.30}$	47.59%
Wallis [1]	$f_i = 0.005\left(1+300\frac{\delta}{D}\right)$	45.86%

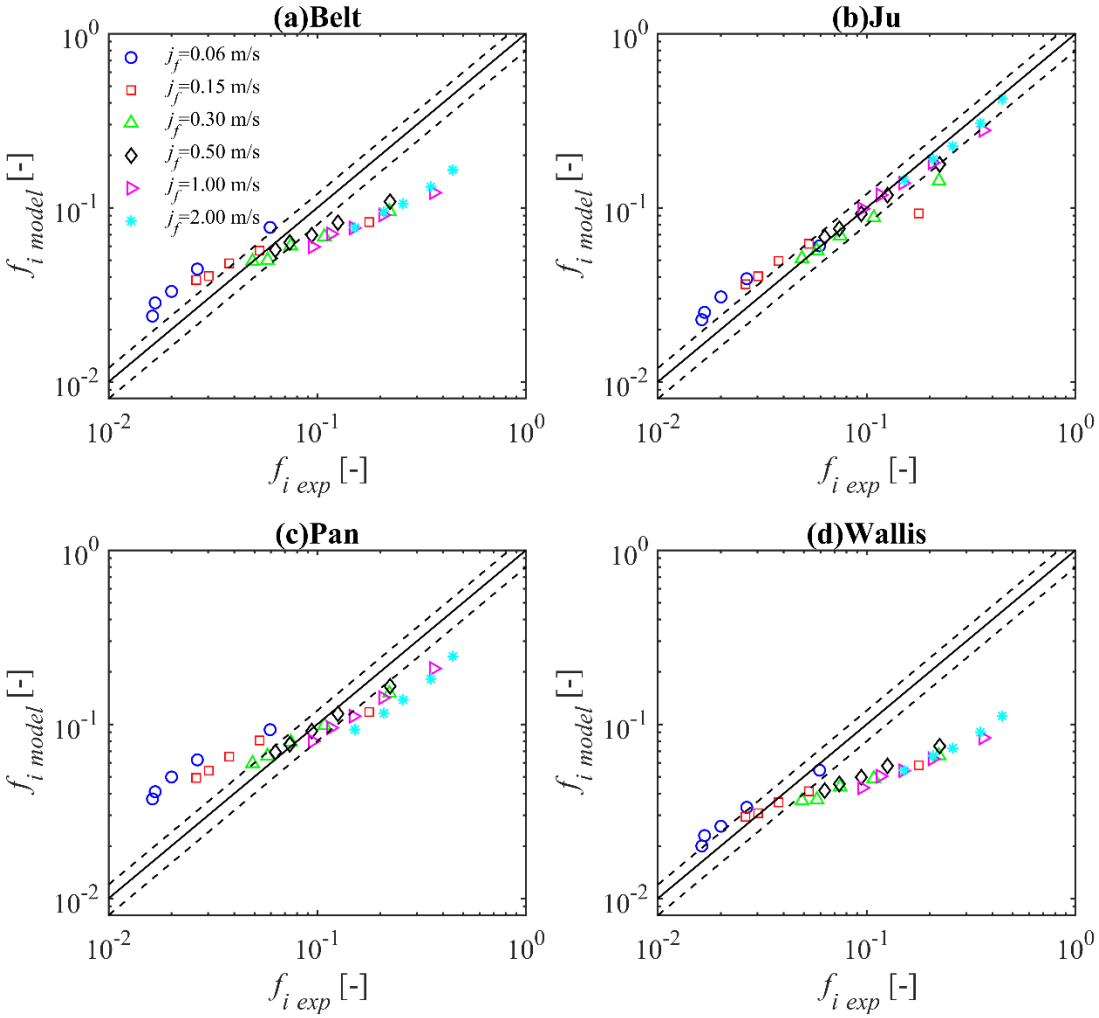

Figure 6-26 Comparison of the measured interfacial shear factor with various models

7. ANNULAR FLOW INTERFACIAL AREA TRANSPORT

7.1 Challenges in Interface Modeling in Annular flow

In annular flow, the interface between the gas core and liquid film may not be well predicted by IATE, because IATE is derived based on the particle (bubble/droplet) dynamic analysis, while the gas core-liquid film interface is characterized by the relative motion of two continuous phases. Therefore, a constitutive model for annular flow IAC is required to have a comprehensive IAC prediction capability for all flow regimes. Hazuku et al. [122] obtained the area-averaged IAC by film thickness measurement and compared the data with a simple correlation obtained by smooth liquid film assumption. It was found that the area-averaged IAC can be well predicted even if the liquid film fluctuation effect is neglected. However, the smooth interface assumption is incompatible with a 3-D two-fluid model. As schematically shown in Fig. 7-1 (a), assuming an interface does not change with time results in a singularity of the local interfacial area concentration (IAC). To address this issue, the liquid film fluctuation should be considered. If taking the average over a short time, like the two-fluid model derivation, the liquid film IAC should become a wall peaked function instead of a singularity, as shown in Fig. 7-1 (b). Therefore, the target of this study is to develop a constitutive model for the IAC radial distribution in annular flow. This model can work with the IATE and form a comprehensive interfacial area predictor for 3-D two-fluid model.

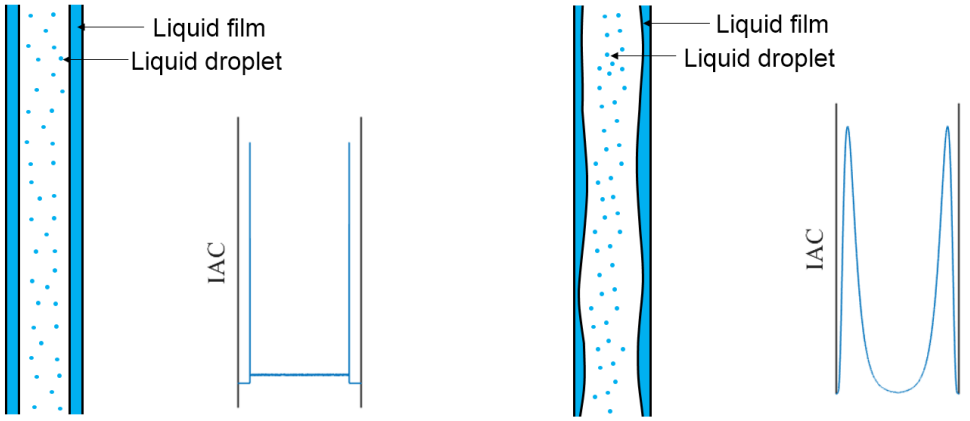

(a) smooth liquid film (b) fluctuating liquid film

Figure 7-1 Annular flow structure and corresponding IAC profile

7.2 Annular Flow IAC Measurement

As mentioned in section 5.3.3, if we assume the interface between the gas core and the liquid film travels at a uniform velocity, the time trace of the film thickness measurement can be converted to the actual interfacial structure, and the radial distribution of time-averaged IAC can be obtained. To evaluate the accuracy of IAC measurement using the film thickness probe, the flow structure is measured using flow visualization. The schematic of the flow visualization for interfacial structure measurements is shown in Fig. 7-2. To compensate for the distortion effect of the round pipe, a square box filled with water is used. Given that the refractive index of water is close to that of acrylic, the difference between the actual interface structure and the measured structure is small. To determine the camera focusing length, a thin plate with a scale on it is placed on the center of the box, as shown in Fig. 7-2. LED light is placed on the opposite side of the tube. By benchmarking with the scale, each pixel corresponds to 0.02 mm.

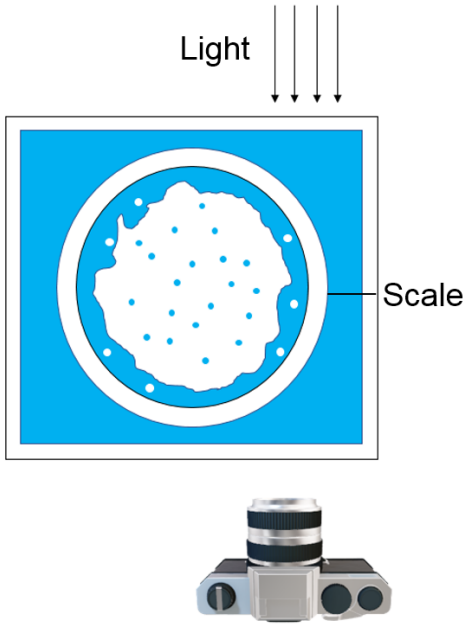

Figure 7-2 Schematic of flow visualization for interfacial structure measurement

A sample image captured using this method is presented in Fig. 7-3. The interface between liquid film and the gas core is clear and can be easily identified using the image processing method. The identified interface is shown as a blue line in Fig. 7-3. With the measured interfacial structure, the IAC radial distribution can be obtained using the same approach discussed in section 5.3.3. The comparison of IAC profiles measured by flow visualization and a film thickness probe is presented

in Fig. 7-4. Two subplots Fig. 7-4 (a) and (b) represent low gas velocity conditions and high gas velocity, respectively. The IAC profile obtained by the film thickness probe agrees well with the IAC profile obtained by flow visualization. Therefore, the capability of using a time trace of film thickness measurement to get an IAC radial distribution is verified, and the IAC profiles can be obtained using the film thickness result presented in Chapter 6.

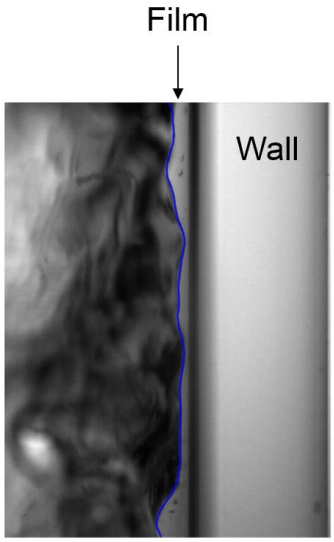

Figure 7-3 Sample image (j_f=0.05 m/s j_g=10.03 m/s) and identified interface boundary using image processing

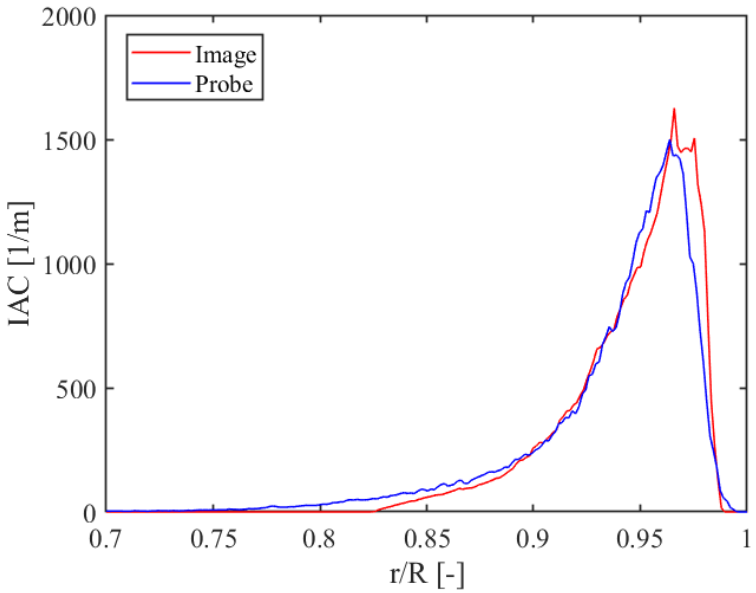

(a) j_f=0.05 m/s j_g=10.03 m/s

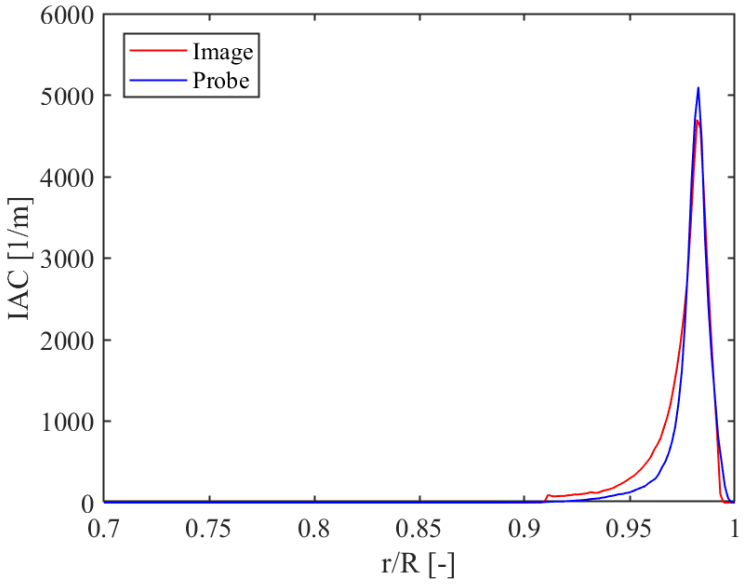

(b) j_f=0.06 m/s j_g=26.07 m/s

Figure 7-4 Comparison of IAC profiles measured by flow visualization and film probe

7.3 Annular Flow IAC Model Development

In this section, a constitutive model that can predict the IAC radial distribution will be developed. By observing the measured IAC profiles, it is assumed that the IAC profile can be modeled as the log-normal distribution, as shown in Fig. 7-5. Then the IAC radial distribution can be formulated as:

$$a_i(r) = \frac{k}{r\sigma\sqrt{2\pi}} e^{-(\ln r-\mu)^2/2\sigma^2} \tag{7.1}$$

where r is the nondimensional radial location, k, μ, and σ are the mathematical parameters that determine the amplitude, location, and shape of this distribution. The key to this model is connecting these mathematical parameters to the flow characteristics using proper closure relations. Therefore, three assumptions are made to find these parameters:

(1) IAC profile peaks at the base film location

$$d_{peak} = \delta_{base} \tag{7.2}$$

(2) Area average IAC can be calculated using the smooth film assumption

$$\langle a_i \rangle = \frac{\int a_i(r)dA}{\pi D^2/4} = 4\frac{D-2\delta_{avg}}{D^2} \tag{7.3}$$

(3) Full Width at Half Maximum (FWHM) of the profile equals to the average film thickness

$$FWHM = \delta_{avg} \tag{7.4}$$

The peak location and FWHM are also presented in Fig. 7-5. Given that the IAC profile is assumed to follow a log-normal distribution, Eq. (7.2)-(7.4) can be expressed as:

$$e^{\left(\mu-\sigma^2\right)} = \delta_{base} \tag{7.5}$$

$$2k\left(1-e^{(\mu+\sigma^2/2)}\right) = 4\frac{D-2\delta_{avg}}{D^2} \tag{7.6}$$

$$e^{(\mu-\sigma^2)+\sqrt{2\sigma^2\ln 2}} - e^{(\mu-\sigma^2)-\sqrt{2\sigma^2\ln 2}} = \delta_{avg} \tag{7.7}$$

Therefore, if the base film and average film thicknesses are known, the distribution parameter k, μ, and σ can be calculated using Eq. (7.5)-(7.7). The constitutive models by Ju et al. [88], [102] are selected for the film thickness:

$$\frac{\delta_{avg}}{D} = 0.06\tanh\left(14.22We_f^{0.24}We_g^{"-0.47}N_{\mu f}^{0.21}\right) \tag{7.8}$$

$$\frac{\delta_{base}}{D} = 0.04\tanh\left(4.31We_f^{0.22}We_g^{"-0.44}\right) \tag{7.9}$$

where We_f, $We_g^{"}$, and $N_{\mu f}$ is liquid Weber number, gas Weber number, and viscosity number, respectively, which are defined as:

$$We_f = \frac{\rho_f\left\langle j_f\right\rangle^2 D}{\sigma_s} \tag{7.10}$$

$$We_g^{"} = \frac{\rho_g\left\langle j_g\right\rangle^2 D}{\sigma_s}\left(\frac{\Delta\rho}{\rho_g}\right)^{1/4} \tag{7.11}$$

$$N_{\mu_f} = \frac{\mu_f}{\sqrt{\rho_f\sigma_s\sqrt{\frac{\sigma_s}{g\Delta\rho}}}} \tag{7.12}$$

Since the constitutive model for film thickness only depends on the flow conditions and the fluid properties, the IAC profile can be obtained using Eq. (7.5)-(7.9) if the fluid type and flow conditions are known. The comparison of the predicted IAC profile using this new model and the IAC data measured by the film thickness probe is presented in Fig. 7-6. The prediction agrees well with the measured profiles for various flow conditions.

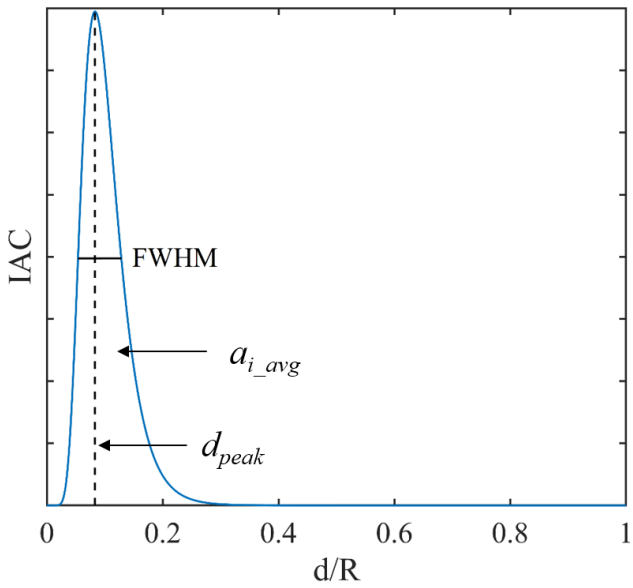

Figure 7-5 Sample IAC profile

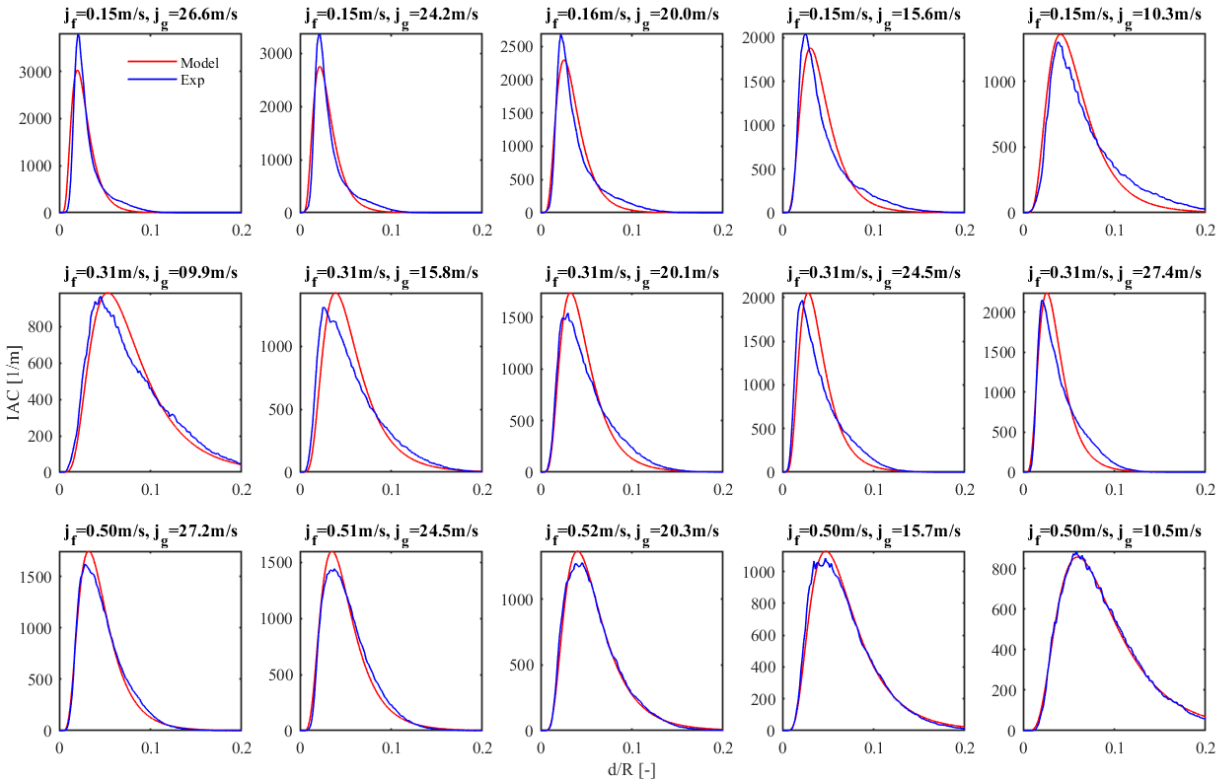

Figure 7-6 Comparison of measured IAC profiles with the model prediction

8. CONCLUSIONS AND FUTURE WORK

8.1 Summary of Current Work

The purposes of this dissertation are to improve the interfacial structure prediction capability for various flow regimes. The major accomplishments of this dissertation are summarized based on previous chapters as follows:

1. Established a reliable database focusing on bubbly to slug transition flow in a small size pipe and a narrow rectangular channel. To improve the two-group IATE model concentrating on intergroup transfer, vertical-upward air-water two-phase flow experiments were performed at two experimental facilities: a 25.4 mm inner diameter pipe and a 200 mm ×10 mm narrow rectangular channel. The test matrix covers the bubbly to slug transition region to characterize the transition from one-group flow to two-group flow. Significant intergroup transfer along the axial direction is observed for low superficial liquid velocity conditions, which is unique among the currently available database.

2. Evaluated the state-of-the-art two-group IATE models against the newly developed experimental database. The original two-group IATE model for moderate size pipes as well as most recent improvements are evaluated using the database. Both the original and improved models underestimate the intergroup transfer and cannot accurately predict the axial development of IAC.

3. Developed the IATE model to dynamically predict the intergroup transfer at bubbly to slug transition flows. The reasons for the discrepancy of the previous IATE model were analyzed in detail. The intergroup wake-entrainment model was improved to reflect intergroup void and IAC transfer and the transition flow. IATE with the newly developed model can predict the intergroup transition for both small size pipes and moderate size pipes.

4. Developed the local measurement instrumentation for churn-turbulent and annular flow. The four-sensor droplet capable conductivity probe (DCCP-4) was developed to capture all interfaces

in churn-turbulent and annular flow. Compared to the conventional four-sensor probe, it incorporates one more sensor to distinguish the continuous liquid phase and the dispersed liquid phase. The probe circuit was also improved significantly to get a much faster signal response speed and much less interference to handle the complicated flow structure in churn-turbulent and annular flow.

5. Established the first local two-phase flow experimental data set in the churn-turbulent to annular transition region. Using the newly developed DCCP-4, experiments were performed for the churn-turbulent to annular transition flow to get the local time-averaged volume faction, IAC, and velocity for various fields in annular flow including the droplet, bubble, and liquid ligament. The reliability of the measurement was checked with both theoretical models and area-average comparisons to bulk instrumentation.

6. Extended the local measurement capability to wispy annular flow using the DCCP-4 and film thickness probes. Few previous studies focused on wispy annular flow. Using the DCCP-4 and the film thickness probe together, the flow structure for wispy annular flow can be measured: in the center, the interfaces of droplets and ligaments are captured by the DCCP-4, and in the near-wall region, the film dynamics are captured by the film probe. Local measurements using this approach was performed at four wispy annular flow conditions. The near-wall IAC and volume fraction profile measured by the DCCP-4 and film probe agree well with each other, which supports the reliability of both instruments.

7. An annular flow wave structure database is established using a conductance film probe. Important parameters including average film thickness, wave height, base film thickness, wave frequency, wave velocity, and pressure drop are measured and analyzed. Existing models for predicting these parameters and interfacial shear are comprehensively reviewed and evaluated using the new data.

8. Developed a new annular flow IAC model. A constitutive model to predict the interfacial area between the gas core and the liquid film is proposed by assuming the radial IAC profile can be

approximately expressed as a log-normal distribution. The new model is evaluated using the experimental results, and the measured IAC profiles can be well predicted.

8.2 Recommendation for Future Research

Based on the research progress of this dissertation, future research in the following directions is recommended:

1. Perform comprehensive experiments in churn-turbulent, annular, and wispy annular flow using DCCP-4 at multiple axial locations. Detailed local measurement data is important to the development and benchmark of the multi-field two-fluid model

2. Investigate the mist annular to wispy annular transition mechanism using the DCCP-4. With the capability of DCCP-4 to identify the connectivity between the liquid film and the liquid phase in the gas core, more detailed information about this transition can be obtained through the experiment, and corresponding constitutive models for wispy annular flow can be developed.

3. Benchmark the IATE with a 3-D two-fluid model for developing flow. This study evaluates 1-D IATE for conditions with significant flow structure change in the axial direction, and improved corresponding intergroup transition terms. To fulfill the dynamic prediction, the IATE model needs to be benchmarked and evaluated under the 3-D two-fluid model framework, especially for the developing flow conditions.

4. Evaluate the annular flow IAC model using a CFD code. As the major difficulty to use the two-fluid model in annular flow CFD calculation, the interface between the gas core and the liquid film can be characterized using the new IAC model developed in this study. To extend the two-fluid model application range to annular flow, this IAC model should be implemented into a CFD code to predict the 3-D annular flow structure.

5. Development of an interfacial area transition mechanism from churn-turbulent flow to annular flow. The IATE can be applied to bubbly, slug, and churn-turbulent flows, which are dominated by bubble dynamics. The annular flow gas core and the liquid film interface can be predicted by

the IAC model developed in this study. Aiming at the comprehensive IAC model from bubbly to annular flow, a proper IAC transition mechanism from churn-turbulent flow to annular flow should be developed.

APPENDIX A. IATE SOURCE/SINK TERMS

Table A. Summary of IATE source/sink terms and supporting models

Mechanism	Source/Sink Term Models	Supporting Closure Equations
Random collision	$\phi_{RC}^{(1)} = \left\langle \delta A_{i1}^{(11,1)} \right\rangle_R R_{RC}^{(1)}$ $\phi_{1,RC}^{(11,2)} = \left\langle \delta A_{i1}^{(11,2)} \right\rangle_R R_{RC}^{(1)}$ $\phi_{2,RC}^{(11,2)} = \left\langle \delta A_{i2}^{(11,2)} \right\rangle_R R_{RC}^{(1)}$ $\eta_{RC}^{(11,2)} = \left\langle \delta V^{(11,2)} \right\rangle_R R_{RC}^{(1)}$ $R_{RC}^{(1)} = C_{RC}\left[\frac{u_t n_1^2 D_{sm1}^2}{\alpha_{1,max}^{1/3}\left(\alpha_{1,max}^{1/3}-\alpha_1^{1/3}\right)}\right]\left[1-\exp\left(-C\frac{\alpha_{1,max}^{1/3}\alpha_1^{1/3}}{\alpha_{1,max}^{1/3}\left(\alpha_{1,max}^{1/3}-\alpha_1^{1/3}\right)}\right)\right]$	$n_1 = \frac{1}{36\pi}\frac{a_{i1}^3}{\alpha_1^2}$ When D_{sm1}>0.0083 m: $\left\langle \delta A_{i1}^{(11,1)} \right\rangle_R = D_{sm1}^2\left[-3.142D_1^{*3}+2.183D_1^{*5}-0.395D_1^{*8}+3.392\left(0.579D_1^{*3}-1\right)^{\frac{8}{3}}\right]$ $\left\langle \delta A_{i1}^{(11,2)} \right\rangle_R = D_{sm1}^2\left[8.82+2.035\left(0.579D_1^{*3}-1\right)^{8/3}-5.428D_1^{*3}\right]$ $\left\langle \delta A_{i2}^{(11,2)} \right\rangle_R = D_{sm1}^2\left(6.462-2.182D_1^{*5}+0.395D_1^{*8}\right)$ $\left\langle \delta V^{(11,2)} \right\rangle_R = D_{sm1}^3\xi\left(0.603+0.349D_1^{*3}\right)$ $\xi = 2\left(1-0.2894D_1^{*3}\right)^2$, $D_1^* = \frac{D_c}{D_{sm1}}$ Otherwise: $\left\langle \delta A_{i1}^{(11,1)} \right\rangle_R = 1.0001 D_{sm1}{}^2$, $\left\langle \delta A_{i1}^{(11,2)} \right\rangle_R = \left\langle \delta A_{i2}^{(11,2)} \right\rangle_R = \left\langle \delta V^{(11,2)} \right\rangle_R = 0$
Wake entrainment	$\phi_{WE}^{(1)} = \left\langle \delta A_{i1}^{(11,1)} \right\rangle_R R_{WE}^{(1)}$, $\phi_{1,WE}^{(11,2)} = \left\langle \delta A_{i1}^{(11,2)} \right\rangle_R R_{WE}^{(1)}$, $\phi_{2,WE}^{(11,2)} = \left\langle \delta A_{i2}^{(11,2)} \right\rangle_R R_{WE}^{(1)}$ $\eta_{WE}^{(11,2)} = \left\langle \delta V^{(11,2)} \right\rangle_R R_{WE}^{(1)}$, $R_{WE}^{(1)} = C_{WE}^{(1)} C_D^{1/3} n_1^2 D_{sm1}^2 v_{r1}$ $\phi_{WE}^{(2)} = -C_{WE}^{(2)} K_{WE2}^{(2)} \alpha_2 \left[1-\exp\left(\frac{-2331\alpha_2 V_s^{*2}}{D^5}\right)\right]\left[\exp\left(\frac{-0.06C_1\left(\alpha_{2m}/\alpha_2-1\right)}{V_s^*}\right)-1\right]^{-1}$ $\phi_{1,WE}^{(12,2)} = -C_{WE}^{(12,2)} K_{1,WE}^{(12,2)} V_s^{*\frac{1}{2}} \frac{\alpha_1\alpha_2}{1-\alpha_2} \kappa_{fr} D_{sm1}^{-1}$ $\phi_{2,WE}^{(12,2)} = C_{WE}^{(12,2)} K_{2,WE}^{(12,2)} V_s^{*\frac{1}{2}} \frac{\alpha_1\alpha_2}{1-\alpha_2} \kappa_{fr}$ $\eta_{WE}^{(12,2)} = C_{WE}^{(12,2)} K_{WE}^{(12,2)} V_s^{*\frac{1}{2}} \frac{\alpha_1\alpha_2}{1-\alpha_2} \kappa_{fr}$	$v_{r1} = \left(\frac{gD_{sm1}}{3C_D}\frac{\Delta\rho}{\rho_f}\right)$, $C_D = \frac{2}{3}D_{sm1}\sqrt{\frac{g\Delta\rho}{\sigma}}\left[\frac{1+17.67\left(1-\alpha_1\right)^{2.6}}{18.67\left(1-\alpha_1\right)^3}\right]^3$ $K_{WE2}^{(2)} = 10.24D^{\frac{3}{2}}$, $\kappa_{fr} = 1-\exp\left(\frac{-C_{fr}V_s^{*\frac{1}{2}}}{D^{\frac{1}{2}}}\right)$, $K_{1,WE}^{(12,2)} = 3\pi C_g D^{1/2}$ $K_{2,WE}^{(12,2)} = 2\pi C_g D^{-1/2}\alpha_{2m}{}^{-1/2}$, $K_{WE}^{(12,2)} = 0.5\pi C_g D^{1/2}$ $C_g = \left(\frac{2g\Delta\rho}{\rho_f}\right)^{\frac{1}{2}}$, $V_s^* = \frac{V_{s,min}}{V_{s,max}}$ and can be determined by $D_{sm2} = 1.35D/(1+6.86V_s^*-2.54V_s^{*2})$
Shearing-off	$\phi_{1,SO}^{(2,1)} = C_{SO}K_{1,SO}^{(2,1)}\alpha_2 V_s^{-\frac{4}{5}^*}\left(1-0.6535\kappa_{bl}\right)\xi_{SO}\kappa_{fr}{}^2$ $\phi_{2,SO}^{(2,1)} = -C_{SO}K_{2,SO}^{(2,1)}\alpha_2 V_s^{-\frac{1}{5}^*}\left(1-0.6474\kappa_{bl}\right)\kappa_{fr}{}^{\frac{4}{5}}$ $\eta_{SO}^{(2,1)} = C_{SO}K_{SO}^{(2,1)}\alpha_2 V_s^{-\frac{1}{5}^*}\left(1-0.6474\kappa_{bl}\right)\kappa_{fr}{}^{4/5}$	$\xi_{SO} = \left\{1-\exp\left[-\gamma_{SO}\left(\frac{\alpha_{2,\max}}{\alpha_{2,\max}-\alpha_2}\right)^{\beta_{SO}}\frac{We_{cr}}{We_1}\right]\right\}^{-1}$ $\kappa_{bl} = \left(D^{-0.3}\alpha_{2m}^{-0.5}v_g^{0.2}C_g^{-0.2}V_s^{-0.7*}\kappa_{fr}{}^{-0.2}\right)^{1/7}$ $K_{1,SO}^{(2,1)} = 0.5755v_g^{0.2}C_g^2\left(\frac{\rho_f}{\sigma D}\right)^{3/5}$ $K_{2,SO}^{(2,1)} = 4.4332v_g^{0.2}D^{-9/5}\alpha_{2m}{}^{1/2}C_g^{4/5}$ $K_{SO}^{(2,1)} = 1.1083v_g^{0.2}D^{-4/5}C_g^{4/5}$ $We_2 = \frac{\rho_f u_{r2}^2 D_{sm2}}{\sigma}$

Table A continued

Turbulence impact	$\varphi_{TI}^{(1)} = C_{TI}\frac{1}{18}\left(\frac{\overline{u_t'^2}a_{i1}^2}{\alpha_1}\right)\left[1-\frac{We_{cr}}{We^*}\right]^{1/2}\exp\left(-\frac{We_{cr}}{We^*}\right)$ for $We^*>We_{cr1}$, Otherwise $\varphi_{TI}^{(1)}=0$	$We^* = \frac{\rho_f \overline{u_t'^2} D_{sm1}}{\sigma}$, $\overline{u_t'^2} = \overline{u_{t,w}'^2} + \overline{u_{t,iso}'^2}$, $\overline{u_{t,w}'} = 0.056 C_g \left(\frac{D^3}{V_s^*}\right)^{1/2} \mathrm{K}_{fr}$ $\overline{u_{t,iso}'} = \left(\varepsilon D_{sm1}\right)^{2/3}$
Pressure change	$\phi_{1,\exp} = -\frac{2}{3}\frac{a_{i1}\upsilon_{g1}}{p}\frac{\partial p}{\partial z}$, $\phi_{2,\exp} = -\left(\frac{4+10.19V_s^{*2}}{\alpha_{2m}^{0.5}D}\right)\frac{a_{i2}\upsilon_{g2}}{p}\frac{\partial p}{\partial z}$ $\phi_{\exp 12} = \chi D_{c1}^{*2}\frac{a_{i1}}{\alpha_1}\frac{1}{1-CD_{c1}^{*3}}\left(\nabla\cdot\left(\alpha_1\upsilon_{g1}\right)-\sum_j \eta_{j,1}^{\text{inter}}\right)$ $\eta_{\exp 12} = \frac{\chi D_{c1}^{*3}}{1-\chi D_{c1}^{*3}}\left(\nabla\cdot\left(\alpha_1\upsilon_{g1}\right)-\sum_j \eta_{j,1}^{\text{inter}}\right)$	$\chi = 4.44\times10^{-3}\left(\frac{\langle D_{sm1}\rangle}{D_c}\right)^{0.36}\langle\alpha_1\rangle^{-1.35}$, $D_{c1}^* = \frac{D_c}{D_{\text{sm1}}}$ $\sum_j \eta_{j,1}^{\text{inter}} = -\left(\eta_{RC}^{(11,2)}+\eta_{WE}^{(11,2)}+\eta_{WE}^{(12,2)}+\eta_{SO}^{(2,1)}\right)$

APPENDIX B. ANNULAR FLOW EXPERIMENT DATA

Table B-1. Film thickness, wave height, base film, wave velocity, and wave frequency data

Run#	j_f [m/s]	j_{g0} [m/s] (Inlet)	j_{g3} [m/s] (z/D_h=141)	δ_{avg} [mm]	h [mm]	δ_{base} [mm]	v_w [m/s]	f [Hz]
1	0.061	9.84	9.59	0.838	2.364	0.648	0.99	8.00
2	0.062	15.34	14.94	0.480	1.49	0.395	1.91	8.60
3	0.062	19.68	19.12	0.355	1.128	0.303	2.34	9.27
4	0.061	24.24	23.44	0.304	0.936	0.264	2.78	10.37
5	0.061	26.92	26.00	0.254	0.834	0.233	3.01	10.57
6	0.150	26.65	25.45	0.414	1.136	0.263	3.05	16.73
7	0.154	24.24	23.23	0.437	1.251	0.272	3.01	15.93
8	0.159	19.98	19.32	0.518	1.491	0.288	2.75	13.67
9	0.154	15.62	15.20	0.613	1.806	0.311	2.29	11.37
10	0.155	10.34	10.45	0.901	2.429	0.503	1.59	10.23
11	0.314	9.95	9.97	1.035	2.67	0.649	2.25	10.87
12	0.306	15.75	15.70	0.742	1.963	0.498	2.69	11.87
13	0.309	20.13	19.87	0.655	1.705	0.41	3.13	13.73
14	0.306	24.54	23.94	0.541	1.431	0.309	3.40	15.57
15	0.307	27.37	26.46	0.532	1.341	0.296	3.60	16.90
16	0.499	27.24	25.62	0.621	1.504	0.415	3.91	14.27
17	0.505	24.46	23.23	0.686	1.61	0.455	3.68	12.80
18	0.517	20.32	19.48	0.755	1.871	0.504	3.50	11.80
19	0.503	15.67	15.15	0.892	2.367	0.573	3.27	9.50
20	0.500	10.46	10.25	1.182	3.394	0.736	3.27	8.23
21	1.028	10.25	9.58	1.331	4.081	0.855	12.82	8.37
22	1.000	15.51	14.09	0.989	2.907	0.675	15.15	8.90
23	0.992	20.27	17.99	0.832	2.327	0.583	16.13	9.60
24	1.005	24.09	20.89	0.768	2.192	0.546	16.67	8.93
25	0.989	29.11	24.44	0.647	1.716	0.456	7.25	10.93
26	1.742	29.57	21.73	0.836	2.661	0.59	26.32	10.13
27	2.040	24.55	18.23	1.034	3.228	0.718	25.00	10.60
28	2.022	20.19	15.51	1.150	3.659	0.775	22.73	10.03
29	2.049	14.96	11.86	1.440	4.425	0.946	19.23	9.67
30	2.030	10.71	8.82	1.804	5.209	1.088	16.13	10.60

Table B-2. Pressure measurement data

Run#	j_f [m/s]	j_{g0} [m/s]	P1 [kPa] (z/D_h=15)	P2 [kPa] (z/D_h=78)	P3 [kPa] (z/D_h=141)
1	0.061	9.84	110.23	106.23	103.86
2	0.062	15.34	109.77	106.19	103.95
3	0.062	19.68	110.52	106.81	104.16
4	0.061	24.24	111.98	107.92	104.61
5	0.061	26.92	112.83	108.66	104.76
6	0.150	26.65	118.62	112.57	105.99
7	0.154	24.24	117.61	111.84	105.57
8	0.159	19.98	115.40	110.12	104.63
9	0.154	15.62	113.61	108.83	103.99
10	0.155	10.34	112.98	108.30	100.07
11	0.314	9.95	117.42	110.99	101.00
12	0.306	15.75	119.33	112.40	101.56
13	0.309	20.13	122.10	114.32	102.50
14	0.306	24.54	125.37	116.81	103.75
15	0.307	27.37	127.64	118.50	104.67
16	0.499	27.24	137.36	125.38	107.62
17	0.505	24.46	134.85	123.73	106.57
18	0.517	20.32	131.06	120.94	105.55
19	0.503	15.67	126.27	117.48	104.62
20	0.500	10.46	123.20	114.96	103.36
21	1.028	10.25	140.17	126.64	108.31
22	1.000	15.51	147.14	131.64	111.41
23	0.992	20.27	154.77	137.06	114.00
24	1.005	24.09	160.62	141.25	116.70
25	0.989	29.11	169.52	148.14	120.56
26	1.742	29.57	210.77	180.93	137.74
27	2.040	24.55	209.47	180.41	136.23
28	2.022	20.19	197.77	171.28	131.73
29	2.049	14.96	180.81	161.74	127.71
30	2.030	10.71	170.80	149.95	122.91

REFERENCES

[1] G. B. G. Wallis, *One-dimensional two-phase flow*. New York: McGraw-Hill, 1969.

[2] N. Zuber and J.A. Findlay, "Average volumetric concentration in two-phase flow systems," *J. Heat Transfer*, vol. 87, no. 4, pp. 453–468, 1965.

[3] M. Ishii and K. Mishima, "Two-fluid model and hydrodynamic constitutive relations," *Nucl. Eng. Des.*, vol. 82, no. 2–3, pp. 107–126, 1984.

[4] D. Jamet, O. Lebaigue, N. Coutris, and J. M. Delhaye, "The second gradient method for the direct numerical simulation of liquid--vapor flows with phase change," *J. Comput. Phys.*, vol. 169, no. 2, pp. 624–651, 2001.

[5] M. Ishii, "Thermo-Fluid Dynamic Theory of Two-Phase Flow., volume 22 of Direction des études et recherches d'électricité de France," *Eyrolles, Paris*, 1975.

[6] J. M. Delhaye, "Basic equations for two-phase flow modeling," *Two-Phase Flow, Heat Transf. Power Process Ind.*, 1981.

[7] D. A. Drew, "Analytical modeling of multiphase flow," in *Particulate Two-phase Flow*, M. C. Roco, Boston: Butterworth-Heinemann, 1993.

[8] Y. Mi, M. Ishii, and L. H. Tsoukalas, "Flow regime identification methodology with neural networks and two-phase flow models," *Nucl. Eng. Des.*, vol. 204, no. 1–3, pp. 87–100, 2001.

[9] Z. Li, G. Wang, M. Yousaf, X. Yang, and M. Ishii, "Flow structure and flow regime transitions of downward two-phase flow in large diameter pipes," *Int. J. Heat Mass Transf.*, vol. 118, pp. 812–822, 2018.

[10] G. Wang, Z. Li, M. Yousaf, X. Yang, and M. Ishii, "Experimental study on vertical downward air-water two-phase flow in a large diameter pipe," *Int. J. Heat Mass Transf.*, vol. 118, pp. 919–930, 2018.

[11] Z. Dang *et al.*, "Investigation of the effect of the electrode distance on the impedance void meter performance in the two-phase flow measurement," *Exp. Therm. Fluid Sci.*, vol. 101, 2019.

[12] J. M. Kelly, "Thermal-hydraulic modeling needs for passive reactors," in *Workshop on Transient Thermal-Hydraulic and Neutronic Codes Requirements*, 1997, p. 144.

[13] G. A. Mortensen, "Long-term plan for NRC thermal-hydraulic code development," *Rep. to US NRC under Contract DEAC07-94ID13223*, 1995.

[14] G. Kocamustafaogullari and M. Ishii, “Foundation of the interfacial area transport equation and its closure relations,” *Int. J. Heat Mass Transf.*, vol. 38, no. 3, pp. 481–493, 1995.

[15] C. S. Brooks, “Wall nucleation and the two-fluid model in subcooled boiling flow,” Ph.D. dissertation, Purdue University, West Lafayett, IN, 2014.

[16] J. D. Talley, S. Kim, J. Mahaffy, S. M. Bajorek, and K. Tien, “Implementation and evaluation of one-group interfacial area transport equation in TRACE,” *Nucl. Eng. Des.*, vol. 241, no. 3, pp. 865–873, 2011.

[17] X. Wang and X. Sun, “Three-dimensional simulations of air--water bubbly flows,” *Int. J. Multiph. Flow*, vol. 36, no. 11–12, pp. 882–890, 2010.

[18] X. Y. Fu and M. Ishii, “Two-group interfacial area transport in vertical air-water flow - II. Model evaluation,” *Nucl. Eng. Des.*, vol. 219, no. 2, pp. 169–190, 2003.

[19] X. Sun, S. Kim, M. Ishii, and S. G. Beus, “Modeling of bubble coalescence and disintegration in confined upward two-phase flow,” *Nucl. Eng. Des.*, vol. 230, no. 1–3, pp. 3–26, 2004.

[20] X. Yang, J. P. Schlegel, Y. Liu, S. Paranjape, T. Hibiki, and M. Ishii, “Experimental study of interfacial area transport in air-water two phase flow in a scaled 8x8 BWR rod bundle,” *Int. J. Multiph. Flow*, vol. 50, no. 2013, pp. 16–32, 2013.

[21] G. Wang, X. Xiao, Q. Zhu, X. Yang, S. W. Chen, and M. Ishii, “Local measurement of adiabatic two-phase flow in an annulus under low-frequency vibration,” in *Proc. of ANS Winter Meeting, Washington, DC*, 2015.

[22] X. Xiao, Q. Zhu, G. Wang, S.-W. Chen, M. Ishii, and Y. Zhang, “Vibration effects on bubbly flow structure in an annulus,” in *Proc. of 24th International Conference on Nuclear Engineering (ICONE 2016)*, vol. 3. 2016,

[23] J. P. Schlegel, T. Hibiki, and M. Ishii, “Two-group modeling of interfacial area transport in large diameter channels,” *Nucl. Eng. Des.*, vol. 293, pp. 75–86, 2015.

[24] Q. Wu, S. Kim, M. Ishii, and S. G. Beus, “One-group interfacial area transport in vertical bubbly flow,” *Int. J. Heat Mass Transf.*, vol. 41, no. 8–9, pp. 1103–1112, 1998.

[25] M. Ishii and S. Kim, “Development of One-Group and Two-Group Interfacial Area Transport Equation,” *Nucl. Sci. Eng.*, vol. 146, no. 3, pp. 257–273, 2004.

[26] M. Ishii and T. Hibiki, *Thermo-fluid dynamics of two-phase flow*. Springer Science & Business Media, 2010.

[27] M. Ishii and N. Zuber, “Drag coefficient and relative velocity in bubbly, droplet or particulate flows,” *AIChE J.*, vol. 25, no. 5, pp. 843–855, 1979.

[28] T. S. Worosz, “Interfacial area transport equation for bubbly to cap-bubbly transition flows,” Ph.D. dissertation, Pennsylvania State University, State College, PA, 2015.

[29] X. Sun, S. Kim, M. Ishii, and S. G. Beus, “Model evaluation of two-group interfacial area transport equation for confined upward flow,” *Nucl. Eng. Des.*, vol. 230, no. 1–3, pp. 27–47, 2004.

[30] T. R. Smith, J. P. Schlegel, T. Hibiki, and M. Ishii, “Mechanistic modeling of interfacial area transport in large diameter pipes,” *Int. J. Multiph. Flow*, vol. 47, no. 2012, pp. 1–16, 2012.

[31] X. Y. Fu and M. Ishii, “Two-group interfacial area transport in vertical air--water flow: I. Mechanistic model,” *Nucl. Eng. Des.*, vol. 219, no. 2, pp. 143–168, 2003.

[32] B. C. Doup, “Methodology Development of a Gas-Liquid Dynamic Flow Regime Transition Model,” Ph.D. dissertation, Ohio State University, Columbus, OH, 2014.

[33] M. S. Bernard, “Implementation of the interfacial area transport equation in TRACE for boiling two-phase flows,” Ph.D. dissertation, Pennsylvania State University, State College, PA, 2014.

[34] R. T. Lahey and D. A. Drew, “The analysis of two-phase flow and heat transfer using a multidimensional, four field, two-fluid model,” *Nucl. Eng. Des.*, vol. 204, no. 1–3, pp. 29–44, 2001.

[35] D. A. Drew and R. T. Lahey Jr, “An analytical approach to bubble/slug flow regime modeling in a multi-field two-fluid model,” in *Proc. 6th ASME/JSME Conference*, 2003.

[36] S. K. Wang *et al.*, “3-D turbulence structure and phase distribution measurements in bubbly two-phase flows,” *Int. J. Multiph. Flow*, vol. 13, no. 3, pp. 327–343, 1987.

[37] V. Velidandla, S. Putta, R. P. Roy, and S. P. Kalra, “Velocity field in turbulent subcooled boiling flow,” in *Proc. of the 30th 1995 National Heat Transfer Conference*, vol. 314, pp. 107–124, 1995.

[38] R. Hino and T. Ueda, “Studies on heat transfer and flow characteristics in subcooled flow boiling—Part 2. Flow characteristics,” *Int. J. Multiph. Flow*, vol. 11, no. 3, pp. 283–297, 1985.

[39] P. M. Carrica, D. Drew, F. Bonetto, and R. T. Lahey Jr, “A polydisperse model for bubbly two-phase flow around a surface ship,” *Int. J. Multiph. Flow*, vol. 25, no. 2, pp. 257–305, 1999.

[40] Y. Liu, “Three-dimensional interfacial area transport in gas-dispersed two-phase flow up to churn-annular flow transition,” Ph.D. dissertation, Purdue University, West Lafayett, IN, 2008.

[41] Q. Zhu, “Experiments and modeling for churn-turbulent to annular flow,” Ph.D. dissertation, Purdue University, West Lafayett, IN, 2017.

[42] Z. Dang *et al.*, “Experimental study of interfacial characteristics of vertical upward air-water two-phase flow in 25.4mm ID round pipe,” *Int. J. Heat Mass Transf.*, vol. 108, pp. 1825–1838, 2017.

[43] G. Wang *et al.*, “Experimental study on interfacial structure and interfacial area transport in downward two-phase flow,” *Int. J. Heat Mass Transf.*, vol. 106, pp. 1303–1317, 2017.

[44] T. Hibiki, M. Ishii, and Z. Xiao, “Axial interfacial area transport of vertical bubbly flows,” *Int. J. Heat Mass Transf.*, vol. 44, no. 10, pp. 1869–1888, 2001.

[45] L.S. Zhai, P. Bian, Z.K. Gao, and N.D. Jin, “The measurement of local flow parameters for gas--liquid two-phase bubbly flows using a dual-sensor probe array,” *Chem. Eng. Sci.*, vol. 144, pp. 346–363, 2016.

[46] G. Wang, Q. Zhu, Z. Dang, X. Yang, and M. Ishii, “Prediction of interfacial area concentration in a small diameter round pipe,” *Int. J. Heat Mass Transf.*, vol. 130, pp. 252–265, 2019.

[47] A. Cartellier, “Simultaneous void fraction measurement, bubble velocity, and size estimate using a single optical probe in gas--liquid two-phase flows,” *Rev. Sci. Instrum.*, vol. 63, no. 11, pp. 5442–5453, 1992.

[48] E. Barrau, N. Rivière, C. Poupot, and A. Cartellier, “Single and double optical probes in air-water two-phase flows: real time signal processing and sensor performance,” *Int. J. Multiph. Flow*, vol. 25, no. 2, pp. 229–256, 1999.

[49] M. Honkanen, P. Saarenrinne, T. Stoor, and J. Niinimäki, “Recognition of highly overlapping ellipse-like bubble images,” *Meas. Sci. Technol.*, vol. 16, no. 9, p. 1760, 2005.

[50] Y. Fu and Y. Liu, “Development of a robust image processing technique for bubbly flow measurement in a narrow rectangular channel,” *Int. J. Multiph. Flow*, vol. 84, pp. 217–228, 2016.

[51] D. Lucas, E. Krepper, and H.-M. Prasser, “Development of co-current air--water flow in a vertical pipe,” *Int. J. Multiph. Flow*, vol. 31, no. 12, pp. 1304–1328, 2005.

[52] H.M. Prasser, “Evolution of interfacial area concentration in a vertical air-water flow measured by wire-mesh sensors,” *Nucl. Eng. Des.*, vol. 237, no. 15–17, pp. 1608–1617, 2007.

[53] A. Manera, B. Ozar, S. Paranjape, M. Ishii, and H.M. Prasser, “Comparison between wire-mesh sensors and conductive needle-probes for measurements of two-phase flow parameters,” *Nucl. Eng. Des.*, vol. 239, no. 9, pp. 1718–1724, 2009.

[54] S. Kim, X. Y. Fu, X. Wang, and M. Ishii, “Development of the miniaturized four-sensor conductivity probe and the signal processing scheme,” *Int. J. Heat Mass Transf.*, vol. 43, no. 22, pp. 4101–4118, 2000.

[55] Y. Liu, X. Yang, Q. Zhu, P. Ju, M. Ishii, and J. R. Buchanan Jr, “Development of the droplet-capable conductivity probe for measurement of liquid-dispersed two-phase flow,” *Int. J. Multiph. Flow*, vol. 88, pp. 238–250, 2017.

[56] S. T. Revankar and M. Ishii, “Theory and measurement of local interfacial area using a four sensor probe in two-phase flow,” *Int. J. Heat Mass Transf.*, vol. 36, no. 12, pp. 2997–3007, 1993.

[57] K. Mishima and M. Ishii, “Flow regime transition criteria for upward two-phase flow in vertical tubes,” *Int. J. Heat Mass Transf.*, vol. 27, no. 5, pp. 723–737, 1984.

[58] G. Wang, M. Zhang, and M. Ishii, “Flow structure of bubbly to slug transition flow in a small pipe,” *Int. J. Heat Mass Transf.*, vol. 147, p. 118943, 2020.

[59] G. Wang, M. Zhang, and M. Ishii, “Interfacial characteristics at bubbly to slug transition flow in a small diameter pipe,” in *Proc. of the 27th International Conference on Nuclear Engineering (ICONE2019)*, pp. 1969. 2019,

[60] X. Sun, S. Kim, L. Cheng, M. Ishii, and S. G. Beus, “Interfacial structures in confined cap-turbulent and churn-turbulent flows,” *Int. J. Heat Fluid Flow*, vol. 25, pp. 44–57, 2004.

[61] Y. Liu, D. Y. Lee, T. Roy, M. Ishii, and J. R. Buchanan Jr., "The development of two-phase flow structures in air-water planar bubble jets," *Int. J. Multiph. Flow*, vol. 56, pp. 25–39, 2013.

[62] Y. Liu, T. Roy, D. Y. Lee, M. Ishii, and J. R. Buchanan Jr., "Experimental study of non-uniform inlet conditions and three-dimensional effects of vertical air-water two-phase flow in a narrow rectangular duct," *Int. J. Heat Fluid Flow*, vol. 39, pp. 173–186, 2013.

[63] S. L. Sharma, "Investigation of Gas-Liquid Two-Phase Flow Using Three-Field Two-Fluid Model and Two-Group Interfacial Area Transport Equation in CFD Code," Ph.D. dissertation, Purdue University, West Lafayett, IN, 2016.

[64] G. Wang, Q. Zhu, and M. Ishii, "Interfacial structures in bubbly-to-slug transition flows in a duct," *Nucl. Technol.*, vol. 206, no. 2, pp. 347–357, 2020.

[65] T. Hibiki and K. Mishima, "Flow regime transition criteria for upward two-phase flow in vertical narrow rectangular channels," *Nucl. Eng. Des.*, vol. 203, no. 2–3, pp. 117–131, 2001.

[66] F. Lehr, M. Millies, and D. Mewes, "Bubble size distributions and flow fields in bubble columns," *AIChE J.*, vol. 42, no. 11, pp. 1225–1233, 2002.

[67] E. Camarasa, C. Vial, S. Poncin, G. Wild, N. Midoux, and J. Bouillard, "Influence of coalescence behaviour of the liquid and of gas sparging on hydrodynamics and bubble characteristics in a bubble column," *Chem. Eng. Process. Process Intensif.*, vol. 38, no. 4–6, pp. 329–344, 1999.

[68] P. L. C. Lage and R. O. Esposito, "Experimental determination of bubble size distributions in bubble columns : prediction of mean bubble diameter and gas hold up," *Powder Technol.*, pp. 142–150, 1999.

[69] R. Schäfer, C. Merten, and G. Eigenberger, "Bubble size distributions in a bubble column reactor under industrial conditions," *Exp. Therm. Fluid Sci.*, vol. 26, pp. 595–604, 2002.

[70] T. Wang, J. Wang, and Y. Jin, "Population Balance Model for Gas - Liquid Flows : Influence of Bubble Coalescence and Breakup Models," *Ind. Eng. Chem. Res.*, vol. 44, no. 19, pp. 7540–7549, 2005.

[71] A. Tomiyama, H. Tamai, I. Zun, and S. Hosokawa, "Transverse migration of single bubbles in simple shear flows," *Chem. Eng. Sci.*, vol. 57, no. 11, pp. 1849–1858, 2002.

[72] C. T. Crowe, *Multiphase Flow Handbook*, Boca Raton: CRC Press. 2005.

[73] J. C. Lagarias, J. A. Reeds, M. H. Wright, and P. E. Wright, "Convergence properties of the Nelder--Mead simplex method in low dimensions," *SIAM J. Optim.*, vol. 9, no. 1, pp. 112–147, 1998.

[74] I. Kataoka, M. Ishii, and A. Serizawa, "Local formulation and measurements of interfacial area concentration in two-phase flow," *Int. J. Multiph. Flow*, vol. 12, no. 4, pp. 505–529, 1986.

[75] J. A. R. Bennett, "Data on the vertical flow of air-water mixture in the annular and dispersed flow regions, Part I: Preliminary study," *Trans. Inst. Chem. Eng.*, vol. 39, p. 101, 1961.

[76] G. F. Hewitt, R. D. King, and P. C. Lovegrove, "Liquid film and pressure drop studies," *Chem. Proc. Eng*, vol. 45, pp. 191–200, 1964.

[77] L. E. Gill and G. F. Hewitt, "Data on the upwards annular flow of air-water mixtures," *Chem. Eng. Sci.*, vol. 20, no. 2, pp. 71–88, 1965.

[78] M. Miya, D. E. Woodmansee, and T. J. Hanratty, "A model for roll waves in gas-liquid flow," *Chem. Eng. Sci.*, vol. 26, no. 11, pp. 1915–1931, 1971.

[79] R. C. Brown, P. Andreussi, and S. Zanelli, "The use of wire probes for the measurement of liquid film thickness in annular gas-liquid flows," *Can. J. Chem. Eng.*, vol. 56, no. 6, pp. 754–757, 1978.

[80] J. E. Koskie, I. Mudawar, and W. G. Tiederman, "Parallel-wire probes for measurement of thick liquid films," *Int. J. Multiph. Flow*, vol. 15, no. 4, pp. 521–530, 1989.

[81] H. C. Kang and M. H. Kim, "The development of a flush-wire probe and calibration method for measuring liquid film thickness," *Int. J. Multiph. Flow*, vol. 18, no. 3, pp. 423–437, 1992.

[82] Q. Wu, G. J. Zhang, M. Ishii, S. T. Revankar, and R. Y. Lee, "Experimental simulation of corium dispersion phenomena in direct containment heating," *Nucl. Eng. Des.*, vol. 164, no. 1–3, pp. 237–255, 1996.

[83] G. F. Hewitt and D. N. Roberts, "Studies of two-phase flow patterns by simultaneous X-ray and flash photography," No. AERE-M-2159. Atomic Energy Research Establishment, Harwell, England (United Kingdom), 1969.

[84] X. Sun, "Two-group interfacial area transport equation for a confined test section," Ph.D. dissertation, Purdue University, West Lafayett, IN, 2001.

[85] I. Kataoka, M. Ishii, and K. Mishima, "Generation and size distribution of droplet in annular two-phase flow," *J. Fluids Eng.*, vol. 105, no. 2, pp. 230–238, 1983.

[86] G. Wang, K. Tang, M. Ishii, and W. Lafayette, "Film thickness and disturbance wave structure of upward annular flow," in *Proc. of 18th International Meeting on Nuclear Reactor Thermal-Hydraulics (NURETH-18) Portland, OR*, pp. 5193–5203, 2019.

[87] I. Kataoka, M. Ishii, and A. Nakayama, "Entrainment and desposition rates of droplets in annular two-phase flow," *Int. J. Heat Mass Transf.*, vol. 43, no. 9, pp. 1573–1589, 2000.

[88] P. Ju, C. S. Brooks, M. Ishii, Y. Liu, and T. Hibiki, "Film thickness of vertical upward co-current adiabatic flow in pipes," *Int. J. Heat Mass Transf.*, vol. 89, pp. 985–995, 2015.

[89] C. Berna, A. Escrivá, J. L. Muñoz-cobo, and L. E. Herranz, "Review of droplet entrainment in annular flow: Interfacial waves and onset of entrainment," *Prog. Nucl. Energy*, vol. 74, pp. 14–43, 2014.

[90] T. Fukano and T. Furukawa, "Prediction of the effects of liquid viscosity on interfacial shear stress and frictional pressure drop in vertical upward gas--liquid annular flow," *Int. J. Multiph. Flow*, vol. 24, no. 4, pp. 587–603, 1998.

[91] W. H. Henstock and T. J. Hanratty, "The interfacial drag and the height of the wall layer in annular flows," *AIChE J.*, vol. 22, no. 6, pp. 990–1000, 1976.

[92] K. Hori, M. Nakasatomi, K. Nishikawa, and K. Sekoguchi, "Study of Ripple Region in Annular Two-Phase Flow (3 rd Report, Effect of Liquid Viscosity on Gas-Liquid Interfacial Character and Friction Factor)," *Trans. Jap. Soc. Mech. Eng*, vol. 44, no. 387, pp. 3847–3856, 1978.

[93] D. F. Tatterson, J. C. Dallman, and T. J. Hanratty, "Drop sizes in annular gas-liquid flows," *AIChE J.*, vol. 23, no. 1, pp. 68–76, 1977.

[94] MATLAB (R2017b), "Documentation of function 'findpeaks," [Online], Available: https://www.mathworks.com/help/signal/ref/findpeaks.html, 2017 [Accessed Nov. 14, 2019].

[95] R. J. Belt, J. M. C. Van Westende, H. M. Prasser, and L. M. Portela, "Time and spatially resolved measurements of interfacial waves in vertical annular flow," *Int. J. Multiph. Flow*, vol. 36, no. 7, pp. 570–587, 2010.

[96] Y. Zhao, C. N. Markides, O. K. Matar, and G. F. Hewitt, "Disturbance wave development in two-phase gas-liquid upwards vertical annular flow," *Int. J. Multiph. Flow*, vol. 55, pp. 111–129, 2013.

[97] P. Sawant, M. Ishii, T. Hazuku, T. Takamasa, and M. Mori, "Properties of disturbance waves in vertical annular two-phase flow," *Nucl. Eng. Des.*, vol. 238, no. 12, pp. 3528–3541, 2008.

[98] P. de Jong, K. S. Gabriel, P. De Jong, and K. S. Gabriel, "A preliminary study of two-phase annular flow at microgravity: experimental data of film thickness," *Int. J. Multiph. Flow*, vol. 29, no. 8, pp. 1203–1220, 2003.

[99] L. M. Pan, H. He, P. Ju, T. Hibiki, and M. Ishii, "Experimental study and modeling of disturbance wave height of vertical annular flow," *Int. J. Heat Mass Transf.*, vol. 89, no. 2015, pp. 165–175.

[100] S. V Alekseenko, A. V Cherdantsev, O. M. Heinz, S. M. Kharlamov, and D. M. Markovich, "Analysis of spatial and temporal evolution of disturbance waves and ripples in annular gas – liquid flow," *Int. J. Multiph. Flow*, vol. 67, pp. 122–134, 2014.

[101] H. Han, Z. Zhu, and K. Gabriel, "A study on the effect of gas flow rate on the wave characteristics in two-phase gas-liquid annular flow," *Nucl. Eng. Des.*, vol. 236, no. 24, pp. 2580–2588, 2006.

[102] P. Ju, Y. Liu, X. Yang, and M. Ishii, "Wave characteristics of vertical upward adiabatic annular flow in pipes," *Int. J. Heat Mass Transf.*, vol. 145, p. 118701, 2019.

[103] S. Chandrasekhar, *Hydrodynamic and hydromagnetic stability*. North Chelmsford: Courier Corporation, 2013.

[104] M. J. Holowach, L. E. Hochreiter, and F. B. Cheung, "A model for droplet entrainment in heated annular flow," *Int. J. Heat Fluid Flow*, vol. 23, no. 6, pp. 807–822, 2002.

[105] M. Ishii and M. A. Grolmes, "Inception criteria for droplet entrainment in two-phase concurrent film flow," *AIChE J.*, vol. 21, no. 2, pp. 308–318, 1975.

[106] F. Dobran, "Hydrodynamic and heat transfer analysis of two-phase annular flow with a new liquid film model of turbulence," *Int. J. Heat Mass Transf.*, vol. 26, no. 8, pp. 1159–1171, 1983.

[107] D. Schubring, "Behavior interrelationships in annular flow," Ph.D. dissertation, University of Wisconsin-Madison, Madison, WI, 2009.

[108] R. Kumar, M. Gottmann, and K. R. Sridhar, "Film thickness and wave velocity measurements in a vertical duct," *J. Fluids Eng.*, vol. 124, no. 3, pp. 634–642, 2002.

[109] A. Al-Sarkhi, C. Sarica, and K. Magrini, “Inclination effects on wave characteristics in annular gas--liquid flows,” *AIChE J.*, vol. 58, no. 4, pp. 1018–1029, 2012.

[110] P. Marmottant and E. Villermaux, “On spray formation,” *J. Fluid Mech.*, vol. 498, pp. 73–111, 2004.

[111] D. Schubring and T. A. Shedd, “Wave behavior in horizontal annular air--water flow,” *Int. J. Multiph. Flow*, vol. 34, no. 7, pp. 636–646, 2008.

[112] T. Hazuku, T. Takamasa, and Y. Matsumoto, “Experimental study on axial development of liquid film in vertical upward annular two-phase flow,” *Int. J. Multiph. Flow*, vol. 34, no. 2, pp. 111–127, 2008.

[113] M. B. Alamu and B. J. Azzopardi, “Wave and drop periodicity in transient annular flow,” *Nucl. Eng. Des.*, vol. 241, no. 12, pp. 5079–5092, 2011.

[114] B. J. Azzopardi, *Gas-liquid flows*. New York: Begell House, 2006.

[115] K. Sekoguchi, T. Ueno, and O. Tanaka, “Flow characteristics of air-water annular flow (2nd report: correlation for flow parameter),” *Trans. Jpn. Soc. Mech. Eng.*, vol. 51, no. B, pp. 1798–1806, 1985.

[116] D. G. Owen, “An experimental and theoretical analysis of equilibrium annular flows,” Ph.D. dissertation, University of Birmingham, Birmingham, UK, 1986.

[117] G. F. Hewitt, “Churn and wispy annular flow regimes in vertical gas-liquid flows,” *Energy & Fuels*, vol. 26, no. 7, pp. 4067–4077, 2012.

[118] M. Ishii and K. Mishima, “Droplet entrainment correlation in annular two-phase flow,” *Int. J. Heat Mass Transf.*, vol. 32, no. 10, pp. 1835–1846, 1989.

[119] G. Wang, P. Sawant, and M. Ishii, “A new entrainment rate model for annular two-phase flow,” *Int. J. Multiph. Flow*, vol. 124, p. 103185, 2020.

[120] L. B. Fore, S. G. Beus, and R. C. Bauer, “Interfacial friction in gas--liquid annular flow: analogies to full and transition roughness,” *Int. J. Multiph. Flow*, vol. 26, no. 11, pp. 1755–1769, 2000.

[121] R. J. Belt, J. M. C. Van’t Westende, and L. M. Portela, “Prediction of the interfacial shear-stress in vertical annular flow,” *Int. J. Multiph. Flow*, vol. 35, no. 7, pp. 689–697, 2009.

[122] T. Hazuku, T. Takamasa, T. Hibiki, and M. Ishii, “Interfacial area concentration in annular two-phase flow,” *Int. J. Heat Mass Transf.*, vol. 50, no. 15–16, pp. 2986–2995, 2007.

VITA

Guanyi Wang was born in Henan, China in November 1991, son of Weiguo Wang and Yongliang Zhao. He received his elementary school education in Nanyang, middle and high school education in Zhengzhou. In 2010, Mr. Wang attended the Chongqing University, where he earned a Bachelor of Science in Nuclear Engineering in 2014. Then he joined the Thermal-hydraulics and Reactor Safety Laboratory (TRSL) at Purdue University to pursue Master degree and Doctor of Philosophy in Nuclear Engineering under the supervision of Distinguished Prof. Mamoru Ishii. As a graduate research assistant at TRSL, Mr. Wang engaged in several research projects sponsored by the Nuclear Regulatory Commission, Naval Nuclear Laboratory (Bettis), and Department of Energy (NEUP). For the dissertation study, he focused on the experiments and model development of interfacial area transport phenomena.

PUBLICATIONS

1. Wang, G., Sawant, P., & Ishii, M. (2020). A new entrainment rate model for annular two-phase flow. *International Journal of Multiphase Flow*, 124, 103185.
2. Wang, G., Zhang, M., & Ishii, M. (2020). Flow structure of bubbly to slug transition flow in a small pipe. *International Journal of Heat and Mass Transfer*, 147, 118943.
3. Wang, G., Zhu, Q., & Ishii, M. (2020). Interfacial structures in bubbly-to-slug transition flows in a duct. *Nuclear Technology*, 206 (2), 347-357.
4. Wang, G., Zhu, Q., Dang, Z., Yang, X., Ishii, M. (2019). Prediction of interfacial area concentration in a small diameter round pipe. *International Journal of Heat and Mass Transfer*, 130, 252-265.
5. Wang, G., Yan, Y., Shi, S., Dang, Z., Yang, X., Ishii, M. (2018). Experimental Study of Blowdown Event in a PWR-Type Small Modular Reactor. *Nuclear Technology*, 205(1-2), 297-306.
6. Wang, G., Li, Z., Yousaf, M., Yang, X., Ishii, M. (2018). Experimental study on vertical downward air-water two-phase flow in a large diameter pipe. *International Journal of Heat and Mass Transfer*, 118, 919-930.
7. Wang, G., Yan, Y., Shi, S., Yang, X., Ishii, M. (2018). Experimental study on accident transients and flow instabilities in a PWR-type small modular reactor. *Progress in Nuclear Energy*, 104, 242-250.
8. Wang, G., Dang, Z., Ju, P., Yang, X., Ishii, M., Ireland, A., Bajorek, S., Bernard, M. (2017). Experimental study on interfacial structure and interfacial area transport in downward two-phase flow. *International Journal of Heat and Mass Transfer*, 106, 1303-1317.
9. Wang, G., Tang, K., Ishii, M., (2019 August). Film thickness and disturbance wave structure of upward annular flow. 18th International Topical Meeting on Nuclear Reactor Thermal Hydraulics (NURETH-18), Portland, OR
10. Wang, G., Zhang, M., Ishii, M., (2019 May). Interfacial characteristics at bubbly to slug transition flow in a small diameter round pipe. 27th International Conference on Nuclear Engineering (ICONE27), Tsukuba, Japan
11. Wang, G., Li, X., Yang, X., Ishii, M., (2019 November). An entrainment rate correlation for annular flow, 2019 ANS Winter Meeting, Washington, D.C.

12. Wang, G., Zhu, Q., Ishii, M., (2018 November). Interfacial structures in bubbly to slug transition flows in a duct, 2018 Advances in Thermal Hydraulics, Orlando, FL
13. Wang, G., Yang, X., Zhu, Q., Ishii, M., (2017 September). Evaluation of two-group interfacial area transport equations in small pipe and improvement at bubbly to slug transitions flow. 17th International Topical Meeting on Nuclear Reactor Thermal Hydraulics (NURETH-17), Xi'an, China
14. Wang, G., Yan, Y., Shi, S., Tang, K., Dang, Z., Yang, Z., Yang, X., Ishii, M., (2017 September). Experimental study of blowdown event in a PWR-type small modular reactor. 17th International Topical Meeting on Nuclear Reactor Thermal Hydraulics (NURETH-17), Xi'an, China
15. Wang, G., Li, X., Yang, X., Ishii, M., (2017 November). Vertical downward two-phase flow in a large diameter pipe, 2017 ANS Winter Meeting, Washington, D.C.
16. Wang, G., Xiao, X., Zhu, Q., Yang, X., Chen, S., Ishii, M., (2015 November). Local Measurement of Adiabatic Two-Phase Flow in an Annulus under Low-Frequency Vibration, 2015 ANS Winter Meeting, Washington, D.C.